2018

Monolithically Integrated Wavelength Tunable Laser Diode for Integrated Optic Surface Plasmon Resonance Sensing

Thamer Tabbakh
University of Central Florida

MONOLITHICALLY INTEGRATED WAVELENGTH TUNABLE LASER DIODE FOR INTEGRATED OPTIC SURFACE PLASMON RESONANCE SENSING

by

THAMER TABBAKH
B.S. in Electrical Engineering, College of Engineering, Taibah University, 2011
M.S. in Electrical Engineering, College of Engineering, University of Central Florida 2014

A dissertation submitted in partial fulfillment of the requirements
for the degree of Doctor of Philosophy
in the department of Electrical and Computer Engineering
In the College of Engineering and Computer Science
at the University of Central Florida
Orlando, Florida

Fall Term
2018

Major Professor: Patrick LiKamWa

ABSTRACT

In this work, we demonstrate an InGaAsP multiple quantum well tunable laser diode that amalgamates two gain sections with different bandgap energies. This is achieved using selective area intermixing of the multiple quantum wells, and impurity-free vacancy induced disordering. When different current combination is injected into each section, that leads to a laser wavelength peak whose position depends on the relative magnitudes of the two injected currents. The laser wavelength can be fine-tuned from 1538 nm to 1578 nm with relatively constant output power. The free spectral range FSR of the tunable laser found to be 0.25 nm. This tunable laser was launched into an optical surface plasmon resonance sensor head to provide an input light source for the SPR sensor.

Using the tunable laser diode, we have demonstrated an optical surface plasmon resonance sensor head that is based on an inverted rib dielectric waveguide, in which the resonance wavelength of the surface plasmon excited at the gold metal-dielectric interface depends on the refractive index of the liquid in contact with it. The inverted-rib waveguide of the SPR sensor head is made of a layer of SU-8 polymer with a refractive index of 1.568. While the lower cladding layer consists of silicon oxynitride (SiO_xN_y) with a refractive index of 1.526. The top surface is coated with 20 nm of chromium followed by a 50 nm thick layer of gold or with 4 nm of titanium followed by a 25 nm thick layer of gold. The SPR sensor head was designed, to allow monitoring of analyte media with a refractive index, ranging from 1.43 to the 1.52. Using a set of reference liquids representing the analyte medium, the sensitivity of the SPR sensor was measured using the fabricated tunable laser, an optical spectrum analyzer, and a photodiode. It was found that with various calibrated sample liquids in contact with the gold metal, a sharp resonance dip in the transmission spectrum occurred, and its position shifted to a shorter wavelength when the refractive index of the sample liquids was

increased. The average sensitivity of the SPR sensor devices was determined to be S = 334 nm/RIU.

This dissertation is dedicated to my parents, my siblings, my daughters, and my love (wife)

who was extremely patient and supportive with me during all these years

ACKNOWLEDGMENTS

Faculty Advisors

Dr. Patrick L. LiKamWa

Professor of Optics & Photonics, ECE

CREOL, The College of Optics & Photonics

University of Central Florida

Committee Members

Dr. Mercedeh Khajavikhan

Assistant Professor of Optics & Photonics

CREOL, The College of Optics & Photonics

University of Central Florida

Dr. Sasan Fathpour

Associate Professor of Optics & Photonics, ECE

CREOL, The College of Optics & Photonics

University of Central Florida

Dr. Issa Batarseh

Professor of Electrical Engineering

College of Electrical & Computer Engineering

University of Central Florida

Dr. Wasfy B. Mikhael

Professor of Electrical Engineering

College of Electrical & Computer Engineering

University of Central Florida

I would like to take this opportunity, to thank my advisor Prof. Patrick L. LiKamWa. Being part of Multiple Quantum Well group (MQW) was an awesome experience for me. The opportunity to work with you over the last few years have been enriching, you were really supportive and professional and kept me informed during my difficult times.

I would also like to extend my deepest gratitude to the members of the committee, Dr Mercedeh Khajavikhan, and Dr Sasan Fathpour. I am grateful for your advice and help. And to the dissertation committee members, thank you for your promptitude and kindness, it would not have been easy without you.

A special thanks goes out to Yousef Alahmadi for the inestimable assistance, which he rendered during the course of my work, particularly in my final years.

I also want to thank all CREOL students, staff, and faculty, especially my current and previous MQW group members, particularly Chi, Sailing, Gisela, Miguel, Parinaz for their support and generosity, I am truly humbled.

Furthermore, I am thankful to King Abdulaziz City for Science and Technology (KACST) and Saudi Arabia Government, I cherish their support and scholarship.

Lastly, I would like to thank my parents Abdulaziz and Najat for their love and support at all times, life without you would have been impossible. And to my siblings Saud, Miesa, Khlood, Ohood, and Nojod who always encouraged me to complete my PhD despite all odds, I love you all. Special thanks to my wife (Mai) who was extremely supportive and encouraging throughout this entire process, she made countless sacrifices to help me get to this point, regardless of the challenges. To my daughters Ruha (and unborn child, Ruaa), you inspired and motivated me to finish this degree.

TABLE OF CONTENTS

LIST OF FIGURES

LIST OF TABLES

LIST OF ACRONYMS

BOE	Buffered Oxide Etchant
EL	Electroluminescence
DOS	Density of States
IID	Impurity Induced Disordering
IFVD	Impurity Free Vacancy Disordering
IID	Impurity Induced Disordering
MEMS	Micro-Electro-Mechanical Systems
MMI	Multimode Interference
MOCVD	Metalorganic Chemical Vapor Deposition
MQW	Multiple Quantum Well
PECVD	Plasma Enhanced Chemical Vapor Deposition
PL	Photoluminescence
QW	Quantum Well
QWI	Quantum Well Intermixing
RIE	Reactive Ion Etching
RTA	Rapid Thermal Annealing
CTL	Commercial Tunable Laser
TE	Transverse Electric
TM	Transverse Magnetic
TE	Transverse Electric
TIR	Total Internal Reflection

SEM	Scanning Electron Microscope
SPR	Surface Plasmon Resonance
WCE	Wet Chemical Etching
WDM	Wavelength Division Multiplexing

CHAPTER 1: INTRODUCTION

Tunable laser diodes have made a tremendous jump in dynamic networks and many spectroscopic applications during the last two decades. The operation of semiconductor tunable lasers is very flexible, and the devices can operate in different places where wavelengths are linked to the fibers [1-4] .The flexibility of the lasers enables them to do multiple tasks thus reducing the number of lasers that are manufactured and bought. The lasers help the carriers to configure channels that are added to fiber, and they enable carriers to manage the wavelengths effectively based on the requirements of the customers. Flexibility shortens the time required to offer the services [4, 13]. Moreover, they are also considered a central factor for chemical detection in medical diagnosis and important for any optical test that requires spectral analysis, which demand simple tunable lasers with broad wavelength, ranges. Among these devices, integrated photonics sensor such as Surface Plasmon Resonance sensor, which is a key component in my dissertation, is in high demand.

Tunable lasers comprise of many types, which can be in solid, liquid and gas state. Examples of tunable lasers include diode lasers, rare-earth doped crystals, and dye lasers. Diode lasers are lasers that are made of semiconductor materials and the laser emission is created in an intrinsic layer sandwiched between p and n regions forming a p-i-n diode junction. The dye laser is a type of laser that uses organic dyes that are dissolved in liquid solvents that form the laser media. All these types of lasers are applied in different areas of communications, spectroscopy and photochemistry [1-5]. Sorokin and Lankard, and Schäfer were first to demonstrated a tunable laser using the organic dye laser in 1966 [1, 2]. Fabry-Perot tunable laser diode were developed and proposed. This is a type of laser diode that consists and based on semiconductor devices. In the Fabry-Perot laser, the sharp facet forms the two mirrors that provide the feedback for the light. These tunable lasers are the most

commonly produced and used in laser pointers and the illumination of the light beam. FB tunable laser diodes consider is favored than DFB and DBR because it is cheap, easy to fabricate, and the lasers emit light in broad wavelengths range. A while later, distributed Bragg reflector (DBR) and distributed feedback (DFB) tunable lasers are already being used in many optoelectronics applications. DFB tunable laser structures and principle were proposed in the early 1970s[6]. Today, DFB tunable laser is used in almost all dense wavelength division multiplexing networks applications[7]. DFB laser is a laser in which active layer of the device is bounded by a diffraction grating that acts like an optical filter[8] with distributed reflection (feedback). It does not require any mirror in forming an optical cavity for laser action to occur. The grating continually reflects a single wavelength back into the cavity, thus the DFB laser operates in a single mode or inherently a degenerate double mode. [9]. On the other hand, the DBR tunable laser diode: is a type of laser diode where at least one of distributed Bragg reflector that form the laser resonator is placed outside of the active region [10]. This type of laser need an external modulator for a strong modulation. DBR lasers are stable, produce less noise, and it generates high powers than DFB laser. While, DFB is best in transmitting in long distances, Both DFB and DBR have superb single mode characteristics but the fabrication process is expensive and complicated.

The MQW laser diodes consists of semiconductor materials that are made of very thin layers of different bandgap energy and which confine and trap free charge carriers. These MQW laser diodes can produce high power conversion efficiencies as well as high quantum efficiency. Furthermore, high power output and small leakage current make the multiple quantum wells also the best candidate for the manufacturing of LEDs. In this dissertation, we introduce a novel InGaAsP multiple quantum well tunable laser diode that amalgamate two gain sections with different bandgap energies based on MQW intermixing technique. This tunable laser is simple in operation, and it can be integrated with other devices to perform many complex tasks. The purpose of this dissertation is to introduce and

demonstrate a novel InGaAsP multiple quantum well tunable laser diode. This tunable laser diode consists of two sections with different bandgap energies achieved using selective area intermixing of the MQW. Using plasma enhanced chemical vapor deposition (PECVD) followed by photolithography and reactive ion etching (RIE), half of the sample is coated with a 30nm thick layer of silicon nitride (SiN_x) film followed by a 200nm thick overlay of silicon oxynitride (SiO_xN_y) film over the entire sample. The whole sample is then thermally annealed at 750°C for 30s, and that results in the SiO_xN_y covered section of the MQW experiencing an increase of the bandgap energy, while leaving the SiN_x covered section practically unchanged. A laser stripe is fabricated that passes through both intermixed and non-intermixed sections. The wavelength of laser operation can then be tuned by varying the injected current levels applied separately to the two sections. The obtained tuning range was 40 nm spanning from 1538 nm to 1578 nm. We have partiality integrated our tunable laser to be as an input light source for a SPR sensor.

1.1. Dissertation outline

In this work, tunable laser and SPR sensor have been simulated, designed, fabricated, and tested using an epitaxially grown InGaAsP multiple quantum wells (MQW) on InP wafer. The electrical and optical properties for the MQW (InGaAsP MQW has been used in the proposed tunable laser) and semiconductor materials (GaAs and Si has been used in the proposed SPR sensor) have been characterized and investigated by injection carrier or optical pumping.

In chapter two, discussions on the theory and principles for semiconductors, semiconductor lasers, and MQWs will be performed.

Three stages are required to achieve the proposed tunable laser namely; MQW intermixing (chapter 3), photonic device integration (chapter 4), optoelectronic device fabrication and testing of the tunable laser (chapter 5) and SPR sensor. In chapter 3, the Impurity Free Vacancy Disordering (IFVD) technique, which is the key method for Multiple Quantum Well Intermixing (MQWI) is examined, characterized and explained. The MQWs form the core of our proposed novel tunable laser. After the InGaAsP MQW has been characterized, the integration ability of MQW sample needs to be tested because our proposed tunable laser needs to be integrated. Therefore, using the results and data from chapter 3, we were able to fabricate integrated optical devices, such as LED and modulators on the InGaAsP quantum well platform, and dual wavelength single waveguide laser diode discussed in chapter 4. Thus, chapter 5 shows the design and fabrication of the novel tunable lasers, based on the intermixing technique from chapter 3 and integration ability from chapter 4. SPR sensor topic and biosensor application will be discussed in chapter 6 and we shall conclude by proving that our fabricated tunable laser can be suitable for probing surface plasmon resonance optical sensor in chapter 7.

CHAPTER 2: THEORY AND PRINCIPLE FOR SEMICONDUCTORS LASER AND MULTIPLE QUANTUM WELLS

2.1.Theory of semiconductors material

There are two types of semiconductors; intrinsic and extrinsic semiconductors [16].In an intrinsic or pure semiconductor, (an undoped semiconductor is relatively close to being intrinsic), the number of electrons in the conduction band (free electrons) is equal to the number of holes in the valence band (free holes). While, extrinsic semiconductors are formed when an impurity (dopant) is brought in a semiconductor. It results in the introducing of new impurity energy levels. Doping is referred as the process of introducing impurities into a semiconductor as shown figure 2.1-1

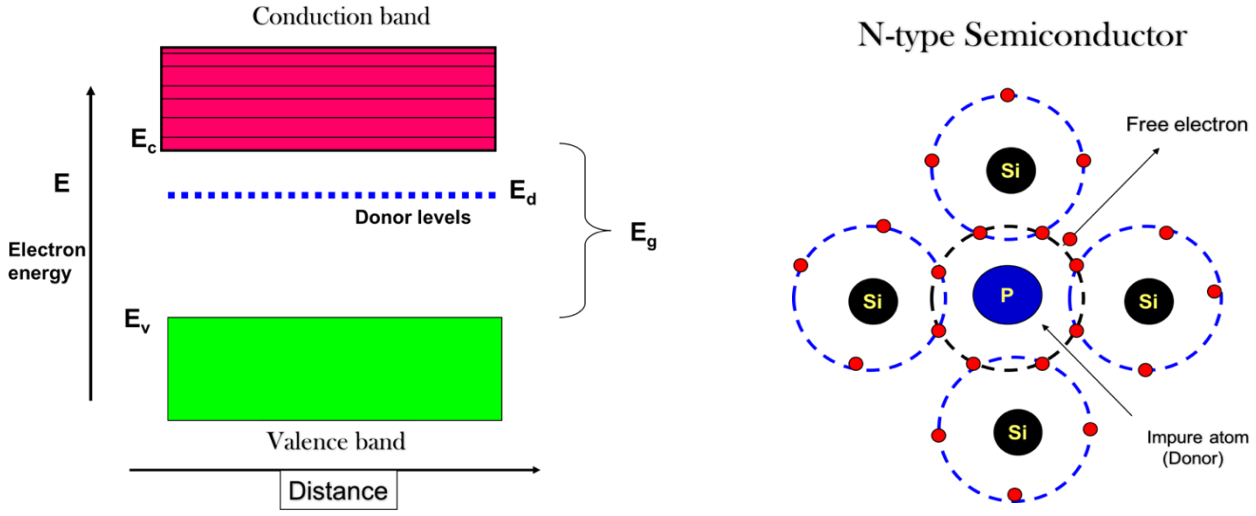

Figure 2.1-1, Phosphorous and Silicon- extrinsic semiconductors and they possess diamond cubic crystalline structure.

When a suitable form of energy is supplied to a semiconductor then electrons take transition from valence band to conduction band. Therefore, a free electron and hole in the conduction and valence band is formed respectively. This phenomenon is known as electron - hole pair generation. Conduction occurs because thermal energy excites electrons from the valence into the conduction band at its bottom region [17]. The Fermi-Dirac probability distribution [18] is used to compute the

quantity of electrons that are excited over the band gap. Probability function F (E) computed as shown in equation 2.1.1 below.

$$F(E) = \frac{1}{1+e^{(E-E_F)/kt}} \quad (2.1.1)$$

where T is the absolute temperature, E_F is the Fermi energy level and k is the Boltzmann constant [19]. Electron density in the conduction band can be illustrated by equation 2.1.2 as:

Where $$N_C \equiv 2\left(\frac{2\pi m_n kT}{h^2}\right)^{3/2} \quad (2.1.2)$$

Comparatively, the hole density p in the valence band is expressed by equation 2.1.3 as [20]:

Where $$N_v \equiv 2\left(\frac{2\pi m_p k_B T}{h^2}\right)^{3/2} \quad (2.1.3)$$

The number of holes (p) and electrons (n) in a pure semiconductor are equivalent in valence and conduction bands respectively [21]. That satisfies the expression ($n = p = n_i$) where n_i is the intrinsic carrier density. Halfway in the forbidden gap lies the Fermi level energy for an intrinsic semiconductor. Despite the fact that energy levels are now forbidden, the likelihood of finding an electron here is half [22]. In addition, the electron will only move from the valence band to the conduction band through thermal excitation.

Whether the electrons are in the valence or conduction band is dictated by two important aspects of the semiconductor, the Fermi-Dirac functions and the Density of States (DOS). The Fermi-Dirac principle provides the probability of finding an electron in any of the quantum states in reference to a virtual energy level. The fermi distribution concept based on Pauli's exclusion principle of accommodating onto two electrons with opposing spins in the same energy level. The Fermi energy E_F mathematically represented by equation 2.1.4.

$$f_{FD} = \frac{1}{1+e^{\frac{\xi-\xi_f}{k_B T}}} \quad (2.1.4)$$

Where k_B is the Boltzmann constant and

ξ_f is called the Fermi energy level or Fermi level

The energy distribution of electrons in the conduction band and holes in the valence band can be represented by the product of the Fermi-Dirac function with the availability of states in the conduction and valence bands respectively (DOS function). In the case of an intrinsic semiconductor (constant DOS), we can graphically represent the electron/hole concentration in Fig 2.1-2.

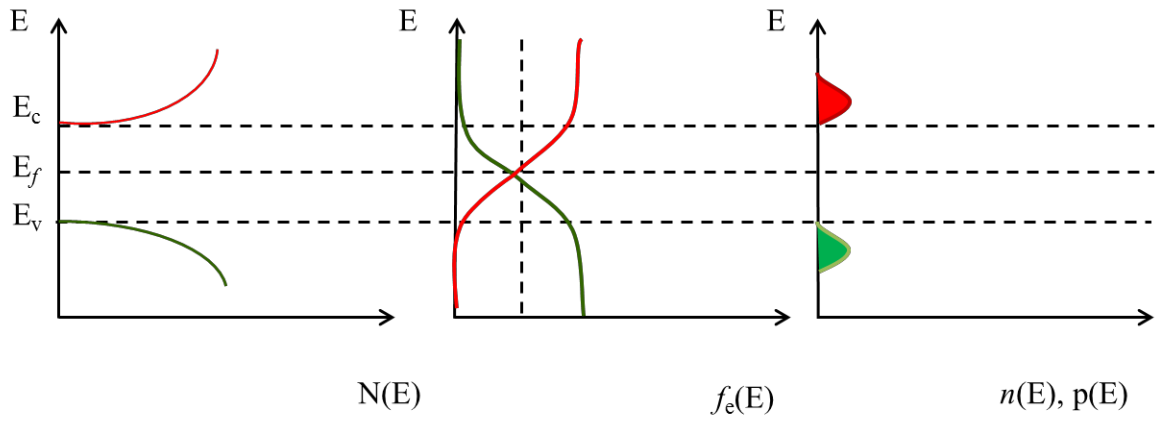

Figure 2.1-2, the energy distribution of electrons in the conduction band and holes in the valence band in the case of an intrinsic semiconductor.

The generation of photon process can occur by recombination of free electron in the conduction band with a hole in the valence band. This can be easily achieved by creating a *p-i-n* structure. When N-type and P-type dopants are introduced side-by-side with an intrinsic layer sandwiched between them in semiconductor, a *p-i-n* junction is formed. Applying voltage to p-i-n add more carries or holes in conduction or violence band. In forward bias voltage, there are large diffusion currents of minority carriers through the junction. Both holes and electrons diffuse across the junction into the intrinsic region as shown in figure 2.1-.3

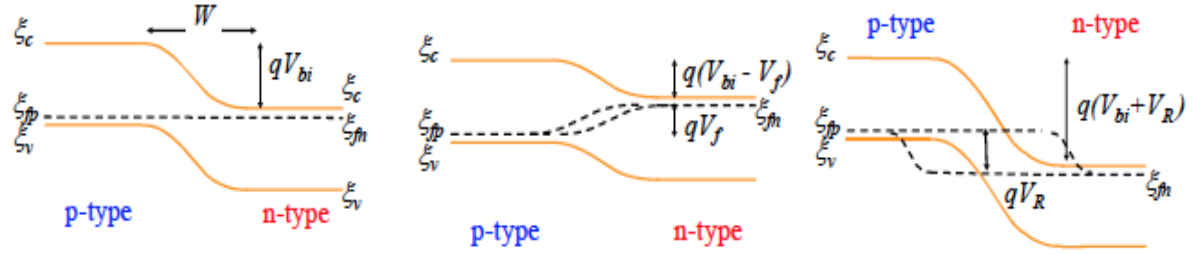

Figure 2.1-3, A In thermal equilibrium the Fermi energy levels in the p- and n-type materials lineup. B, forward bias The Fermi levels become discontinuous across the depletion region. C, Reverse bias causes an increase in the potential energy for the motion of majority carriers.

However, as we apply more voltage into N and P regions, recombination currents from the majority carriers dominate. The current and voltage relationship of a *p-i-n* junction is exponential in forward bias region, and relatively constant in reverse bias region that causes an increase in the potential energy for the motion of majority carriers. Only leakage current due to minority carriers can flow as shown figure 2.1-4 and equation 2.1.5.

$$I_D = I_s\left(e^{\frac{qV_D}{k_B T}} - 1\right) \qquad (2.1.5)$$

Where q = electron charge ($1.602e^{-19}$ C), I_S = Saturation current (A), V_D = Voltage across Diode (V) , k_B = Boltzmann's constant ($1.381e^{-23}$ J/K), T = Temperature (K)

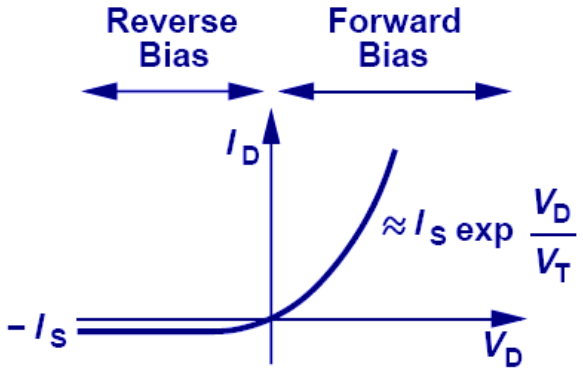

Figure 2.1-4, the current and voltage relationship of a p-i-n junction forward and reverse bias.

However, in order to enhance optoelectronic device performance to higher efficiency and faster response time, the thickness of the depletion region should be increased. Forming a double heterostructure as shown in figure 2.1-5. By applying forward bias voltage, the electrons and holes

are trapped in the i region which leads to high recombination efficiency devices such as LEDs and laser diodes. Furthermore, the heterostructure also help to confine the emitted photons to remain in the i region. Thus, i-region has a lower bandgap energy (higher index of refraction) following Moss rule than the p and n regions. Therefore, the electrons will be trapped in the lower bandgap region (i-region) because of the high hetero-barrier, thus will improve the recombination efficiency. Since the recombination occur in the lower bandgap energy region, the emitted photon has a same energy of the i-region, thus will reduce the photon absorption in the top cladding layer and improve the extraction efficiency.

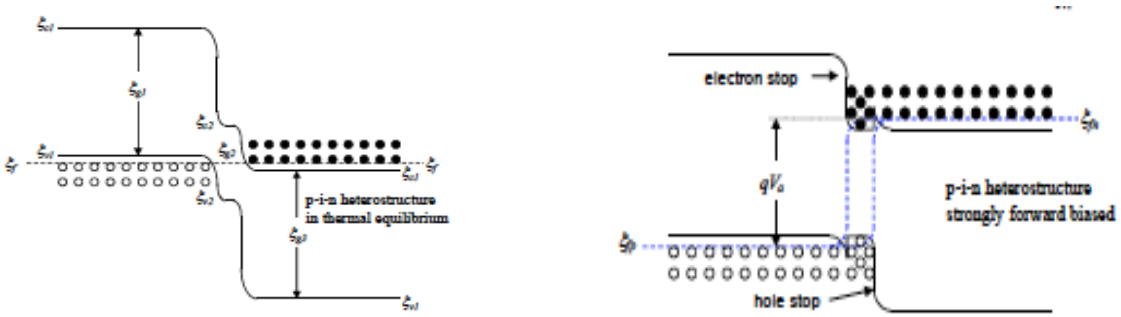

Figure 2.1-5, Energy band diagram and particles flow for p-i-n heterostructure under equilibrium condition and forward bias.

2.2.Semiconductor laser diodes

The semiconductor laser diode is considered as one of the most important types of lasers because it operates with low power and is very energy efficient with its very important application in fiber optic communication. The basic mechanism that is responsible for the light emission from a semiconductor is the recombination of electrons and holes in the intrinsic region of a p-i-n junction when forward voltage is applied across the junction. At this point, the injected electrons and holes will increase the density of electrons in the conduction band and holes in the valence band respectively resulting in population inversion. The stimulated emission rate will exceed the absorption rate as the current is

further increased. Thus, optical amplification will overcome the losses in the cavity and the device will begin to emit coherent radiation. When the photons pass through the active region, they experience optical gain because there will be more electrons in the conduction band than the electrons that getting absorbed in the valence band. The recombination of electrons and holes in the i-region creates stimulated emission. As the injected carriers increase, lasing will take place with a wavelength that corresponds to the peak of overall "gain-loss" spectrum of the cavity. An optical cavity (or resonator) is a must in a laser to reach to the gain condition which is given by equations 2.2.1, 2.2.2 and figure 2.2-1.

$$\gamma(\xi) = \frac{Power\ emitted\ per\ unit\ volume}{Power\ crossing\ per\ unit\ volume} cm^{-1} \tag{2.2.1}$$

$$\gamma(\xi) = \left[2 * 10^4 (\xi - \xi_g)^{\frac{1}{2}}\right] * \left[f_e(\xi_2) + f_h(\xi_1) - 1\right] \tag{2.2.2}$$

Where $f_e = \dfrac{1}{1+\exp\left(\dfrac{\xi_2 - \xi_{fn}}{k_B T}\right)}$ and $f_h = \dfrac{1}{1+\exp\left(\dfrac{\xi_{fp} - \xi_1}{k_B T}\right)}$

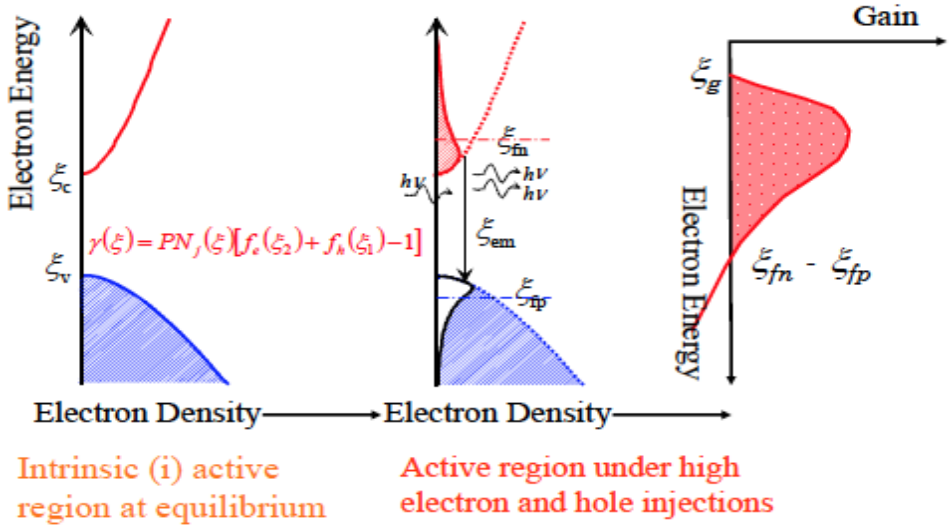

Figure 2.2-1, LED emission process as forward voltage is applied.

The active region in a semiconductor acts as an optical cavity that is needed for the laser where light can oscillate and gets to lase. The oscillations provide a coherent radiation at the device output leading to a Fabry-Perot laser effect. The active region can be represented as a slab optical waveguide where light is confined in the active region and surrounded by layers that have lower refractive index values. The Fabry-Perot effect is a result of these coherent oscillations, an internal multiple reflection within the optical will occur. However, in order to obtain lasing we need feedback for the photons. This is normally achieved by placing the gain medium within a resonator cavity. In the case of semiconductors, cleaving the two ends conveniently produces optical flats acts as feedback mirrors. The natural reflectivity of the semiconductor to air interface is calculated using equation 2.2.3

$$R = \left(\frac{n-1}{n+1}\right)^2 \tag{2.2.3}$$

Consequently, waveguides in conjunction with plane mirrors placed orthogonally provides conveniently compact and stable resonators for laser feedback as shown in figure 2.2-2.

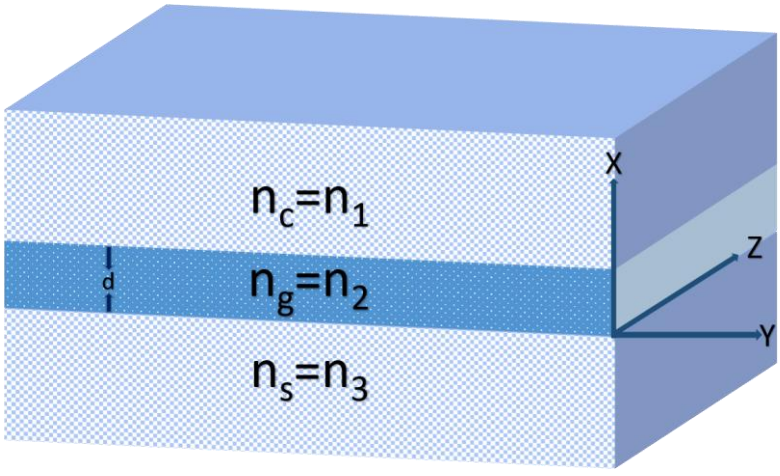

Figure 2.2-2, the slab waveguide is the simplest waveguiding structure because the confinement is only one dimensional.

2.3.Multiple quantum wells

A multiple quantum well is a specific sort of a semiconductor with a thin layer of heterostructure encompassed of two or more layer material. Multiple quantum wells are applied in the manufacture of light emitting diodes and lasers for high power applications [24]. These diodes have high power conversion efficiency as well as high quantum efficiency. In addition, high power output and very little leakage current makes the multiple quantum wells the best candidate for the manufacture of LEDs and lasers. The electrical and the optical properties of multiple quantum wells can be improved by efficient electron blocking [25]. In multiple quantum wells, the quality of the active region can be improved by depositing the cap layer at low temperature [26]. This is achieved by use of two –step growth method. In addition, two step-growth methods have been used to improve both structural and optical properties of multiple quantum wells.

Electrons within the multiple quantum wells system are not static. The change in the system to indicate a quantum number *j* which is given by the equation 2.3.1 as shown below.

$$\mathrm{E} = \frac{\pi^2.\hbar^2.j^2}{2.m_e.{d_z}^2} \qquad (2.3.1)$$

In multiple quantum wells, the motion of an electron in two or three dimension is determined by the Heisenberg uncertainty principle. In addition, the electrons move freely within the allowable energy levels [27]. Pseudomorphically grown InGaAs experience strain within the band gap energy. This strained band gap E_g^{str} is calculated using equation 2.3.2 as shown below [28].

$$E_g^{str} = E_g + \Delta E_h \pm \Delta E_s \ldots\ldots\ldots\ldots\ldots\ldots\ldots\ldots\ldots\ldots\ldots \quad \ldots \qquad (2.3.2)$$

The energy shift of the hydrostatic portion ΔE_h is given by equation 2.3.3.

$$\Delta \mathrm{E}_h = [-2.d.\varepsilon_{II}]\left[\frac{C_{11}-C_{12}}{C_{11}}\right]\ldots\ldots\ldots\ldots\ldots\ldots\ldots\ldots\ldots\ldots \qquad (2.3.3)$$

In addition, the contribution due to uniaxial part of the energy shift is given by the equation 2.3.4 as shown below.

$$\Delta E_s = [\pm d_2 . \varepsilon_I] \left[\frac{C_{11}-2C_{12}}{C_{11}}\right] \ldots\ldots\ldots\ldots\ldots\ldots\ldots\ldots\ldots\ldots\ldots\ldots\ldots\ldots \quad (2.3.4)$$

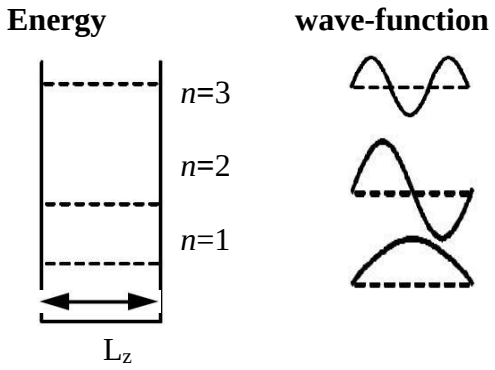

Figure 2.3-1, Infinite quantum wells and the corresponding wave-functions.

From the above figure 2.3-1, the wave-function follows sinusoidal curve. At the bottom of the quantum well, we have first allowable energy level. It can be observed from the above figure that as the quantum wells becomes narrow, the spacing distance (that is L_Z) between the energy levels becomes larger.

In quantum wells, for the bearing of the majority charge carrier are at right angle to the layers, the energy band gap has a choice policy that determines the excitation of electrons from the lower energy level to the higher energy level. The policy states that only changes between conditions of a similar discrete photon energy in the valence band and in the conduction groups are permitted. This is applicable within the conduction and the valence wave capacities. The standing wave of sinusoidal form appears for the vast multiple quantum wells. This is illustrated by figure 2.3-2 above. In addition, it can be observed that the stationary waves as conditions of particular force that determines the motion of electrons within the quantum well. In the mass semiconductors, we can equally see the force preservation tends to follow from permitted cover integrals. Multiple quantum wells are therefore considered between plane wave wave-functions [20].

The cavity height in the multiple quantum well is reduce to around 100-200 Å , or around 40 nuclear layers [24-25]. The cavity width ,which is generally between 5 to 20 μm, needed to be as narrower as possible to prevent lateral modes from appearing and producing laser in one line . Figure 2.3-2 show an example of cavity structure for InGaAsP MQW which is have been used as the platform in this dissertation.

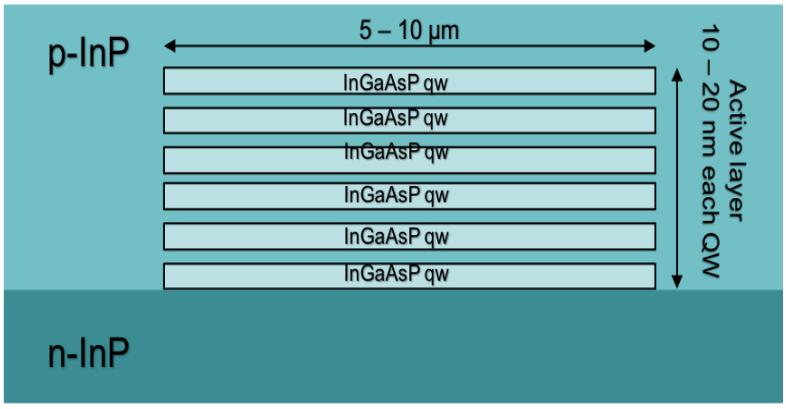

Figure 2.3-2 Cavity Structure of a InGaAsP Multiple Quantum Well Laser

The QW cavity geometry reduce the amount of material (which reduce the amount of energy for lasing) in the active region to reach to the lasing condition, thus reduce the threshold current ,increases the gain characteristic, and device efficiency. Furthermore QW has lower temperature dependency and narrower linewidth than the non QW devices. In addition, the momentum effects is much less to form in the QW due to narrower cavity width. For all of the above mentioned reason, we have chosen to fabricate our laser using MQW structure. The InGaAsP MQW has the proper band gap range for the 1550 nm wavelength and freedom in composition as well as thickness to adjust the wavelength.

CHAPTER 3: CHARACTERIZATION OF INTERMIXED InGaAsP MULTIPLE QUANTUM WELLS

3.1. Overview

Quantum well Intermixing (QWI) is one of the most important technique in the last decade in optoelectronics specially in fabrication of high performance laser diodes and photonic integrated circuits (PIC)[32-37]. Intermixing tune the bandgap energy that leads to a change in the refractive index. Thus, the laser wavelength could be shifted toward higher frequency (blue part of the spectrum) or toward lower frequency (red part of the spectrum) by using the right mixture of the coated films. Selective area intermixing of multiple quantum wells using impurity-free vacancy diffusion (IFVD) has been ongoing task in device fabrication for the past few decades, due to its ability to inherent spatial selectivity between adjacent regions and conserve the electrical properties of the disordered and non-disordered sections alike [38-47]. The side effects of using IFVD technique are drops in efficiency and increases in waveguide losses. There are other techniques for QWI such as ion-implantation-induced inter-diffusion, impurity-induced disordering (IID), and laser induced disordering (LID). These techniques are more costly and complicated than the IFVD. In this work however we present a controllable red and blue shifting of the band to band wavelength emission up to 120nm toward red and 140nm toward blue.

3.2. Impurity Free Vacancy Disordering (IFVD) and Multiple Quantum Well Intermixing.

Among the many techniques that has been utilized for intermixing the quantum well, impurity-free vacancy diffusion (IFVD) is considers to be the most reliable and promising technique due to its ability to conserve the electrical properties of the quantum well structure. Moreover, IFVD is an inexpensive, reliable and highly reproducible process granted stable equipment. The IFVD techniques are usually performed by selecting a capping layer, silicon oxynitride (SiO_xN_y) or silicon

nitride (SiN_x). In case of group InGaAsP materials, SiO_xN_y film promotes the out-diffusion of Ga atoms from the top layer of the semiconductor into the upper dielectric capping layer through a rapid thermal annealing ,figure 3.2.-1. As the annealing continues, the vacancies that are thus introduced at the surface, rapidly migrates towards the substrate layer. As the vacancies pass through the MQW layers, they exchange lattice sites with constituent atoms of the well and barrier materials causing a significant inter-diffusion of the species especially at the well/barrier interfaces. The SiO_xN_y film therefore usually causes the bandgap of the quantum wells to increase (blue shifting of the absorption edge). On the other hand, covering the surface of the semiconductor with SiN_x usually serves to prevent the out-diffusion of Ga atoms from the top surface, thereby protecting the MQW below from intermixing, figure.3.2-1.

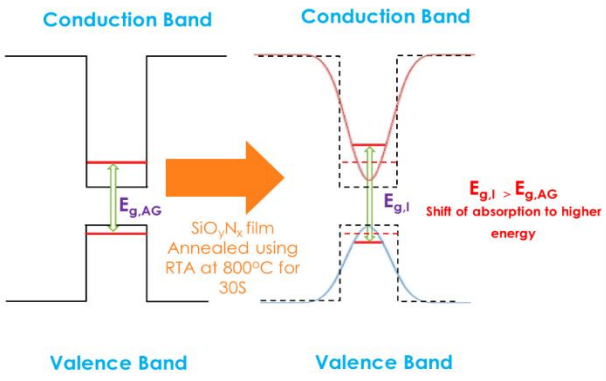

Figure 3.2-1, Bandgap energy diagram before and after capping it with SiO_yN_x film after intermixed it using RTA.

The dielectric film properties and the annealing condition in this technique play a critical role in the degree of intermixing. In addition to this parameters, we showed that, the manipulation of the Nitrogen and Oxygen shares in the top cladding films can bring a wide range of selectivity for the blue/red shifting of the bandgap energies. To confirm the mentioned tunings, we collect the photoluminescence spectra of the disordered samples along with the emission spectra of LED devices fabricated on the disordered quantum well wafers which corroborate with the former photoluminescence measurements. Furthermore, we have fabricated multiple lasers with various

capping films, in order to characterize the effects of the intermixing in the proposed tunable laser. We have calculated and measured the blue and red shift, slope efficiency, threshold current, and waveguide losses for InGaAsP multiple quantum wells.

3.3. InGaAsP multiple quantum well structure

The structure used as the platform in this study consists of six InGaAsP quantum wells grown by metal organic chemical vapor deposition (MOCVD) at a commercial semiconductor foundry. The p-i-n structure is grown epitaxially on a Si doped InP substrate with a 70nm thick undoped InGaAsP buffer at the n-i and p-i interface. The active region consists of six undoped InGaAsP (λg = 1.56 μm) quantum wells each 8 nm thick sandwiched between five undoped layers of 15 nm thick InGaAsP (λg = 1.13 μm) barriers, where λg is the bandgap wavelength. The wafer design is shown in figure 3.3-1

InGaAs p-type	100nm
InP p-type (Zn dopped)	1000nm
InGaAsP U/D	70nm
5×InGaAsP (15nm)/6×InGaAsP(8nm)	
InGaAsP U/D	70nm
InP n-type (Si dopped)	2500nm
InGaAs n-type (Si dopped)	50nm
InP Substrate (Si dopped)	

Figure 3.3-1, Schematic cross sectional view of MQW grown by MOCVD.

.

3.4. IFVD for MQW LED devices.

Several samples have been prepared with a variety of SiO_2, SiN_x and SiO_yN_x films grown by plasma-enhanced chemical vapor deposition (PECVD) as the capping layers. Table 3.4.1 shows the different recipes that were used to grow the variety of films. In the evaluation process, the top surface of each sample was first covered by a film of a SiN_x or SiO_yN_x using PECVD.. As indicated in table 3.4.1, the different SiO_yN_x films were generated by manipulation of the ratio of N_2O to NH_3 to control the eventual content of oxygen in the dielectric film. It is fair to assume that a larger oxygen content will lead to a lower refractive index whereas a larger nitrogen content will lead to a higher refractive index. Furthermore, another set of SiN_x films was generated in the absolute absence of N_2O, where the only controllable parameter was the silicon to nitrogen ratio which was achieved by varying the SiH_4 to NH_3 ratio during the PECVD growth. Here a silicon rich SiN_x film will exhibit a higher refractive index. However, in the final analysis, to be able to compare all the dielectric films together, we have sorted them according to their refractive indices. The thickness of the SiN_x /SiO_yN_x films was kept at 30 nm as a good compromise between repeatability and film robustness to high temperature anneals. Each sample then was treated individually in a rapid thermal annealer (RTA) for 30 sec at 800 ^oC.

The absolute values of photoluminescence peak shift from that of the as-grown sample is plotted in figure 3.4-1 as a function of the refractive indices of the covering films. The down-pointing triangles indicate SiO_yN_x films while the up-pointing triangles refers to SiN_x claddings. From this figure, an absolute shift of bandgap energy equal to -140 nm toward blue and +120 nm toward red is recognizable. As expected, the SiO_yN_x films with higher share of Oxygen tends to bring a blue shift similar to the SiO_2 films, while larger ratios of NH_3/N_2O produce SiO_yN_x films that contain larger

x/y ratios with correspondingly higher refractive indices tend to shift the PL to a longer wavelength. However in the absence of N_2O component, the SiN_x films lead to red shifting of the PL peak. The degree of this red-shift could be controlled by the ratio of SiH_4 to NH_3, with a larger ratio of SiH_4/NH_3 resulting in more bandgap narrowing of the MQWs.

Table 3.4-1, Recipes for various film composition sorted with respect to their refractive index.

	Power(W)	Temp(oC)	SiH_4(sccm)	NH_3(sccm)	N_2O(sccm)	N_2(sccm)	HE(sccm)	Index of Refraction
1	150	300	200	4	20	800	0	1.55
2	100	250	200	10	35	600	0	1.573
3	100	250	200	10	29	600	0	1.594
4	150	300	180	3.5	10	800	0	1.621
5	150	300	180	3.5	5	800	0	1.839
6	100	250	180	4.2	0	200	219	1.884
7	150	300	180	4	0	0	450	1.951
8	150	300	200	4	4	800	0	1.959
9	100	250	240	4	0	200	219	1.967
10	150	300	180	4.2	0	200	219	2.034
11	150	300	180	3.75	0	200	219	2.106
12	150	300	200	4	0	800	0	2.134
13	150	300	220	4	0	200	219	2.175
14	150	300	200	3.5	0	800	0	2.2

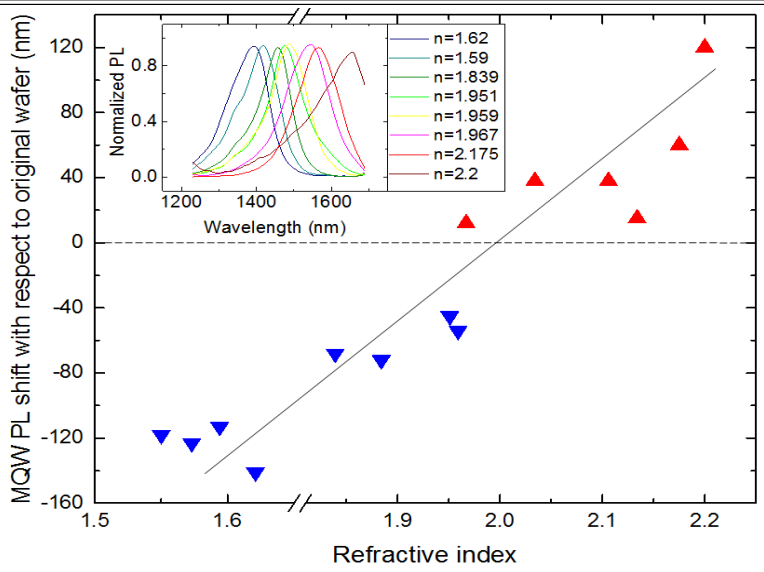

Figure 3.4-1, Measured absolute value of the PL shift of the RTA treated samples from that of the as-grown wafer for different dielectric film capping, in respect to the refractive index of the film. The blue shift associated with SiOyNx films, while the red shift refers Si-rich compositions. The inset shows the absolute PL spectrum for selected data points.

A more thorough study has been focused on SiN_x films of varying Si compositions. To reduce any other unintended influences, in the growth of the SiN_x films, the SiH_4, He and N_2 mass flow rates as well as the plasma RF power and the substrate temperature were all kept constant while changing the NH_3 flow for all different recipes. Figure 3.4-2 shows the absolute PL shift of such samples treated with RTA. The results clearly show a red shifting of the PL peak emission for Si-rich compositions of SiN_x with the largest shift occurring when the ratio of SiH_4 to NH_3 is highest during the PECVD process.

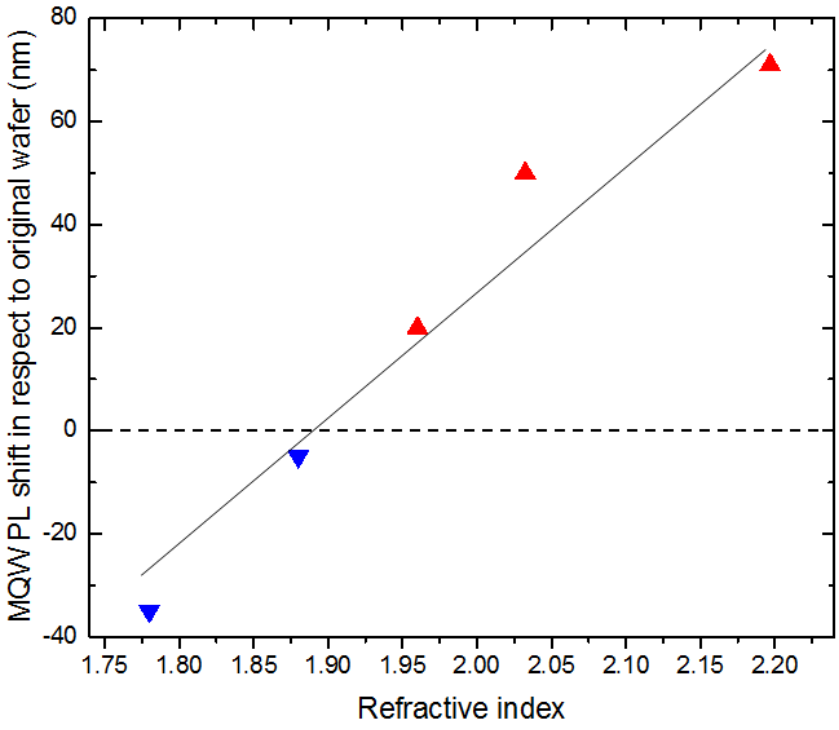

Figure 3.4-2, Blue/Red shifting of PL emission peak from a MQW structure disordered by different SiNx films.

3.5. IFVD for MQWs laser diode devices.

Using plasma-enhanced chemical vapor deposition (PECVD) several samples were coated with diverse range of SiN_x, and SiO_yN_x, films. Table 3.5.1 shows the various recipes that were used to grow the SiN_x, and SiO_yN_x films on the InGaAsP quantum wells with their corresponding refractive index. The thickness of SiN_x and SiO_yN_x films were conserved at 40 nm to protect the films from high stress at high annealing temperature. Then, all the fabricated samples were annealed using Rapid Thermal Annealer (RTA). Simultaneously at 800^0C for 30 sec [48]. The exposed SiN_x and SiO_yN_x films were detached after the annealing using reactive ion etching (RIE). All the samples then recoated with a 200 nm thick SiO_2 film. Subsequently, a positive photoresist has been spin-coated in top of the SiO_2 film in order to form a waveguide ridge. The 4 μm wide waveguide patterned have been transferred in to the photoresist and then in to the SiO_2 film by RIE. The top InGaAs, InP, and InGaAsP etch stop layers were wet etched using mixtures of H_2O_2:H_2O:H_3PO_4, H_3PO: HCl, and HNO_3: HCl: H_2O, respectively. After removing the photoresist and SiO_2 film, the top surface of the samples was spin-coated with a thick layer of bisbenzocyclobutene (BCB). The BCB was plasmin etched using RIE until a 300 nm of the top layer uncovered. Negative photoresist was spin-coated then on the top surface to define the p-type metal contact patterned that consist of Ti (7 nm):Au (350 nm) which evaporated using vacuum thermal evaporation (VTE). All the samples then were annealed at 420^0Cfor 30s followed by polishing the substrate to 110 μm thickness before the n-type metal contact that consist of Ni (4 nm): Ge (20 nm):Au (200 nm) is deposited. Finally, all the sample were cleaved to the same waveguide length of 800 μm with 4 μm width.

Table 3.5-1, Recipes for SiN_x/ SiO_yN_x film composition sorted with respect to their refractive index.

Power (W)	Temp ^0C	NH_3 (sccm)	SiH_4 (sccm)	HE (sccm)	N_2O (sccm)	Refractive Index	Wavelength (nm)	Shift direction
100	250	9	190	200	30	1.59	1392	Blue
100	250	8	190	200	30	1.69	1448	Blue
25	250	0	200	0	412	1.81	1490	Blue
100	250	4	190	200	30	1.89	1515	Blue
100	250	12	200	400	0	1.95	1553	Same as As-grown
150	250	8	200	400	0	2.01	1585	Red
150	250	6	200	400	0	2.09	1613	Red
150	250	4	205	400	0	2.19	1660	Red
150	250	4	210	400	0	2.23	1687	Red

It has been found that increasing the ratio between NH_3 and SiH_4 in the grown SiN_x and SiO_yN_x films results in higher refractive index[49]. Accordingly, the absolute value of the laser spectrum is experiencing a red shift with larger ratio in SiN_x film and blue shift with smaller ratio in SiO_yN_x film, fig.3.5-1.

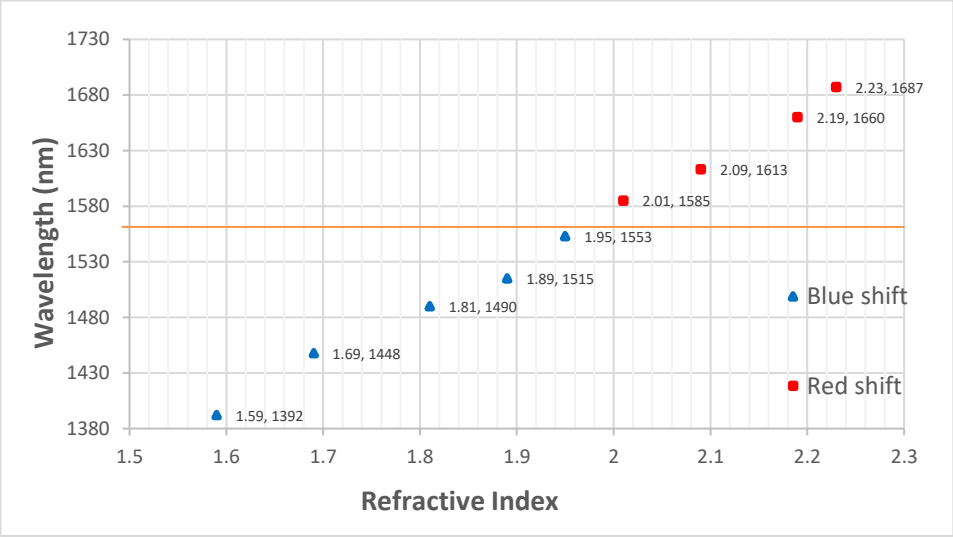

Figure 3.5-1, Measured absolute value of laser spectrum for different dielectric film capping, in respect to the refractive index of the film. The blue shift associated with SiO_yN_x films while the red shift associated with SiN_x.

The as grown semiconductor laser diode has been fabricated as a reference, which has a wavelength of 1556 nm. After implementation of intermixing recipes from table 3.5.1, each fabricated device has shown different wavelength depending on the applied recipe. Figure 3.5-2 shows the corresponding laser diodes spectrum for each refractive index. The highest blue shift is 1392 nm, while the highest red shift is 1687 nm. The p-n junction of uncapped device was damage which prevented the device from lasing due to high annealing temperature. Consequently, it is important to use SiN_x and SiO_yN_x films as a protection layer in high temperature annealing step.

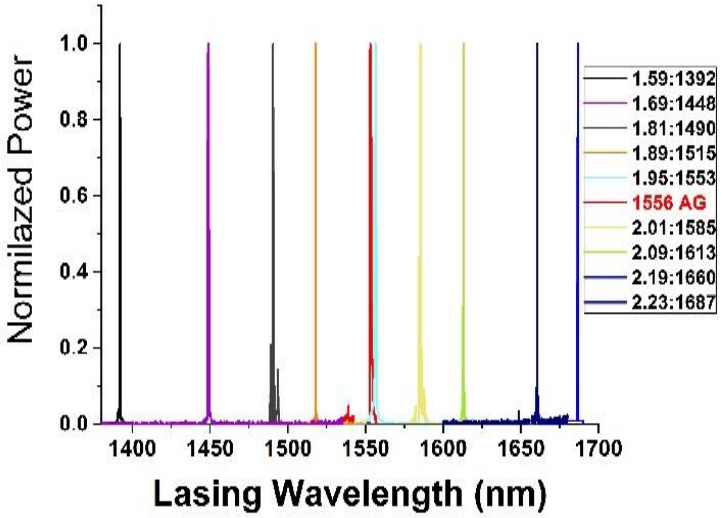

Figure 3.5-2, Laser spectrum of the fabricated devices that treated samples from that of the as-grown wafer for different dielectric film capping, It shifted to the right of the laser spectrum for red shift or for the blue shift.

The variation of the slope efficiency for different fabricated laser diode have been scrutinized. We found that as the lasing wavelength shifted either to blue or red, the slope efficiency gradually decreases because of the diffusion of zinc in to the active region which increases optical losses[50], as shown figure 3.5-3. As expected, the as grown laser has the highest slope efficiency.

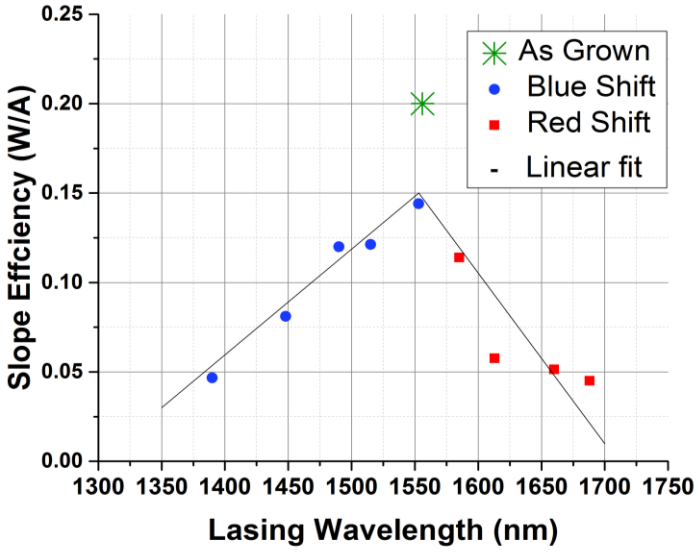

Figure 3.5-3, the fabricated laser diodes and their slope efficiency for as grown, red, and blue shifted lasers.

In contrast, the current threshold has shown an opposite behavior. The threshold current steadily increases with the change of the intermixing[51]. The as grown laser has the lowest threshold current, figure.3.5-4.

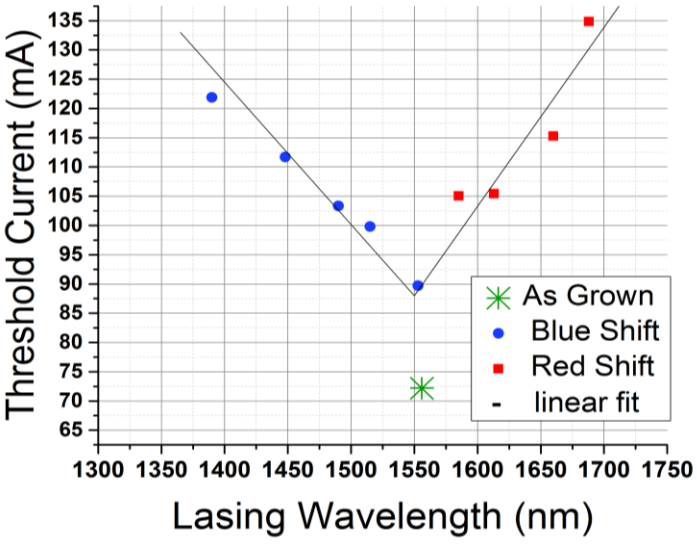

Figure 3.5-4, the fabricated lasers diode as function of threshold current.

Figure 3.5-5 show the output power curve (L-I curve) for all intermixed laser devices. The laser that fabricated using the most intermixed MQWs had the lowest output power while the as-grown laser diode has the highest output power. Therefore, as we intermixed more as we create more losses that

effect the device efficiency.

.

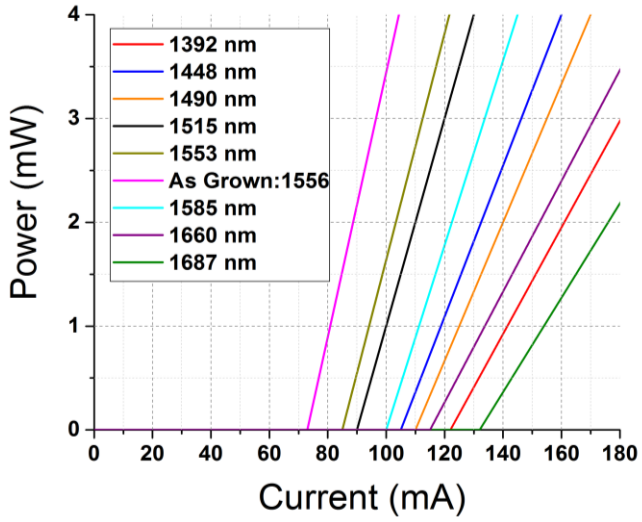

Figure 3.5-5, The L-I curve for all fabricated laser diodes.

In a separate experiment, we have measured the waveguide losses using Hakki-Paoli technique using the gain of the Fabry-Perot device was measured using the threshold the and net gain is given by equation 3.5.1

$$g_{net} = \Gamma g - \alpha_i - \alpha_m = \frac{1}{L}\ln\left[\frac{\sqrt{(p^+/p^-)}-1}{\sqrt{(p^+/p^-)}+1}\right], \quad (3.5.1)$$

Where *P*- is the intensity of valley (local min) and *P*+ is the intensity of peak (local max). The spectrum of the light emission was measured from the devices when we apply current that is very close to threshold current. Then we capture the amplified spontaneous emission from the device on high resolution optical spectrum analyzer as shown in figure 3.5-6. These fringes are basically the Fabry-Perot modes of the cavity. Therefore, the peak to valley is the contrast ratio of those fringes that are related to the losses in the cavity through the Hakki-Paoli Technique.

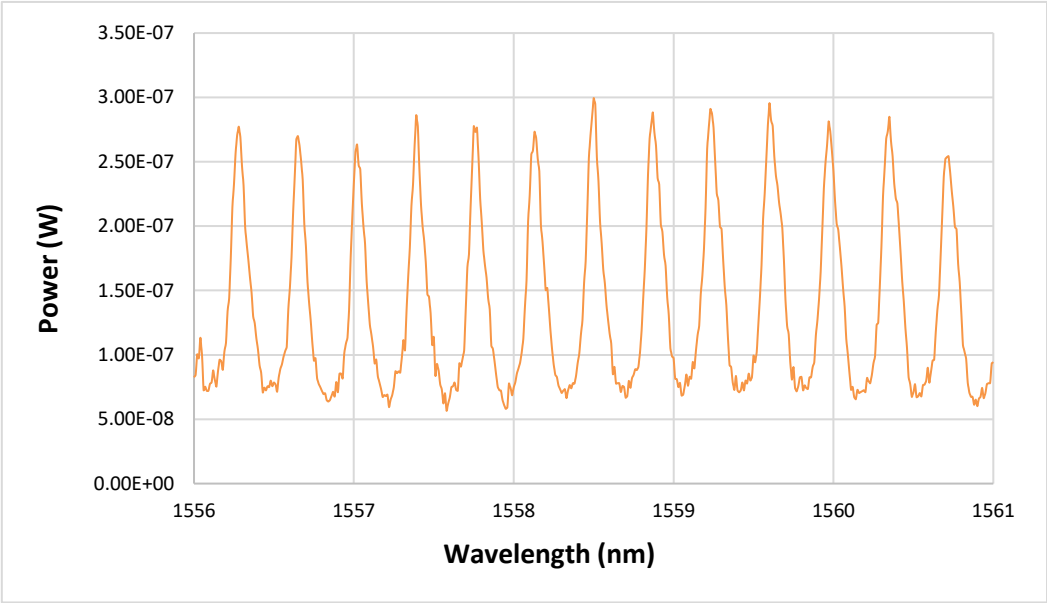

Figure 3.5-6, The Fabry-Perot modes of the cavity below threshold and with high resolution.

Therefore, Intermixing does appear to introduce additional waveguide losses. As grown has the lowest waveguide losses due to the absence of disordering in the active region compare to the intermixed region. The waveguide losses increase as we shifted to the blue or red as shown in figure 3.5-7. In this figure, each bar represents a device that has been intermixed differently and the height of the bar indicate the waveguide losses.

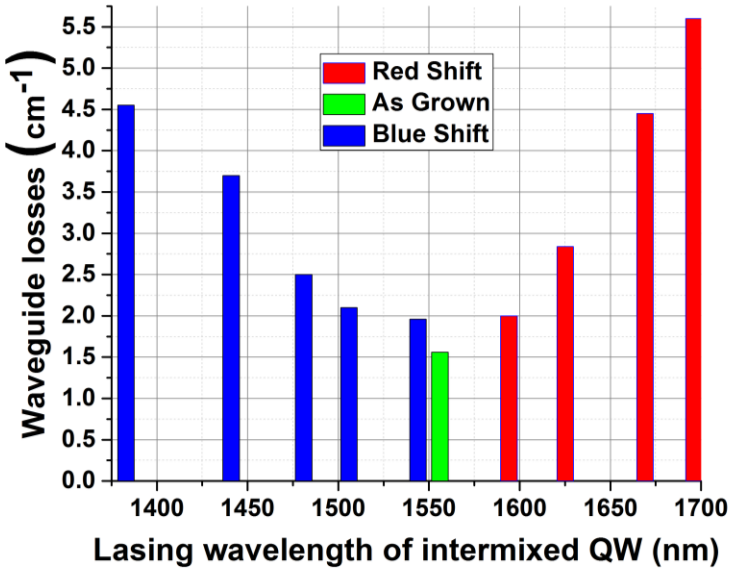

Figure 3.5-7, the fabricated devices Vs the waveguide losses for the as grown, blue, and red shifted lasers.

3.6. Conclusion

We have demonstrated the effects of intermixing on InGaAsP quantum wells laser diodes. We were able to control the laser wavelength either to red or blue shift by changing the ratio of intermixed films. Additionally, the uncapped device was not able to lease because the high annealing temperature. We have shown that, the as grown sample has the best efficiency, lowest losses, and lowest threshold current. However, as we shift the lasing spectrum to either red or blue, the laser will suffer from dropping in efficiency, increase in losses, and increase in threshold current.

By knowing our InGaAsP multiple quantum wells limitation and the intermixing results for both LED and Laser devices, we were able to fabricate our novel tunable laser as upcoming chapter 5. Also, manipulation of bandgap energies on a single chip can enable applications that require a wider spectral bandwidth that give us the ability to integrate and fabricate multiple optoelectronics devices that could be used in different applications as seen in chapter 4.

.

CHAPTER 4: PHOTONICS INTEGRATED DEVICES BASED ON QUANTUM WELL INTERMIXING TECHNIQUES

4.1. Dual wavelength single waveguide laser diode fabricated using selective area quantum well intermixing.

4.1.1. Overview

A two-section single stripe laser diode has been fabricated from a strained InGaAs/GaAs single quantum well heterostruture grown on GaAs substrate. The two sections have different bandgap energies owing to selective area intermixing that is achieved by rapid thermal annealing of the sample with the two sections capped by silicon oxynitride (SiO_xN_y) and silicon dioxide (SiO_2) respectively. The device is capable of producing laser emission at either 911 nm or 953 nm wavelengths depending on the current applied to either section of the laser stripe.

4.1.2. Introduction

Multiple wavelength emissions from a single aperture laser is useful for many types of spectroscopic applications. Usually this is accomplished by combining the optical beams from multiple lasers using beam-combiners such as waveguide couplers. This leads to unnecessary loss of efficiency and added bulk to the laser system. In this work, we propose and demonstrate a laser diode system that incorporate two sections in tandem. The two sections have different bandgap and therefore are able to lase at the wavelength corresponding to the peak of the gain in their respective regions as long as some current is passed through the non-lasing section to keep it above the optical transparency level. A selective area quantum well intermixing process is employed that involves vacancy diffusion through rapid thermal annealing of the sample capped by either silicon dioxide or various silicon oxynitride films. It is shown that the bandgap energy of the intermixed QW structure can be effectively controlled by the composition of the dielectric capping film prior to rapid thermal

annealing of the sample. Using a single InGaAs/GaAs quantum well system, the peak wavelength of the photoluminescence can be fine-tuned from 975nm to 910nm.

4.1.3. Experiment and results

The semiconductor wafer employed in this work is a standard graded-index, separate-confinement-heterostructure, single-quantum-well (GRIN-SCH-SOW) strained InGaAs/GaAs design grown by metal organic chemical vapor deposition (MOCVD) on an n-doped GaAs substrate [50]. The epitaxial structure consists of a 200 nm thick n-doped GaAs buffer layer, followed by a 1 μm thick n-doped AlxGa1-xAs lower cladding layer whose aluminum mole fraction x, is then graded from 0.3 to 0 over a 150 nm layer thickness. The active region consists of an 8 nm thick InGaAs QW between two GaAs barrier layers each 5 nm thick. The top p-doped layers consist of a 150 nm thick graded GaAs-$Al_{0.3}Ga_{0.7}As$ followed by a 1 μm thick $Al_{0.3}Ga_{0.7}As$ capped by a 200 nm thick p-doped GaAs. The photoluminescence of the sample exhibited a peak at a wavelength of 975 nm. Table 4.1.3.1 shows the layer structure of the semiconductor laser material

Table 4.1-1, Design of the InGaAs quantum well laser structure grown by MOCVD.

Layer #	Material	Layer Description	Thickness (mm)
0	n-GaAs Substrate		
1	GaAs	buffer layer	0.300
2	$Al_{0.8}Ga_{0.2}As$	n-cladding	1.200
3	$Al_{0.2}Ga_{0.8}As$	buffer layer	0.075
4	GaAs	QW	0.008
5	$Al_{0.2}Ga_{0.8}As$	buffer layer	0.008
6	GaAs	QW	0.008
7	$Al_{0.2}Ga_{0.8}As$	buffer layer	0.008
8	GaAs	QW	0.008
9	$Al_{0.2}Ga_{0.8}As$	buffer layer	0.075
10	$Al_{0.8}Ga_{0.2}As$	p-cladding	1.000
11	GaAs	p-contact	0.100

In order to characterize the selective area QW intermixing of the structure, several samples were coated with 200 nm thick films of silicon oxynitride of varying composition that were grown at 250°C in a PlasmaTherm 790 Series PECVD system[52, 53]. In order to adjust the relative mole fraction of oxygen to nitrogen in the deposited films, different mass flow rates of NH_3 and N_2O are selected during the PECVD growth process. It was found that the films with a higher nitrogen content tended to have a higher refractive index and therefore the films were tagged according to their refractive index as measured by an ellipsometry [49]. The coated samples were heated at 925°C for 30s in a flowing nitrogen atmosphere inside a rapid thermal annealer (RTA)[54]. Photoluminescence (PL) emission spectra from the samples were captured by an Ocean Optics USB2000 spectrometer. Figure 4.1-1. shows the PL spectra from the different samples and figure 4.1-2 shows the peak emission as a function of the refractive index of the cover film. The measurements show that a full control of the emission wavelength from 975 nm to 910 nm is obtained from a semiconductor layer structure that is coated with different films of SiO_xN_y prior to a high temperature rapid thermal annealing.

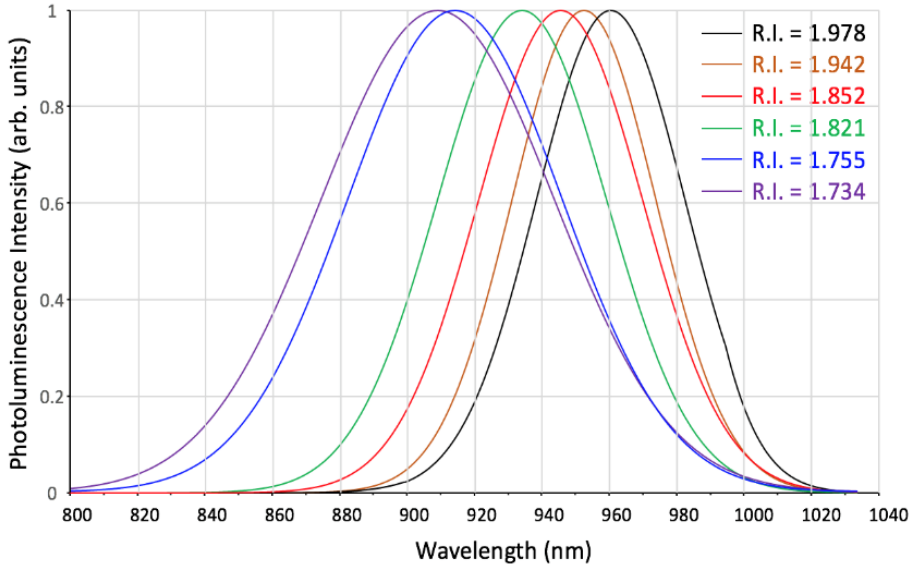

Figure 4.1-1, PL emission spectra of the QW sample after rapid thermal annealing while covered by different SiOxNy films as determined by their refractive indices.

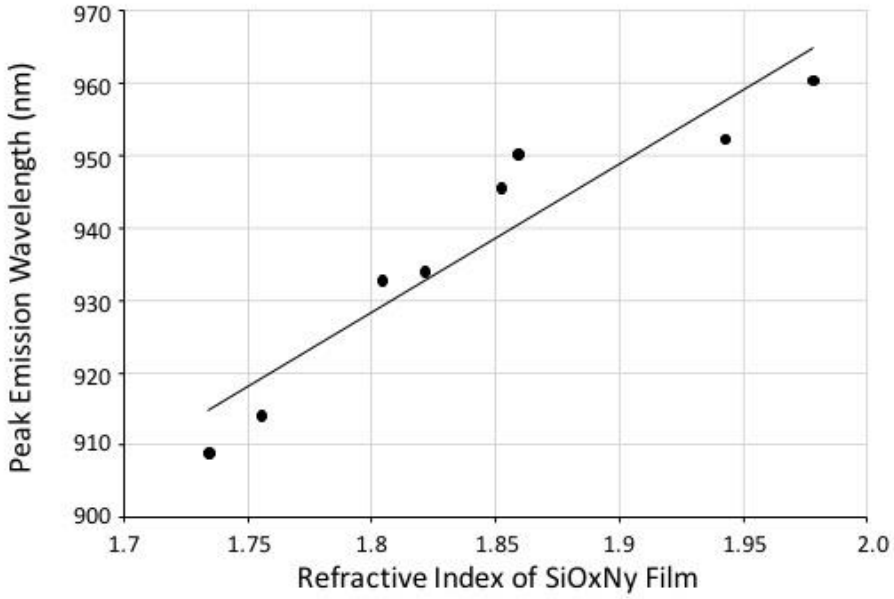

Figure 4.1-2, Plot of peak emission wavelengths as a function of the refractive index for different SiOxNy films.

Two-section single stripe laser diodes are then fabricated using regular photolithographic techniques and wet chemical etching[55]. A small sample of the semiconductor wafer is cleaned with acetone, isopropanol, buffered oxide etch and deionized water and then coated with a 50 nm thick layer of SiO_xN_y that has a refractive index of 1.95[56]. Using photolithography to mask half of the sample with positive photoresist, the exposed SiO_xN_y is removed by reactive ion etching (RIE). After removal of the photoresist, the sample is coated with a 200 nm thick SiO_2 and then heated at 925°C for 30s in an RTA. This process results in two sections of the semiconductor sample with different bandgap energies related to the degree of quantum well intermixing. The QW in the region of the sample that was covered by SiO_xN_y (section A) is intermixed less than in the region covered by SiO_2 (section B). Positive photoresist is spun on top of the SiO_2 and 3 μm wide stripes that run across the two different intermixed sections are delineated using contact mask photolithography[57]. The unwanted SiO_2 and SiO_xN_y layers are removed by RIE and the waveguide ridge is formed by etching the GaAs contact layer and top AlGaAs cladding layer[58]. After removing the photoresist, the whole sample is then spin-coated with a thick layer of bisbenzocyclobutene (BCB), an insulating protective

resin[59, 60]. After curing the BCB in a nitrogen flowing oven for 2 hours at 250°C, the solidified BCB is etched back by RIE until about 350 nm of the top SiO_2 coated waveguide is uncovered. The SiO_2 and SiO_xN_y are then removed by RIE and negative photoresist is spun on the surface followed by photolithography to define 30 μm wide channel openings centered around the waveguide stripes. 10 nm of titanium, followed by 4 nm of zinc followed by 300 nm of gold contact metals are deposited by vacuum thermal evaporation[61]. The unwanted metals are removed by lift-off by dissolving the photoresist in acetone leaving 30 μm wide p-contact metals covering the whole length of the waveguides. A 4 μm wide gap is etched in the contact metal at the interface between the two intermixed sections using photolithography and gold etch consisting of potassium iodide and iodine solution[62]. After sample is cleaned, the metals are annealed at 430°C for 30s. The substrate is then lapped down and polished to a thickness of 120 μm and then coated with 4 nm of nickel followed by 20 nm of germanium and 200 nm of gold by vacuum thermal evaporation to form the n-contact layer[63]. The contacts are finally annealed at 430°C for 30s[64]. The sample is cleaved to a total length of 1450 μm with 650 μm of the waveguide length in section B. Figure 4.1-3 shows a schematic of the two-section laser diode. The device is then mounted p-side up on a copper header and tested on a waveguide alignment setup. A 25X microscope objective lens is used to capture the light emitted from either of the cleaved facets and focus it into the end of an optical fiber that is connected to a spectrometer to monitor the emission spectrum. A power meter is then positioned in the laser beam path to measure the light output power as a function of injected current.

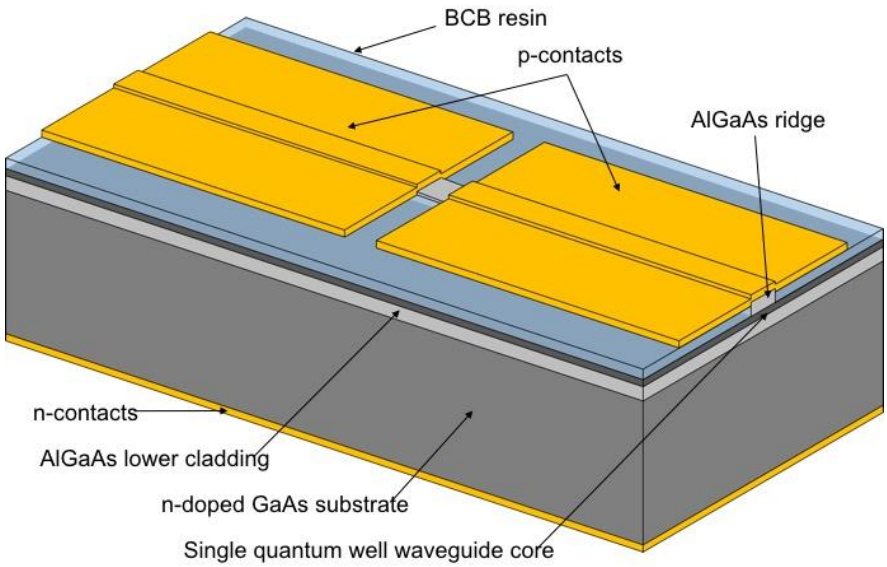

Figure 4.1-3, Schematic of the two-section laser diode device.

Figure 4.1-4 shows the emission spectrum of the light output from the device with 60 mA injected into the section B of the laser device and 4.5 mA injected into section A. The laser emission at 911 nm indicates that the structure of original QW in section B has been altered considerably. Figure 4.1-5 shows the light output as a function of the injection current. The L-I curve was obtained by gradually increasing the current that is applied to the section under test while a fixed 4.5 mA current was applied to the other section. The threshold current for that combination is 26 mA with a current slope efficiency of 0.18 W/A.

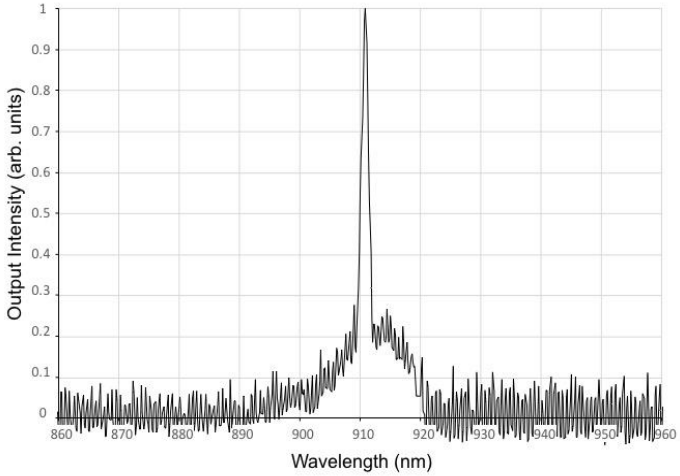

Figure 4.1-4, the spectrum of laser emission spectrum at 911nm with 60 mA injected into section B and 4.5 mA injected into section A.

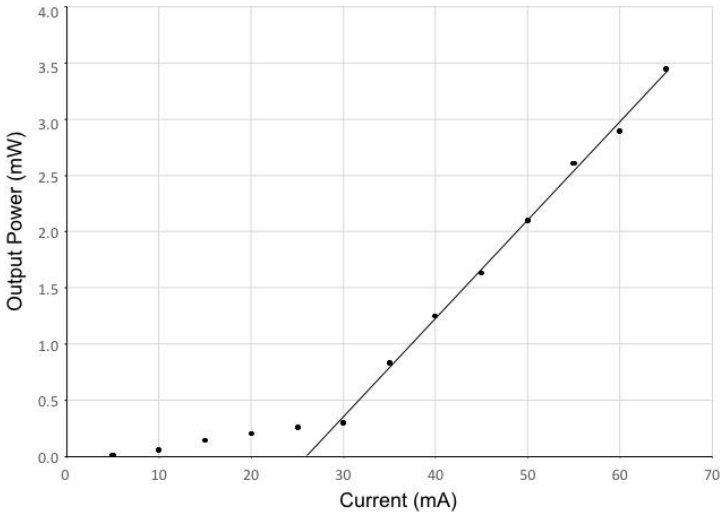

Figure 4.1-5, The L-I curve as a function of current injected into section B of the laser diode with 4.5 mA injected into section A..

Figure 4.1-6 shows the emission spectrum from the same device with 60 mA injected into section A of the device and 3 mA injected into section B. In this case, the laser emission is at 953 nm indicating confirming that the QW in section A is intermixed to a lesser extent than that in section B. Figure 4.1-7 shows the light output as a function of the injection current and indicates a threshold current of 19 mA and a current slope efficiency of 0.056 W/A.

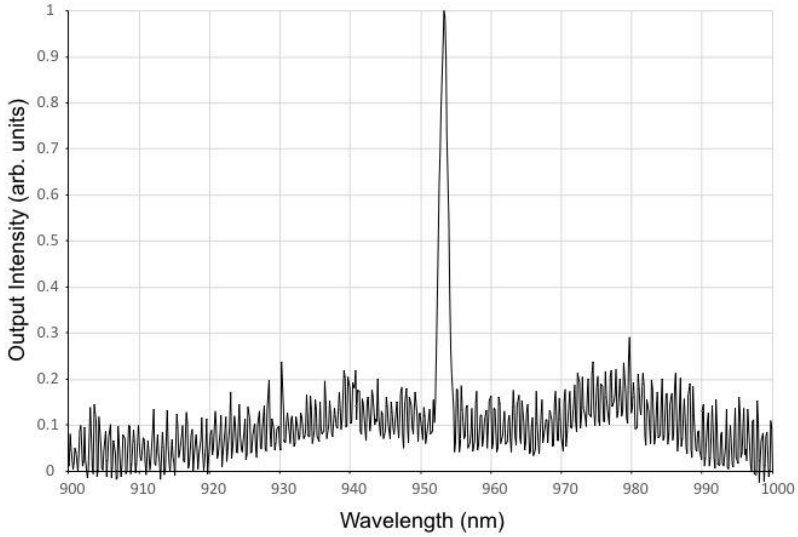

Figure 4.1-6, the spectrum of laser emission at 953nm with 60 mA injected into section A and 3 mA injected into section B.

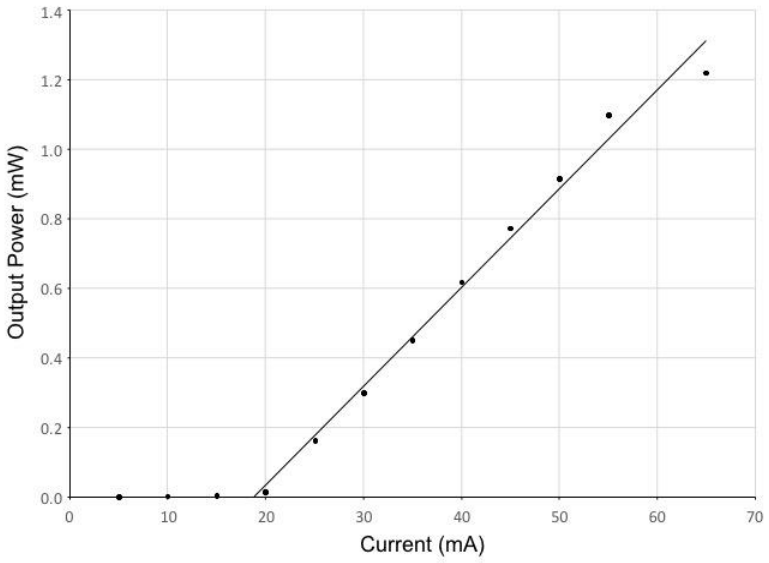

Figure 4.1-7, The L-I curve as a function of current injected into section A of the laser diode with 3 mA injected into section B.

4.1.4. Summary

A two-section single waveguide laser diode has been demonstrated that can lase at two different wavelengths depending on the current injected into the two separate sections. The measurements of the laser L-I responses indicate that the intermixing process does not cause significant deterioration of the active region to an extent that causes laser action to cease and therefore is encouraging for other active devices incorporating multiple selectively intermixed QW regions are feasible.

4.2. Integrated LEDs and modulators on InGaAsP quantum well platform.

4.2.1. Overview

Exploiting a controllable technique for red and blue shifting of quantum well's bandgap energy, we have fabricated LED sources accessing a wide frequency spectrum along with all-optical intensity modulator devices. We demonstrate bandgap tuning of InGaAsP multiple quantum well structures by utilizing an impurity free vacancy diffusion technique. Substantial modification of the bandgap energy toward the red and blue part of the spectrum has been observed using SiO_2, SiO_yN_x, and SiN_x capping layers and by controlling the associated oxygen and nitrogen content. In this work, by utilizing a controllable technique for red and blue shifting of quantum well's bandgap energy, we have developed and fabricated LED sources monolithically integrated with broadband intensity modulator devices that are compatible with the selected spectral frequency of the LED sources. The intensity modulator along with LED sources, designed to reach minimum material losses and residual amplitude modulation Multimode interference (MMI) geometry has been incorporated in the design of the Mach-Zehnder interferometer (MZI) modulator to control the optical intensity of the transmitted LED light. In section 4.2.2, we present the simulations and design of the MMI device that operates as an integrated optical beam splitter. Finally, in section 4.2.3, we present experimental results and fabrication process of a fully monolithically integrated device that includes an LED with a broad spectral emission and a MZI modulator with a high extinction ratio on an InGaAsP quantum well platform.

4.2.2. Design and simulations of MMI based switches and LED

Figure 4.2-1 shows the schematic drawing of a monolithically integrated optical transmitter that includes a LED source and a transparent intensity modulator. The intensity modulator is based on a Mach-Zehnder interferometer (MZI) in which the phase control is achieved by injecting electrons into the core of the waveguide. The MZI is made up of two MMI couplers that serve as integrated optical beam splitters and beam combiners at the input and output of the phase modulation section. The MMI couplers as chosen in the device design owing to their compactness and tolerance to small fabrication inaccuracies, while ensuring equal optical intensities in both phase control arms of the modulator.

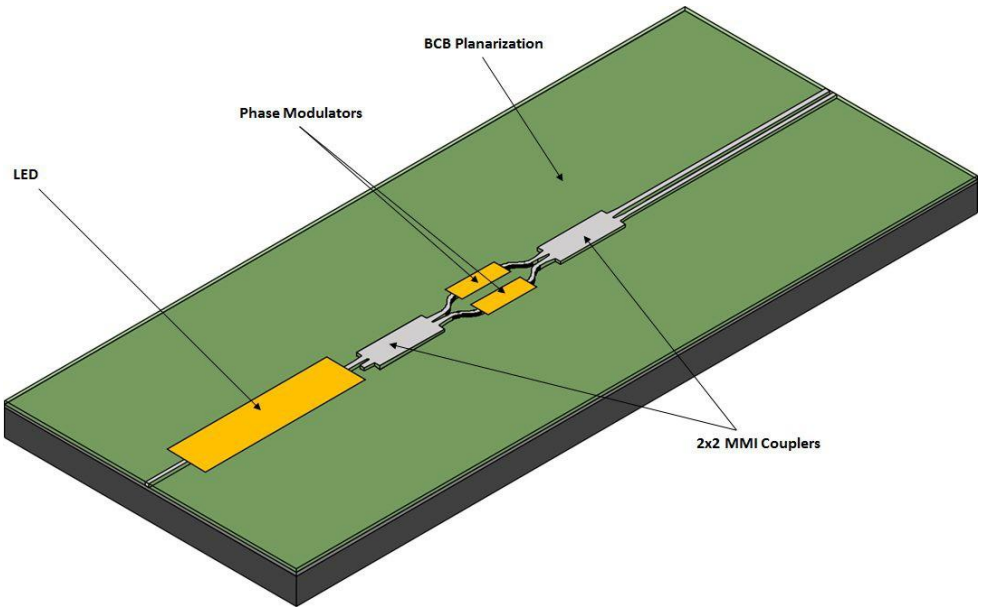

Figure 4.2-1, Schematic view of a completed device with monolithically integrated LED's along a MZI intensity modulator.

Figure 4.2-2 shows the beam propagation in one such MMI device as simulated using a commercial software package (RSoft by Synopsys). In this case, it is observed that equal optical intensity division is achieved after 800 µm propagation distance. The width of the MMI is set at 22 µm and the center to center separation between the waveguides at the input and output is 7 µm.

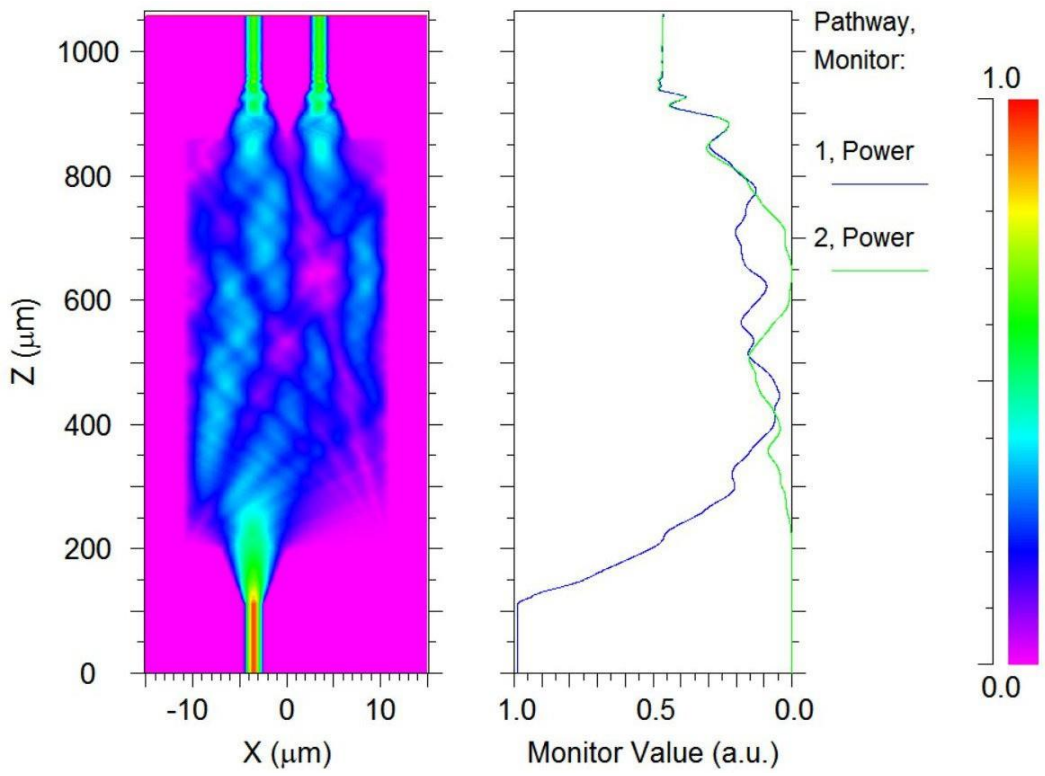

Figure 4.2-2, Simulation of MMI device performed by RSoft, BeamProp package. The device is designed to achieve equal optical power at the output.

4.2.3. Device fabrication and measurements

The samples used in this study were ultrasonically cleaned with acetone, followed by rinsing with isopropyl alcohol (IPA) and deionized (DI) water to remove debris and organic residue from the exposed surfaces. The samples were then immersed in buffered oxide etch (BOE) to remove any native oxide from the surface. In this experiment, a 30 nm thick film of SiN_x film was deposited by PECVD on the top layer. The regions of the MQW that needed to be protected from disordering were delineated using photoresist and photolithography. The other parts of the SiN_x is removed by RIE. After cleaning off the photoresist, a 200 nm thick film of SiO_2 was deposited over the whole surface for the purpose of intermixing the regions of the semiconductor in contact with the SiO_2 film. The samples were then annealed at 775^{o}C for 30 seconds in a nitrogen atmosphere. The sample with

selected regions that have been disordered, and still covered by the SiN_x and SiO_2 films, was then coated with photoresist. The device structures were then photolithographically patterned into the photoresist. These patterns were then transferred into the SiN_x and SiO_2 films by RIE and then the uncovered regions of the top InGaAs layer were removed using a mixture of H_3PO_4:H_2O_2:H_2O in a volume ratio of 1:1:30 respectively. The unwanted InP layer was then etched off using a 1:1 mixture of HCl: H_3PO_4. After all the waveguide structures have been delineated, the originally deposited SiN_x and SiO_2 films were then removed completely using RIE. The top surface was planarized by spin-coating the sample with benzocyclobutene (BCB) resin (commercially known as Cyclotene), and etching it off until only about 200 nm of the top InGaAs layer was exposed. P- type contact metals consisting of Ti, Zn, and Au were then deposited on top of the waveguides that operate as LEDs and phase modulation sections. The sample was annealed at 430ºC for 30s to improve the adhesion of the metal contacts to the surface of the semiconductor. Figure 4.2-3 shows microscope photographs of the fabricated device after the metal deposition from top view. The sample was then lapped and polished to a final thickness of 120 nm before the n-type contact metals (Ni, Ge, and Au) were deposited on the substrate side of the devices. The sample was cleaved to an overall length of 6.5 mm and mounted on a temperature controlled heat-sink.

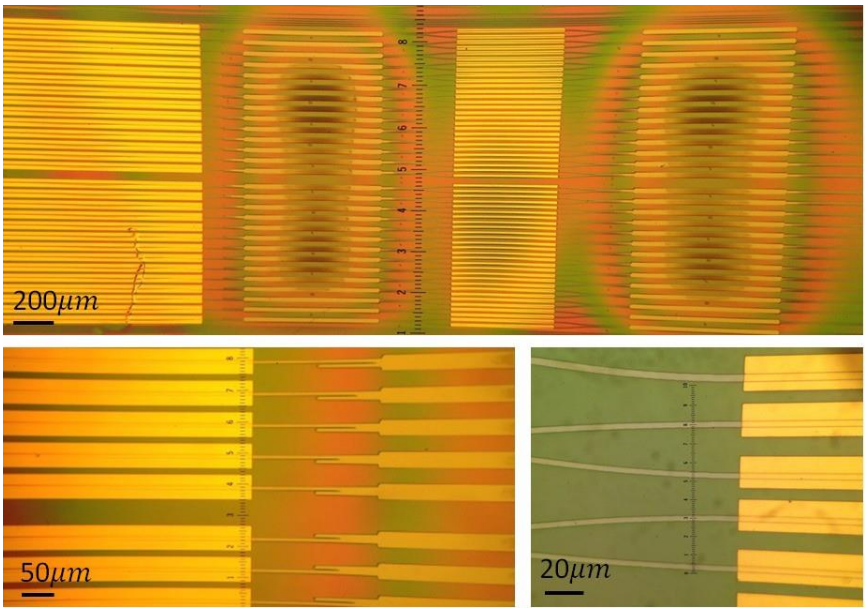

Figure 4.2-3, Fabricated device containing two sets of MMI, and LEC source and a MZI in between. The scales have been changed for clarification for the device.

Figure 4.2-4, shows the scanning electron microscopy (SEM) pictures of the final coupler device. This device has been fabricated to merely characterize the losses and the directional coupler, thus it only includes the coupler section design and LED source.

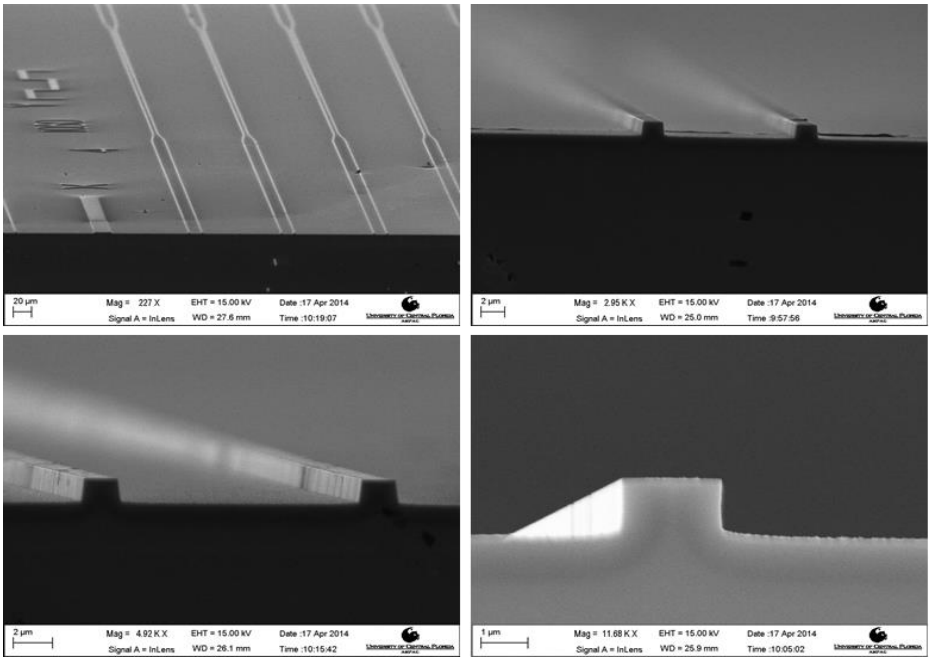

Figure 4.2-4, SEM pictures of the coupler device.

4.2.4. Results

In the regions of the sample where the MQWs were covered by SiNx film during the rapid thermal annealing, and consequently were not disordered, the ridge waveguides with electrical contacts on top conveniently form edge emitting p-i-n LEDs. The I-V characteristics of the LEDs exhibit clear diode behavior with about 5mA flowing with a 1V forward bias whereas it appears as an open-circuit when driven in reverse bias with the current driver. The light output from the LED waveguide was captured by a lens and directed to a power meter. Figure 4.2-5 shows the light vs current (L-I) response of one such LED as well as its emission spectrum which is centered at 1547 nm.

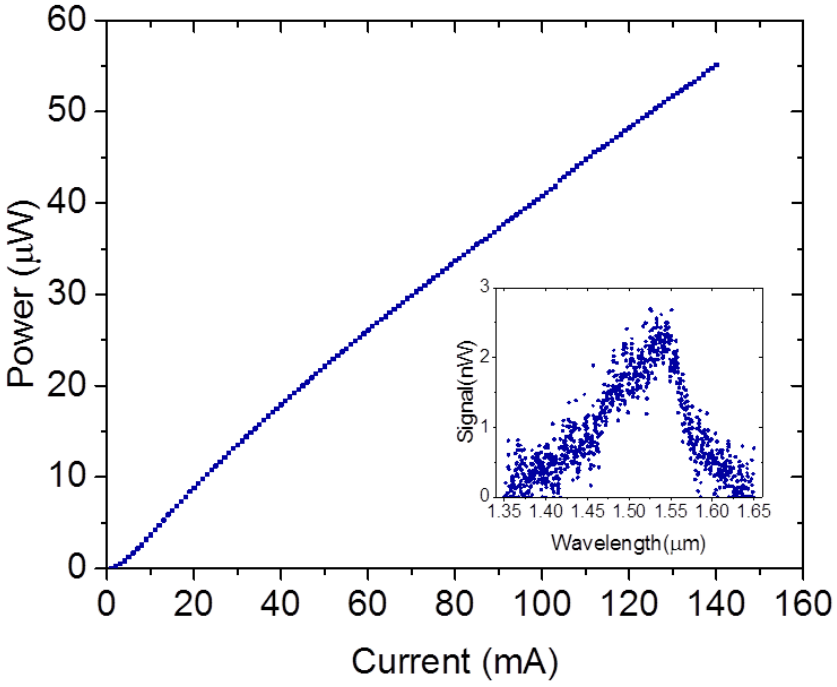

Figure 4.2-5, The L-I curve one of the LED devices. The inset shows the spectrum of the LED at a current of 100mA.

Almost equally divided between the two output waveguides. With 1.47 mA injected into the waveguide, all of the optical power was switched to the left output port. Figure 4.2.-6 shows the switching characteristics of the integrated MZI modulator and figure 4.2-7 show the output modes of the modulator. It is evident that the current needed to achieve a π-phase shift in one arm of the

interferometer is only 1.47 mA. However, the measurements also indicated that beyond that current level, the phase modulation was no longer pure and there was an onset of current induced intensity change in one arm of the interferometer leading to incomplete interferometric cancellation at the second MMI. This resulted in a diminished extinction ratio at the second switching half-cycle. Furthermore, the second switching current occurred at 4.7 mA which was significantly larger than double the switching current for the first half-cycle, indicating an onset of saturation of the electron density induced refractive index change.

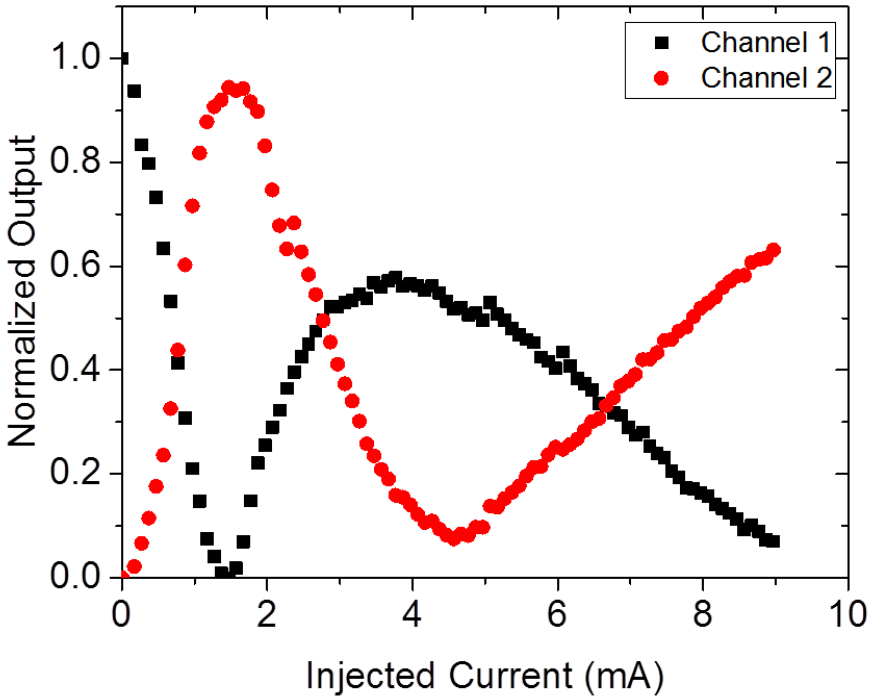

Figure 4.2-6, Measured optical power at the output of each port as a function of the injected current.

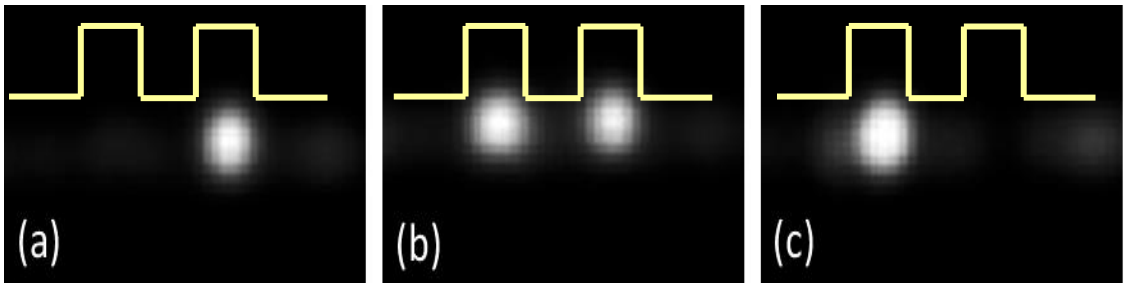

Figure 4.2-7, Images of the output mode from the modulator facet

4.2.5. Summary

In conclusion, we have developed a method of area selectively disordering MQWs for the purpose of fabricating active monolithically integrated optoelectronic circuits. In this work, we report the fabrication of an integrated LED transmitter composed of a broadband LED source and an inline MZI modulator with two MMI couplers/splitters. The optical transmitter with a spectral bandwidth of about 100 nm (FWHM) operates at a switching current of 1.47 mA.

CHAPTER 5: TUNABLE LASER DIODE USING SELECTIVELY INTERMIXED INGAASP MULTIPLE QUANTUM WELLS

5.1. Introduction

Tunable laser diodes are vital for environmental sensing applications requiring spectroscopic measurements such as chemical and biological agents' detection. In addition, the tunable laser has played a crucial role in many applications that demand simple tunable sources with broad wavelength ranges such as photochemistry, optical communications, and many other spectroscopic and sensing applications. Furthermore, tunable laser diodes present an attractive solution to many challenges in dynamic networks with wavelength reconfigurability and optical communication networks that require complex multiplexing processes. Sorokin and Lankard, and Schäfer were first to demonstrated a tunable laser using the organic dye laser in 1966 [1, 2].Presently, distributed Bragg reflector (DBR) and distributed feedback (DFB) tunable lasers are already being used in many network applications. In those lasers, DBR and DBF geometries along with, phase-controlling sections, form the wavelength-selective mirrors for the optical cavity, [3–4]. There are spectroscopic applications that do not require the narrow spectral bandwidth of DFB lasers. In such applications, simple wavelength tunable semiconductor Fabry-Perot laser diodes can be fabricated more easily and the wavelength control circuitry is much simplified. In this work, we demonstrate an InGaAsP multiple quantum well tunable laser diode that amalgamate two gain sections with different bandgap energies. This is achieved using selective area intermixing of the multiple quantum wells using impurity-free vacancy induced disordering. This technique is usually performed by selectively capping the MQW sample with SiNx or SiOxNy dielectric layers and thermally annealing it to expand or shrink the bandgap energy [5, 6]. Using plasma enhanced chemical vapor deposition (PECVD), half of the sample is coated with a 30nm silicon nitride (SiN_x) film followed by a 200nm

thick overlay of silicon oxynitride (SiO_xN_y) film over the entire sample. The whole sample is then thermally annealed at 750°C for 30s, and that results in the SiO_xN_y covered section experiencing a narrowing of the bandgap energy, while leaving the SiN_x covered section practically unchanged. A laser stripe is fabricated that passes through both MQW sections. The wavelength of laser operation can then be tuned by varying the injected current levels applied separately to the two sections. The bandgap energy of the MQW section capped by a SiNx layer (Section A) remains unchanged at a corresponding wavelength of 1560 nm. Meanwhile, the bandgap wavelength of the section capped by SiOxNy layer is blue shifted to 1530 nm. Different current combination was injected to each section. Wavelength tuning is achieved by varying the two currents ratio. When the currents injected in the two sections are varied, the combination of the gain spectra leads to a laser wavelength in the overall effective gain whose peak position depend on the magnitudes of the two injected currents. The fabricated device was capable of producing laser emission that was tunable from 1538 nm to 1578 nm with almost constant output power from 1544 nm to 1566 nm.

5.2. InGaAsP MQW structure.

In this work, the gain medium consists of five InGaAsP quantum wells that were grown by metal organic chemical vapor deposition (MOCVD) on a Si doped InP substrate at a commercial semiconductor foundry. The undoped active multiple quantum well (MQW) layer has a bandgap wavelength of 1560 nm and consists of five undoped InGaAsP quantum wells each 8 nm thick sandwiched between undoped layers of 15nm thick InGaAsP barriers with a total thickness of 275 nm. This together with two undoped spacers of InGaAsP forms the core of the waveguide. An additional layer of InGaAsP, 50 nm thick, is incorporated 100 nm above the active core layer to act as an etching stop layer during the fabrication process which is useful for determining the actual

depth of the devices. The top cladding layer is a 900 nm thick layer of Zn-doped InP followed by a 100 nm thick Zn-doped InGaAs layer. The details of the wafer design are shown in table 5.2.1

Table 5.2-1, InGaAsP multiple quantum wells laser structure design grown by MOCVD

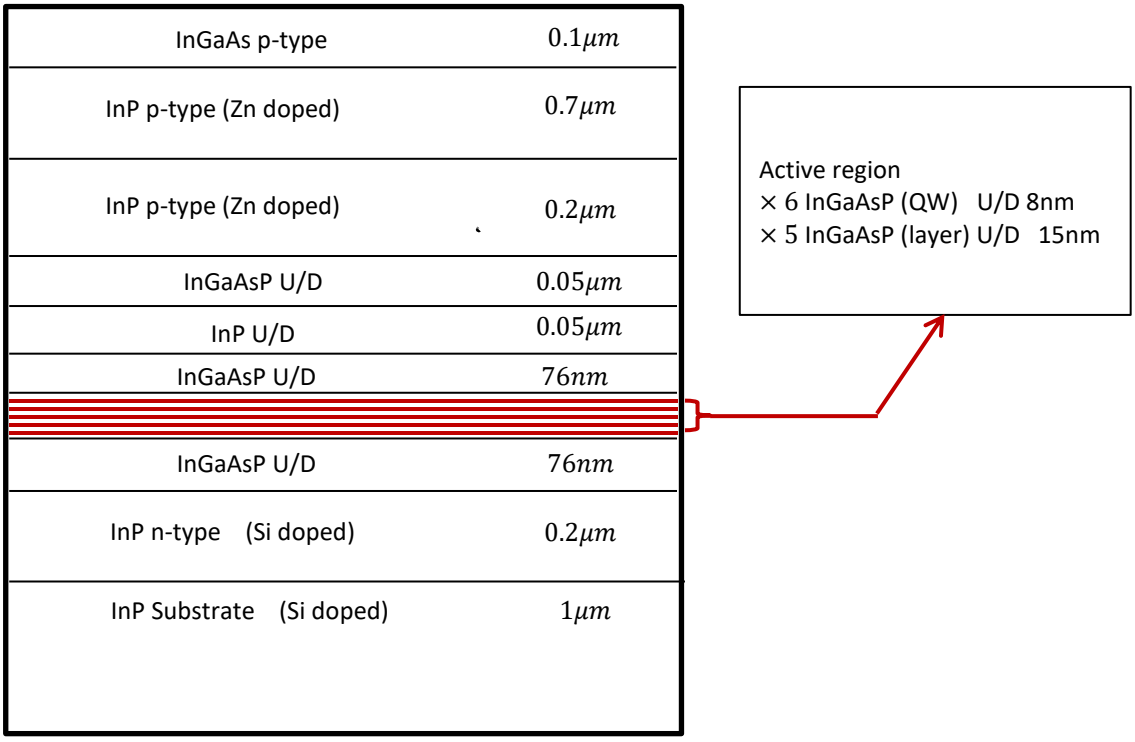

5.3. Fabrication process

In order to characterize the controllability of the selective area QW intermixing process, several samples were capped by SiN_x or SiO_yN_x films of varying compositions grown at 250°C using a Plasma-Therm 790 Series plasma-enhanced chemical vapor deposition (PECVD) system [65]. Different mass flow rates of NH_3 and N_2O are selected during the PECVD growth process to adjust the ratio of nitrogen to oxygen in the final composition of the coated films[66, 67]. It was found that as the ratio between NH_3 and N_2O was increased, the refractive index as measured by an ellipsometry, tended to increase. However, in the absence of N_2O component, the SiN_x film exhibit a higher refractive index by decreasing the ratio between SiH_4 to NH_3 as shown in table 5.3.1. The coated

samples were then heated in a flowing nitrogen atmosphere at 750°C for 30s using a rapid thermal annealer (RTA)[68].

Table 5.3-1, InGaAsP MQW tunable Laser capping layer films ratio.

Power (W)	**Temp (°C)**	**NH_3 sccm**	**SiH_4 sccm**	**He sccm**	**N_2O sccm**	**Refractive Index**	**Wavelength (nm)**	**Shift Direction**
100	250	15	180	200	30	1.89	1513	Blue
100	250	18	200	200	32	1.81	1490	Blue
100	250	9	180	200	30	1.69	1448	Blue
100	250	4	180	200	30	1.59	1392	Blue
100	250	10	200	400	0	1.95	1553	Same as As-grown
150	250	7	200	400	0	2.01	1585	Red
150	250	5.5	200	400	0	2.09	1613	Red
150	250	4	200	400	0	2.19	1660	Red
150	250	4	210	400	0	2.23	1687	Red

For the two-section device reported in this work, we have selected a SiN_x film that protected the MQW from intermixing with the photoluminescence (PL) peak remaining at 1560 nm and a SiO_yN_x film that resulted in the sample experiencing a PL peak shift to 1530 nm as shown in Figure 5.3-1.

x

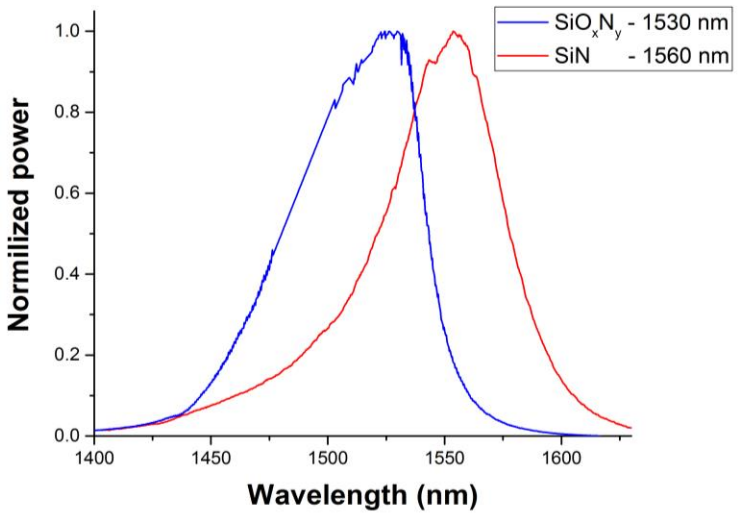

Figure 5.3-1, PL emission spectra of the MQW device after rapid thermal annealing while covered by different SiN_x and SiO_yN_x films corresponding to their refractive indices.

The device fabrication was started by coating the MQW sample with a 30 nm thick SiN_x film that has a refractive index of 1.96. It was necessary to keep the film thickness to 30 nm or less, to avoid film cracking because of the high stress that occurred during high temperature annealing of the sample. Using photolithography and reactive ion etching (RIE), the SiN_x film was removed over half of the sample [57, 69]. The whole sample was re-coated with a 100 nm thick film of SiO_yN_x and then heated at 750°C for 30s in a nitrogen flowing rapid thermal annealer (RTA). The high temperature annealing process created two distinct sections of the sample with one side containing basically non-intermixed MQWs (section A coated with SiN_x) and the other side containing intermixed MQWs (section B coated with SiO_yN_x) whose bandgap energy was blue shifted according to the degree of quantum well intermixing[70]. The films of SiN_x and SiO_yN_x were removed by RIE and the sample was then coated with a 200 nm thick film of SiO_yN_x to serve as a mask during the wet chemical etching of the ridge waveguides. Positive photoresist was spun on top of the SiO_yN_x and 4 μm wide stripes of SiO_yN_x that run perpendicularly across the two different intermixed sections were delineated using contact mask photolithography and RIE. The waveguide ridges were then formed by wet etching of the top layers of InGaAs, InP, and the etch stop layer of InGaAsP using selective

etchant mixtures of H_2O_2(1):H_2O(25):H_3PO_4(3), H_3PO_4(1):HCl(1) and H_2O_2(1):H_2O(10):H_2SO_4(1) respectively[71]. After the SiO_yN_x film was removed, a 3 μm thick layer of bisbenzocyclobutene (BCB), an insulating protective resin, was spin-coated on top of the sample. The BCB film was cured in a nitrogen flowing oven that was programmed for a constant temperature of 250°C for 1 hour followed by 200°C for 30 minutes and 150°C for 30 minutes[72]. The BCB film was thinned down using RIE until 250 nm of the top of the waveguide ridges were uncovered. Negative photoresist was then spun on the top surface of the sample followed by photolithography and lift off process to define 20 μm wide p-type metal contacts that covered the top of the waveguide strips while leaving a 3 μm wide gap at the interface between the two intermixed sections. The metal contact deposited by vacuum thermal evaporation, consisted of a 10 nm thick layer of titanium, followed by a 400 nm thick layer of gold. The sample was annealed at 400°C for 30s and the substrate was lapped down and polished to a thickness of 100 μm. After the sample was thoroughly cleaned, the n-type metal contact that consisted of a 4 nm thick layer of nickel followed by a 20 nm thick layer of germanium, and finally by a 200 nm thick layer of gold, was then deposited by vacuum thermal evaporation and the sample was again annealed at 400°C for 30s[72]. Finally, the sample was cleaved off into three separate arrays of laser devices as shown in figure 5.3-.2 and 5.3-3. One device contained an array of 600 μm long laser diodes in the non-intermixed MQWs ($\lambda_{PL} = 1560$ nm). The second device contained an array of 600 μm long laser diodes in the intermixed MQWs ($\lambda_{PL} = 1530$ nm). The third device contained an array of 800 μm long laser diodes with a 400 μm section spanning the intermixed MQWs and the other section spanning the non-intermixed MQWs. Each of the devices was mountedwith the p-side up, using electrically conductive silver epoxy, on a copper header that served as the ground terminal as well as a heatsink.

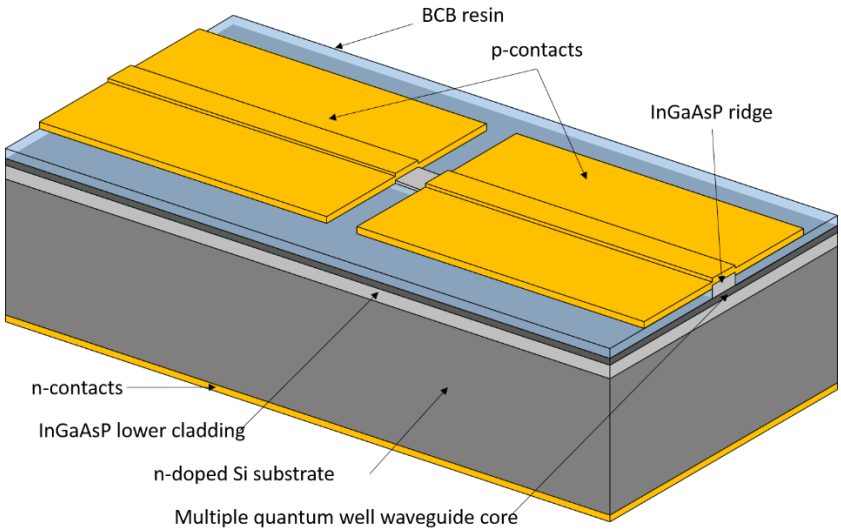

Figure 5.3-2, Schematic of the tunable laser diode device after cleaved.

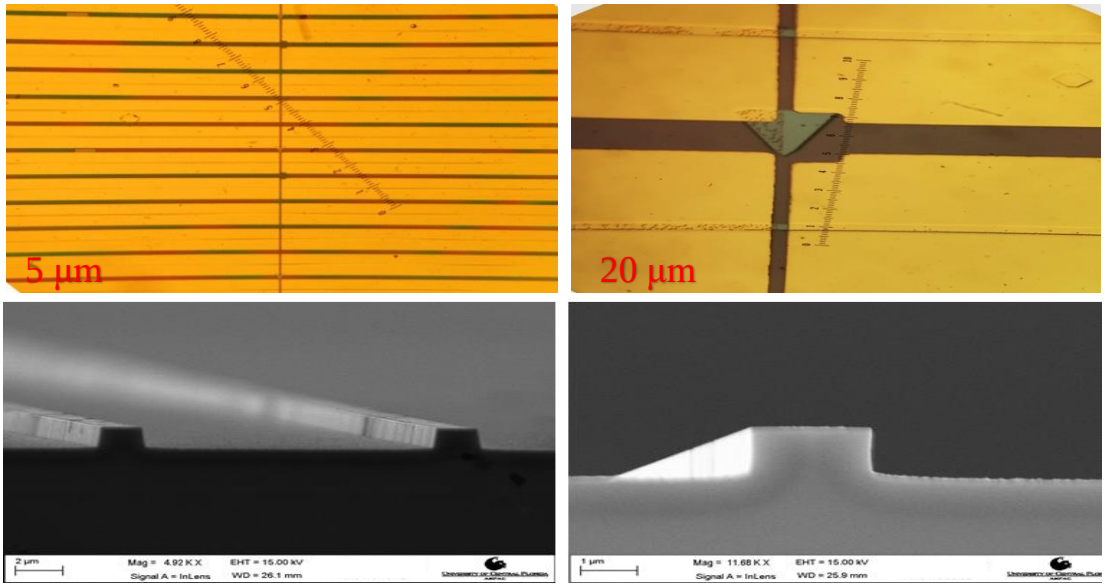

Figure 5.3-3, Top view of the actual tunable laser diode the scales has been changed for clarification for the device. In the below picture is the tunable laser waveguide picture taking by SEM.

5.4. Measurements and results

The devices are mounted p-side up on a copper header and their operation characteristics were measured using a waveguide alignment setup. The laser light emitted through one of the cleaved facets, was collected by a 40X microscope objective lens and focused into the open end of an optical fiber that is connected to a to an optical spectrum analyzer (OSA) to monitor the emission spectrum. A beam-splitter is inserted between the objective lens and the end of the fiber to project the output

light onto a power meter to monitor laser output power as a function of the injected current. Figure 5.4-1 shoe the experiment setup.

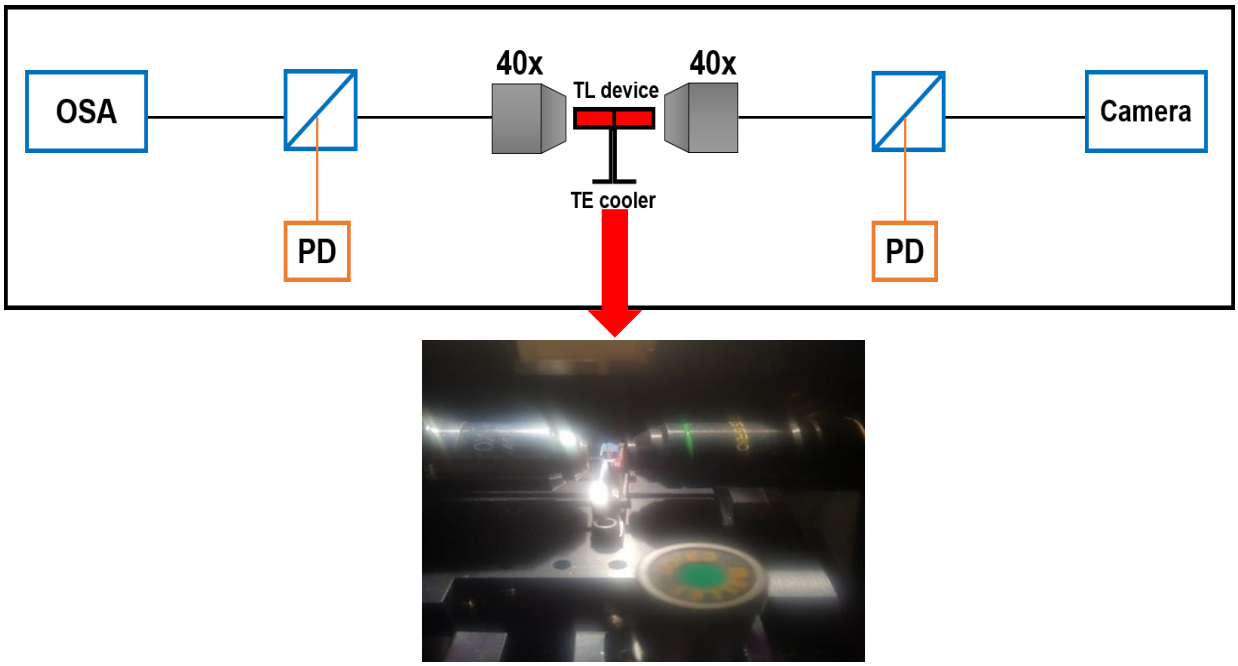

Figure 5.4-1, Schematic for the experiment set-up and the real device.

The three cleaved arrays were tested separately. Figures 5.4-2 shows the emission spectrum of the light output from the laser diodes that contained the un-intermixed MQWs section A. Figure 5.4-3 shows the output power as a function of injection current that exhibits a slope efficiency of 0.28 W/A with a laser threshold current of 42 mA. It was also observed that the laser wavelength increased by 1nm when the input current was increased from 100 mA to 200 mA and this is attributed to thermal effects due to insufficient heat-sinking.

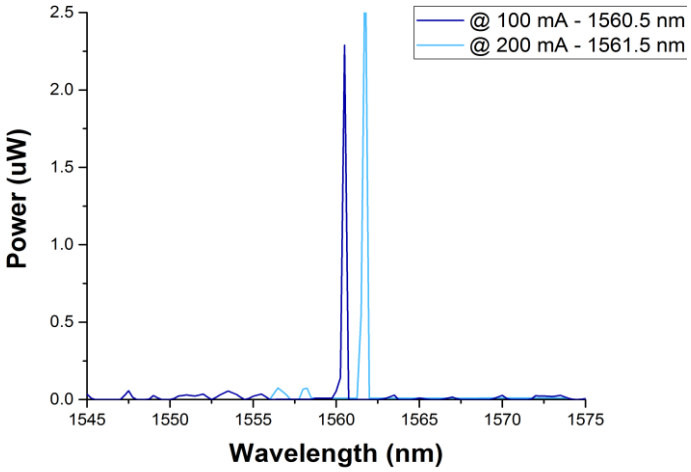

Figure 5.4-2, the laser spectrum for the non-intermixed MQWs (Section A)

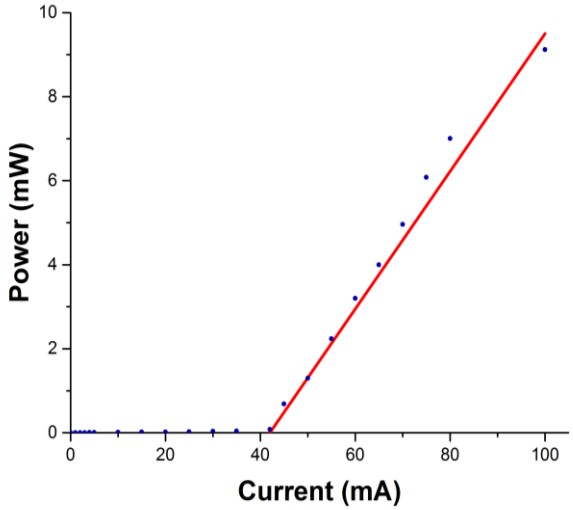

Figure 5.4-3, The L-I curve as a function of injected current into section A.

The results for the laser diodes fabricated with the intermixed MQWs are shown in figures 5.4-4 and 5.4-5. Here the laser diodes operated with a threshold current of 45 mA and the slope efficiency was .216 W/A. Again, it was observed that when the current was increased from 100 mA to 200 mA, the lasing wavelength increased by 1nm, this time from 1560 nm to 1561 nm.

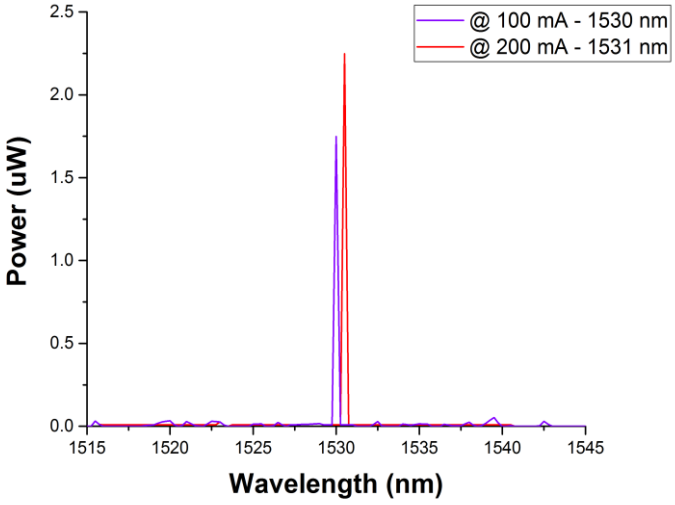

Figure 5.4-4, the laser spectrum for the intermixed SiO_xN_y (Section B) at 1530 nm with 100 mA and at 1531 with 200 mA.

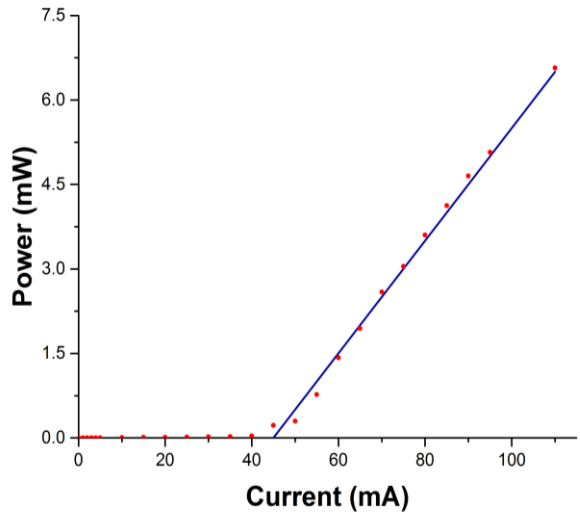

Figure 5.4-5, The L-I curve as a function of injected current into section B.

Finally, the two-section laser diode device that contained both un-intermixed section A (λ_{PL} = 1560 nm) and intermixed section B (λ_{PL} = 1530 nm), was tested. Wavelength tuning is achieved by injecting current separately in the two gain sections. When the currents injected in the two sections are varied, the combination of the gain spectra leads to a lasing wavelength whose position depend on the relative magnitudes of the two injected current. The laser wavelength tuning that is obtained by changing the currents combinations is shown in table 5.4.1

Table 5.4-1, the laser wavelength tuning range as function of the injected currents I_A and I_B in the sections A & B.

Section A (mA)	Section B (mA)	Total injected current (mA)	Power (mW)	Wavelength (nm)	Section A (mA)	Section B (mA)	Total injected current (mA)	Power (mW)	Wavelength (nm)
12	55	67	0.08	1550	65	30	95	0.79	1539
12	65	77	0.33	1553	65	35	100	1.09	1542
12	75	87	0.726	1553.5	65	45	110	1.16	1545
12	85	97	0.924	1557	65	55	120	1.19	1547
12	95	107	0.957	1560	65	65	130	1.20	1549
12	105	117	1.108	1561.5	65	75	140	1.21	1551.3
12	115	127	1.04	1563	65	85	150	1.21	1552.8
12	125	137	0.726	1566	65	95	160	1.21	1555
25	42	67	0.211	1544	65	105	170	1.15	1558
25	50	75	0.851	1548	75	25	100	0.34	1540
25	65	90	1.122	1550.2	75	35	110	1.08	1544
25	75	100	1.157	1553.5	75	45	120	1.14	1546.5
25	85	110	1.193	1556.3	75	55	130	1.17	1548
25	95	120	1.20	1557.3	75	65	140	1.19	1551
25	105	130	1.20	1560	75	75	150	1.20	1554.2
25	135	160	1.20	1565.7	75	85	160	1.21	1557.4
35	35	70	0.211	1542	75	95	170	1.21	1562
35	45	80	0.99	1545	75	105	180	1.22	1566.8
35	55	90	1.13	1547.8	85	20	105	0.21	1537
35	65	100	1.16	1550	85	35	120	1.15	1545
35	75	110	1.18	1551.8	85	45	130	1.20	1549
35	85	120	1.18	1554.8	85	55	140	1.21	1553
35	95	130	1.19	1555.9	85	65	150	1.22	1556
35	105	140	1.19	1557.3	85	75	160	1.27	1560
35	115	150	1.20	1559.3	85	85	170	1.29	1565.8
45	30	75	0.198	1540	85	95	180	1.36	1568.9
45	45	90	1.12	1545	85	105	190	1.43	1573
45	55	100	1.16	1547.7	100	100	200	1	1578
45	65	110	1.18	1549.3	95	98	192	1.08	1575

45	75	120	1.19	1550.8	55	45	100	1.14	1544.7
45	85	130	1.20	1553.3	55	55	110	1.17	1546.7
45	95	140	1.20	1555	55	65	120	1.19	1549.4
45	105	150	1.21	1557.6	55	75	130	1.20	1551.2
55	25	80	0.34	1538	55	85	140	1.21	1553.4

The tunable laser that contained both intermixed and non-intermixed sections was then tested by applying separate currents to the two sections. For this device to lase, electrical current needed to be injected into both sections at the same time. It was observed that the lasing wavelength of the tunable laser could be shifted effortlessly from 1538 nm to 1578 nm. The lasers spectra plotted in figure 5.4-6 are discrete samples of the continuously tunable lasing wavelengths that were achieved. .The tuning range was 40 nm from 1538 nm to 1578 nm as shown in figure 5.4-6.

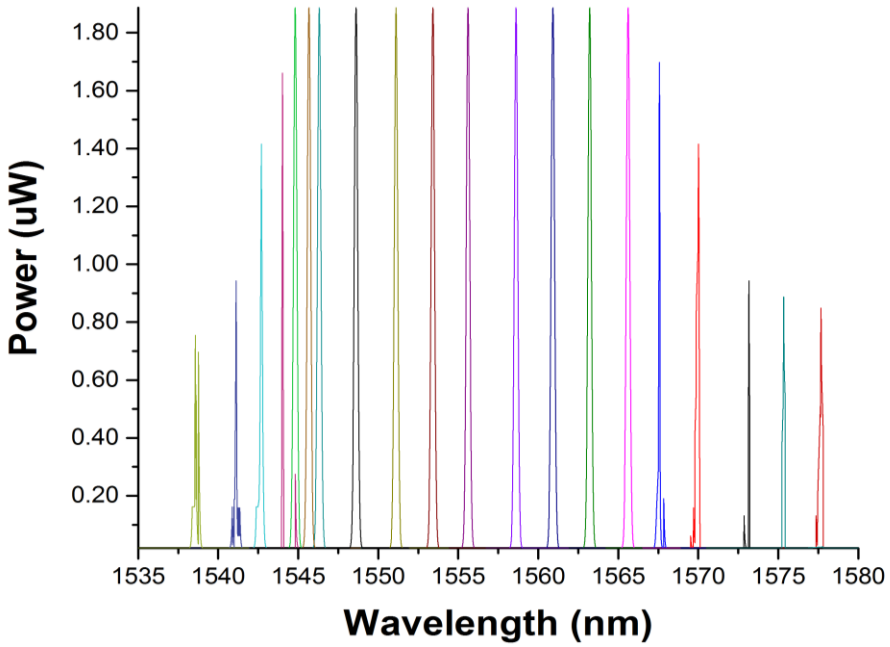

Figure 5.4-6, the laser spectra obtained from the two-sections laser diode with different currents applied into the two sections.

The tuning of the laser wavelength was controlled by changing the currents injected in the two sections independently. By keeping the current applied to section A at 12 mA, while increasing the current in section B, the laser wavelength was tuned from 1544 nm to 1564 nm. Whereas when the

current applied to section A was kept at 25 mA, while increasing the current in section B, the laser wavelength was tuned from 1542 nm 1567 nm. Similarly, by changing the two currents systematically, we were able to fine tune the output laser light from 1538 nm to 1578 nm as shown in figures 5.4-7 and 5.4-8.

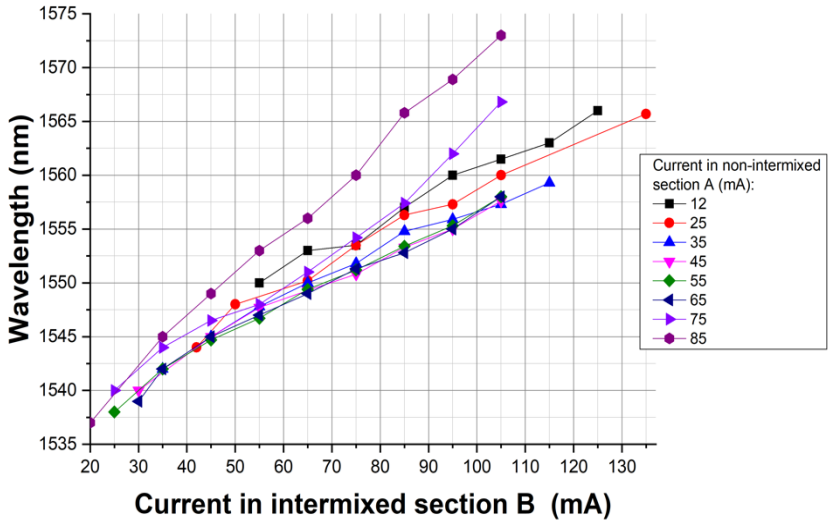

Figure 5.4-7, Wavelength tuning achieved by different currents composition IA and IB.

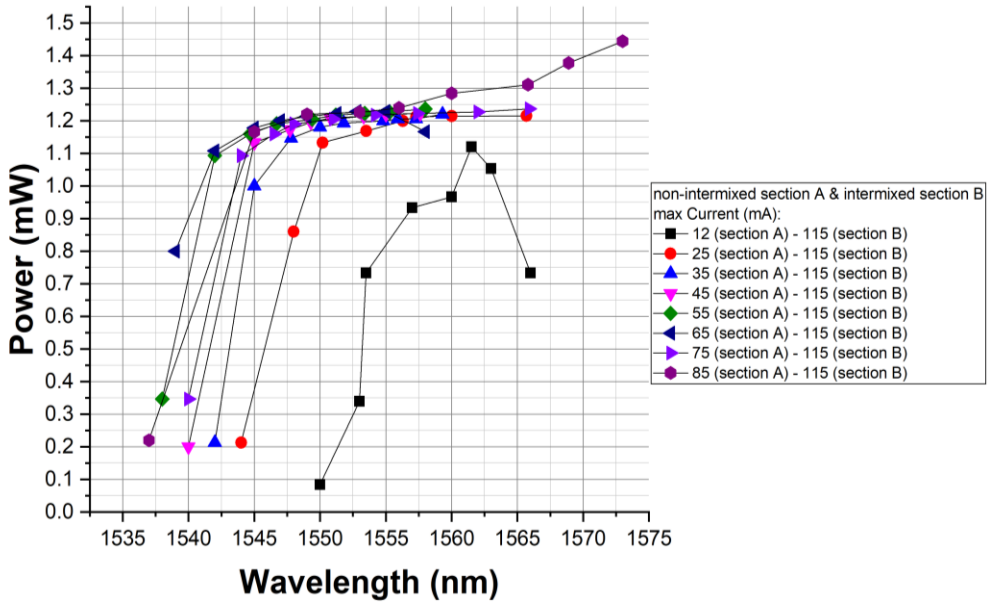

Figure 5.4-8, Output power as function of laser wavelength.

By carefully adjusting the two injection currents, we were able to obtain continuously variable lasing wavelength, while maintaining constant output power, as shown in figure 5.4-9. Table 5.4.2 shows examples of the range of wavelengths that were achieved with constant output powers of 1.1 mW, 1.086 mW, and 1.056 mW respectively[73]. For the whole range of various power and wavelength compositions can be found in appendix A. It was observed that about 10 nm of wavelength tuning could be achieved with a fixed output power.

Table 5.4-2, some examples of output power stability at different wavelength tuning with different current compositions.

Current in section B (mA)	Current in section A (mA)	Output power (mW)	Wavelength (nm)
35	115	1.1	1559.3
45	105	1.1	1557.6
55	85	1.1	1553.4
65	75	1.1	1551.6
65	65	1.1	1550.2
25	85	1.1	1557.2
85	45	1.1	1549
25	75	1.056	1553.5
35	65	1.056	1550
45	55	1.056	1547.7
55	45	1.056	1544.7
85	35	1.056	1545
75	45	1.056	1546.5
65	45	1.056	1546.4
75	65	1.086	1551
65	55	1.086	1547
55	65	1.086	1549.4
45	75	1.086	1550.8
95	95	1.086	1555.9
105	105	1.086	1557.3
25	85	1.086	1556.3

As the total injected current was increased, the output power of the tunable laser increases almost linearly up to 1 mW but then appear to saturate around 1.25 mW as shown in figure 5.4-9. Any value of the total injected current exceeding 100 mA, can produce a wavelength tuning range of about 20 nm by adjusting I_A and I_B ratio as shown in figure 5.4-10.

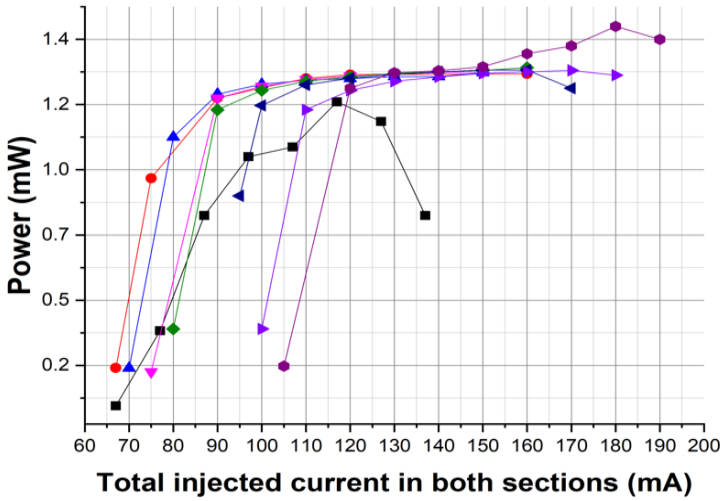

Figure 5.4-9, Output power as function of total injected currents in both sections I_A+I_B.

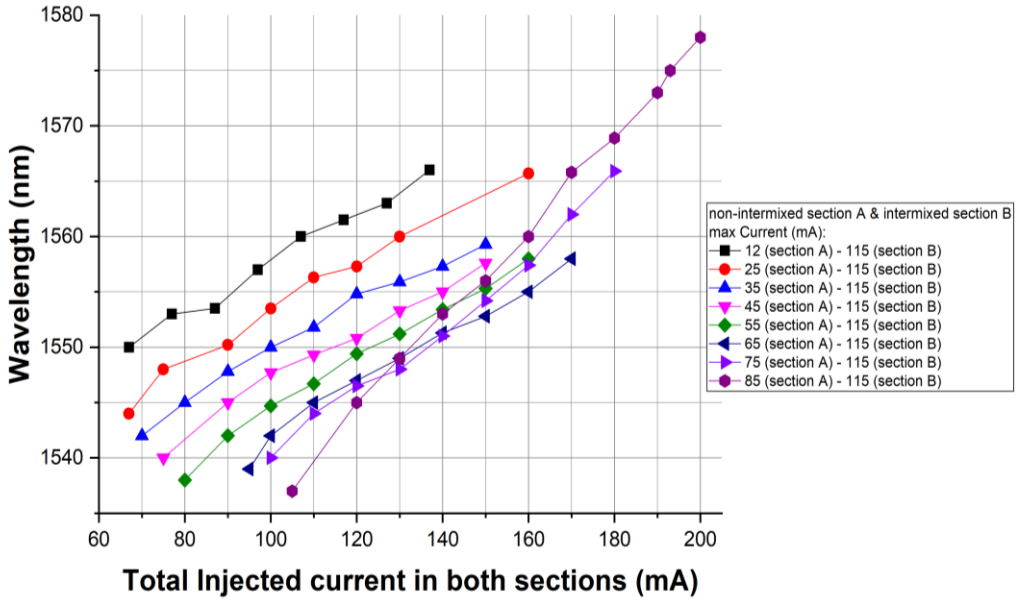

Figure 5.4-10, Wavelength tuning with different currents applied to the two sections.

5.5. Summary

Using a controlled technique for selective area intermixing of InGaAsP MQWs, a two-section laser diode whose wavelength of operation can be tuned by varying the injected current applied to the two sections has been demonstrated. The fabricated device was capable of producing laser emission that was tunable from 1538 nm to 1578 nm depending on the currents injected into the two sections. The continuous wavelength tuning could be achieved with a fixed output power.

CHAPTER 6: SURFACE PLASMON RESONANCE SENSOR (SPRS)

6.1. Introduction

With the rapid growth and demand for biological sensing instruments, there has been an increased emphasis on more versatile and reliable biomolecule detection systems. The motivation is continually growing especially with the rising health consciousness and an ageing world population. One of the well-known biological agent sensing devices, which is usually made up of a transducer and a biological element, is the affinity-based biosensors. The biological element in the biosensor is mainly used for recognizing the substance of interest that needs detection while the transducer is used for converting one form of energy into another- in this case, converting the bio-recognition event into a measureable electric signal. Currently, there is a variety of transducers that have been developed for biosensors, examples include optical, electrochemical and piezoelectric transducers. Among these, optical methods such as interferometry, fluorescence spectroscopy, surface plasmon resonance (SPR) spectroscopy and evanescent wave-based detection are incredibly popular. Although fluorescence based detection methods, such as Enzyme-Linked Immunosorbent Assay (ELISA), has been implemented over the years because of their high sample throughput and device sensitivity, the new detection process now needs time-consuming labelling treatment with multi-steps of detection protocol[74-76]. Although the SPR based bimolecular detection technology is relatively new, detection systems based on such schemes have been successfully commercialized. Furthermore, this method does not need any labelling procedures while it facilitating real-time monitoring with high sensitivity. However, these SPR sensors, especially the current commercial and developing ones, have low throughput and a relatively bulky system size. In general, these features limit the range of application of the SPR sensors. While some of the problems have been partially resolved, there is still a need for higher throughputs and a more compact and even disposable SPR system [77-83].

In this project, we have demonstrated an optical surface plasmon resonance (SPR) sensor

head that is based on an inverted rib dielectric waveguide, in which the resonance wavelength of the surface plasmon excited at the gold metal-dielectric interface. The inverted-rib waveguide of the SPR sensor head is made of a layer of SU-8 polymer with a refractive index of 1.568 while the lower cladding layer consists of silicon oxynitride (SiO_xN_y) with a refractive index of 1.526. The top surface is coated with a 50 nm thick layer of gold. The SPR sensor head was designed to allow monitoring of analyte media with a refractive index ranging from 1.44 to the 1.524. Using a set of reference liquids representing the analyte medium, the sensitivity of the SPR sensor was measured using a three different input light source namely, erbium doped fiber, semiconductor optical amplifier, and commercial tunable laser. All of the measurements were taken separately. It was found that with a liquid of 1.442 refractive index in contact with the chrome and gold metal, a sharp resonance dip in the transmission spectrum occurred at 1525 nm and its position shifted to 1537 nm when a liquid of 1.502 was used. Another SPR sensor was fabricated using the same cladding films but different contact metals consisting of thin layers of titanium and gold. Thus, to improve the sensor sensitivity. The sensitivity for chromic-gold SPR sensor devices was determined to be S = 232 $nm.RIU^{-1}$ and 334 $nm.RIU^{-1}$for the titanium-gold one. We demonstrate that this device can potentially be partially integrated with a wavelength tunable light source as shown in chapter 7.

6.2. Surface Plasmon Resonance (SPR)

Surface plasmon is transverse magnetic surface electromagnetic waves that propagate at the gold metal-dielectric interface. The propagation constant is given by the following dispersion relation, equation 6.2.1[84-87].

$$k_{sp}(\omega) = \frac{\omega}{c}\sqrt{\frac{\varepsilon_M \varepsilon_D}{\varepsilon_M + \varepsilon_D}} \tag{6.2.1}$$

6.3. Configurations for Surface Plasmon Excitation

The surface plasmon can exist if the real part of its dielectric constant is negative and its magnitude is greater than that of the underlying dielectric medium. In the case of a surface plasmon wave on the top surface of the metal, it can be excited by a light wave whose tangential component of its wavevector is equivalent to that of the surface plasmon wave as indicated in equation 6.3.1[88, 89].

$$\beta(\omega) = k_{sp}(\omega) \tag{6.3.1}$$

6.4. Optical waveguide based surface plasmon excitation

Surface plasmon resonance condition is achieved when the wavevectors of a guided mode with that of the surface plasmon are perfectly matched. When this condition is satisfied, there is an efficient transfer of energy from the incident guided light must be guided to the surface plasmon wave and consequently the intensity of the transmitted waveguide mode is significantly reducted. A representation of such a device is shown in figure 6.4-1[90-93].

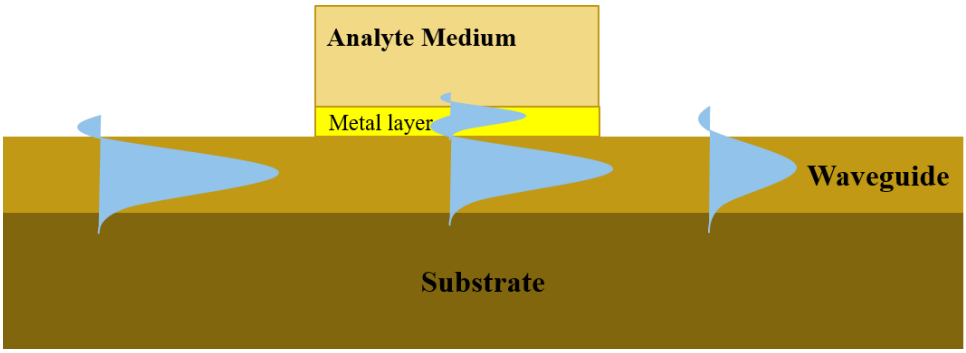

Figure 6.4-1, Optical waveguide based surface plasmon excitation configuration.

6.5. Energy transmission through SPR Sensor Head

Mode transmission happens by changing the eigenmodes at the boundary, when light passes through the SPR sensor head. as shown in figure 6.5-1. In this figure only single mode transmitted through the SPR sensor head due to the waveguide geometry. In the proposed SPR sensor head, the mode conversion happens at the abrupt boundaries, before and after the sensor head [94-96]. Furthermore, two modes can be excited if the waveguide geometer and refractive index of the analyte medium designed to allow double mode condition as can be calculated using equation 6.5.1.

$$a_{\nu\mu} = 2\int_{-\infty}^{+\infty}\int E_i \times H_{\nu\mu}^{*} dxdy \qquad (6.5.2)$$

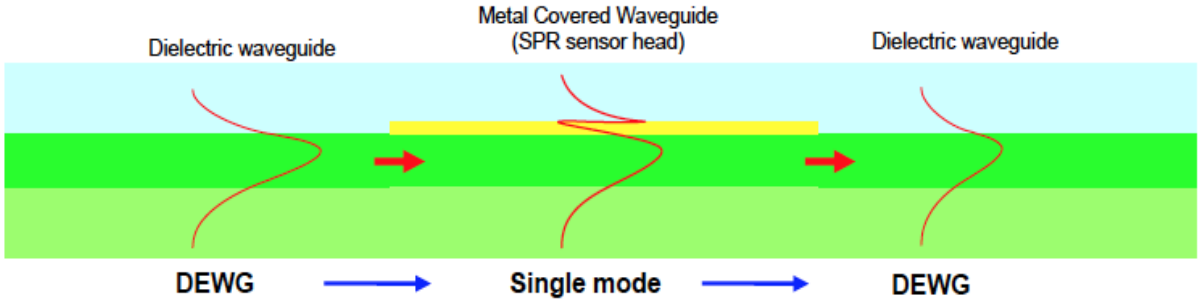

Figure 6.5-1 , Energy transmission process of an integrated optical SPR sensor in a single mode guide condition.

6.6. Waveguide Geometry

The inverted rib waveguide was designed to only support the fundamental TM guided mode. The height and the width of the waveguide was designed and fabricated based on waveguide dispersion relationship equation 6.6.1[97].

$$t_g = \frac{\operatorname{atan}\left(\sqrt{\frac{{n_s}^2 - {n_c}^2}{{n_g}^2 - {n_s}^2}}\right) + \pi}{k_o\sqrt{{n_g}^2 - {n_s}^2}} \qquad k_o = \frac{2\pi}{\lambda}\ is\ the\ free - space\ propgation\ constant \tag{6.6.1}$$

The refractive index of the analyte medium that is in contact with the gold metal will result in a specific surface plasmon resonance wavelength. The theoretical dependence was calculated (table 6.6.1) using matching condition requirement for the propagation constant of the surface plasmon equation 6.6.2[98].

$$\beta = \beta' + i\beta'' \approx \frac{\omega}{c}\sqrt{\frac{\varepsilon'_m \cdot \varepsilon_d}{\varepsilon'_m + \varepsilon_d}} + i\frac{\varepsilon''_m}{2(\varepsilon'_m)^2}\frac{\omega}{c}\left(\frac{\varepsilon'_m \cdot \varepsilon_d}{\varepsilon'_m + \varepsilon_d}\right)^{3/2} \tag{6.6.2}$$

ε_m : Dielectric constant of metal,

ε_d : Dielectric constant of cover material

Table 6.6-1 , refractive index of the analyte medium that will result in a surface plasmon resonance with different wavelength.

Analyte medium refractive index	Surface Plasmon refractive index	Theoretical wavelength nm
1.44	1.463	1539.5
1.47	1.484	1533.8
1.49	1.504	1530
1.5	1.515	1528.1
1.518	1.533	1524.68
1.51	1.5255	1526.2

6.7. Film characterization

The precise values of the refractive indices of the guiding and cladding layers are critical. In order to define the wavevectors of the guided mode and hence satisfy the matching condition to launching a SP mode. Therefore, the refractive indices for both films need to be characterized carefully to design the SPR sensor head. The guiding layer of the SPR sensor head was made with SU-8 polymer and the buffering layer was made of silicon oxynitride (SiO_xN_y) film.

6.7.1 SU-8 refractive index

The guiding layer of the SPR sensor head was made with SU-8 polymer. The SU-8 polymer has a fixed refractive index that is corresponding to the wavelength value. At 1550 nm the refractive index found to be 1.568 as shown in figure 6.7-1.

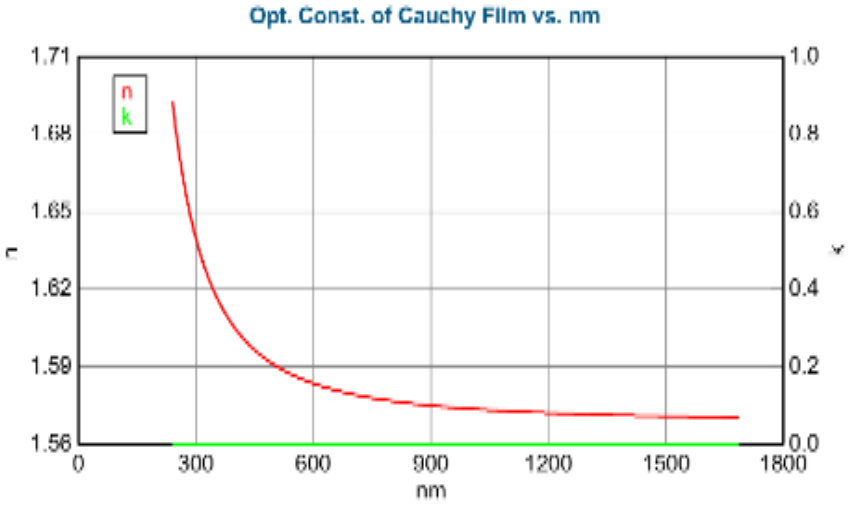

Figure 6.7-1, Refractive index of SU-8 film as function of wavelength measures using ellipsometry.

6.7.2 Silicon oxynitride (SiOxNy) refractive index

The buffering layer of the SPR sensor head was made of SiO_xN_y. Unlike the SU-8 polymer film, the refractive index of SiO_xN_y could be controlled over the wavelength. Therefore, as shown in figure 6.7-2, the SiO_xN_y. cladding layer film that was grown using the PECVD, has a refractive index that can be varied by changing the relative compositions of nitrogen to oxygen in the SiO_xN_y film that measured using Ellipsometry [99, 100]. Appendix B contain all the Filmetrics and Ellipsometry measurements for the capping layers. To characterize the controllability of the SiO_xN_y refractive index, several samples were grown in the PECVD machine using different mass flow rates of silane, ammonia and nitrous oxide. It was found that SiO_xN_y films that contain a larger amount of oxygen atoms lead to a lower refractive index as measured by an ellipsometry, and shown in table 6.7.1.

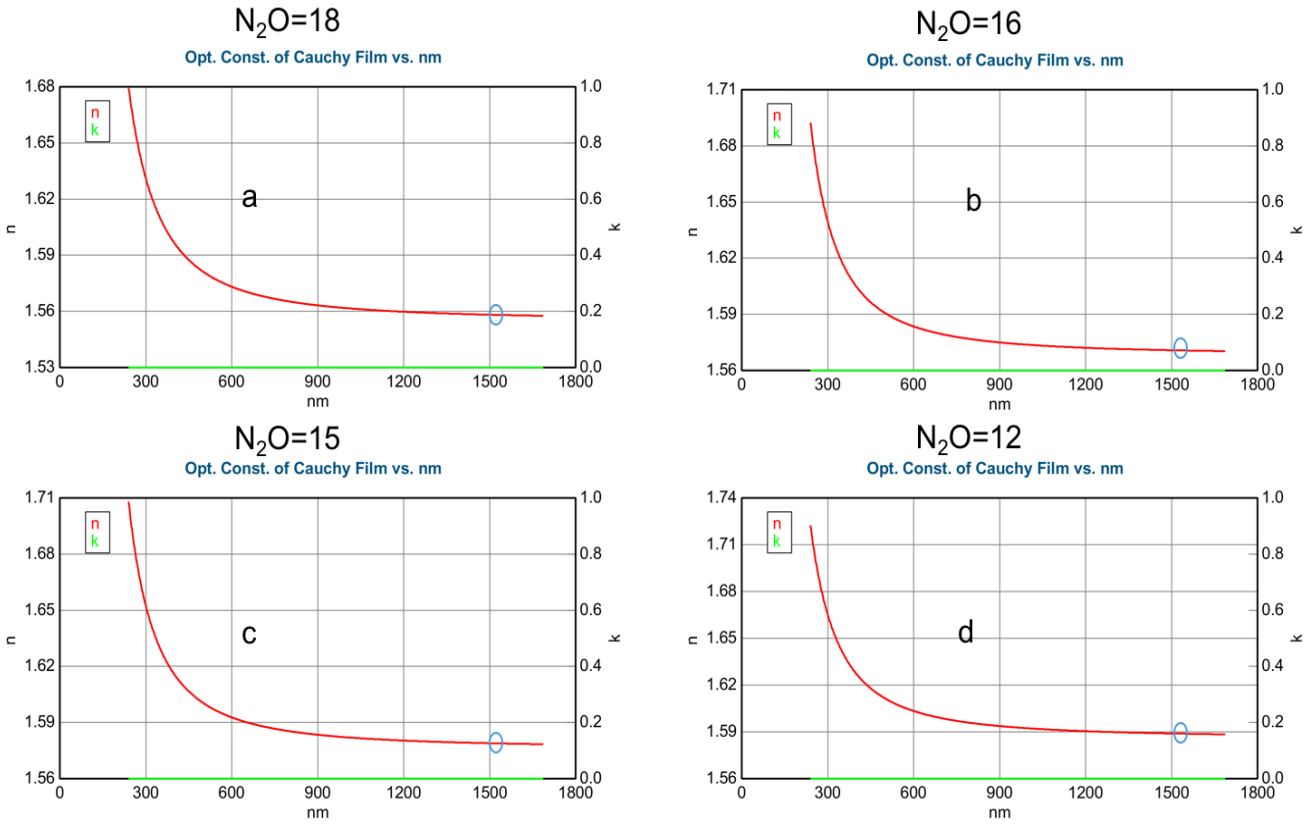

Figure 6.7-2, Refractive index of SiO_xN_y film as function of wavelength measures using ellipsometry a, 1.56 refractive index at 1550nm. b, 1.569 refractive index. c, 1.582 refractive index. d, 1.59 refractive index,

Table 6.7-1, Different recipes for silicon-oxynitride films with varying refractive indices depending on different film composition.

NH_3 sccm	N_2O sccm	SiH_4 sccm	N_2 sccm	Power (W)	DC (V)	Temp (°C)	Refractive Index	Deposition rate nm/min
10	120	200	600	150	8	250	1.46	95
4	40	200	600	100	8	250	1.485	42
4	24	200	600	100	8	250	1.5	37.5
4	21	200	600	100	8	250	1.525	35
4	20	200	600	100	8	250	1.533	35
4	19	200	600	100	8	250	1.55	35
4	18	200	600	100	8	250	1.56	35
4	17	200	600	100	8	250	1.5671	35
4	16	200	600	100	8	250	1.5723	35
4	15	200	600	100	8	250	1.5757	35
4	12	200	600	100	8	250	1.5902	35
4	6	200	600	150	8	250	1.7	30

6.8. Design and simulations

The resonance wavelength of the surface plasmon excited at the gold metal-dielectric interface. The core of the SPR sensor head designed to be inverted rib dielectric waveguide. Thus, to presents a flat top surface to attach the micro-fluidic channel components. The width of the waveguide was design to be 3 µm. The refractive index of the cladding and buffering layers calculated to be 1.568 and 1.526 respectively. Figure 6.8-1shows a cross section of inverted rib type waveguide.

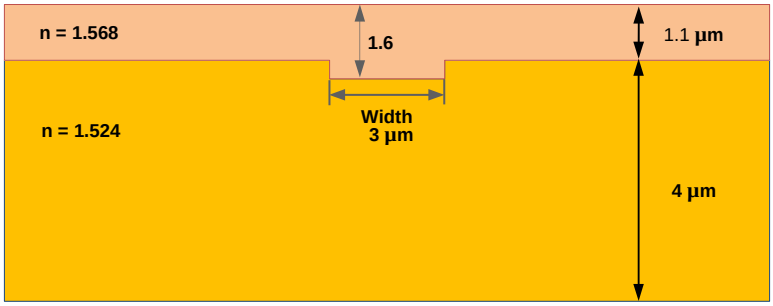

Figure 6.8-1, croos section view for Inverted rib type dielectric waveguide for SPR sensor head.

A schematic drawing of the SPR sensor head shown in Figure 6.8-2. Figure 6.8-3, shows the beam propagation in the SPR sensor head as simulated using a commercial software package (RSoft beam package). In this case, it was observed that the maximum waveguide width and height which can only support the TM fundamental mode are 3.5 µm and 500 nm respectively.

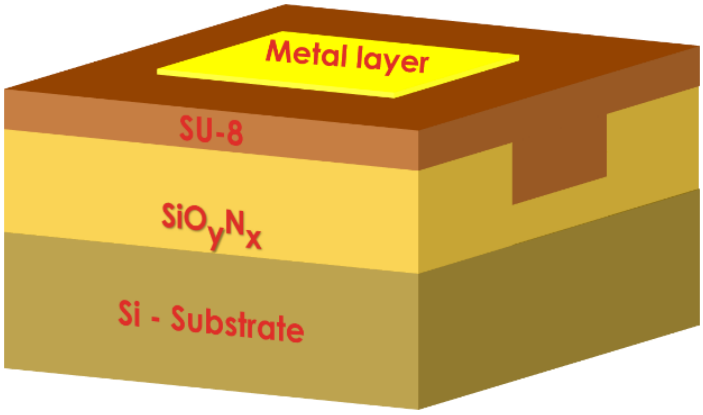

Figure 6.8-2, Schematic of the SPR sensor head

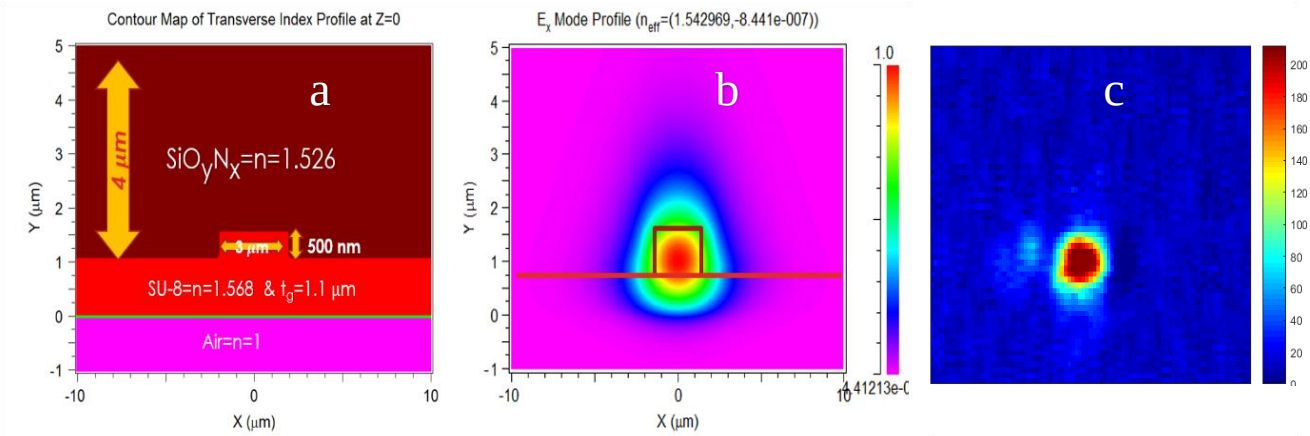

Figure 6.8-3, Simulation of SPR sensor head performed by RSoft . b, fundamental mode for the simulation parameter from a. c, real fundamental mode after fabrication and testing.

If the waveguide width of the SPR sensor increase, the SPR sensor can support multimode. Therefore, we have increased the waveguide width to know the actually width limitation that can produce only the fundamental mode. There were two output modes when we increased the width to 4 µm as shown in figure 6.8.4.

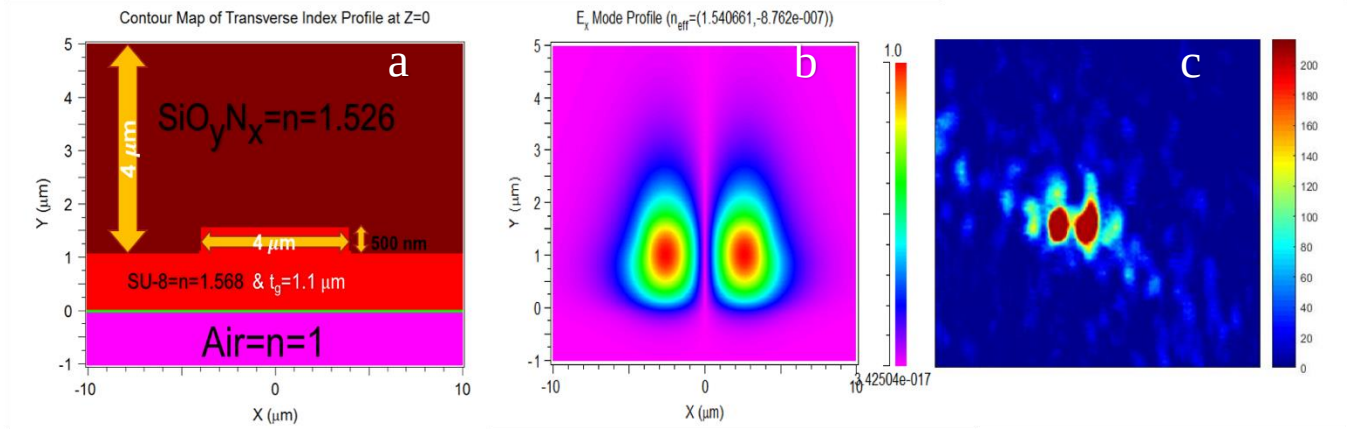

Figure 6.8-4, Simulation of SPR sensor head performed by RSoft. b, fundamental mode for the simulation parameter from a. c, real fundamental mode after fabrication and testing.

6.9. Fabrication

Two SPR sensor head were fabricated, which are chromium-gold and titanium-gold. Both of the sensor had the same buffer and cladding layers but different top surface coating metals. A silicon substrate wafer was cleaved to a size of about 1 cm × 1 cm, and cleaned using buffered oxide etch (dilute HF acid), acetone, isopropanol, and deionized water, respectively. The cleaned sample was coated with a 4 μm thick layer of SiO_xN_y that has a refractive index of 1.523. Then, using a photolithography process a 3 μm wide channel was delineated in NR7-1000P negative photoresist to act as an etching mask. 500 nm of the SiO_xN_y film was etched through the opened channel of the photoresist using reactive ion etching (RIE). The sample was cleaned of the remaining photoresist, using acetone, isopropanol, and deionized water. The whole sample was then coated with a 1 μm thick layer of SU-8 polymer that was cured carefully. Negative photoresist was spun on top of SU-8 and a second photolithography process was used to open a rectangular window directly on top of the inverted SU-8 waveguide. For the chromium-gold SPR sensor. a 20 nm thin layer of chrome followed by a 50 nm thick layer of gold, were vacuum evaporated on top of the sample. While the top surface of titanium-gold SPR sensor, coated with 4 nm of titanium followed by 25nm of gold. The

conventional lift-off process was used to remove the unwanted gold by dissolving the photoresist in acetone. Finally, the silicon substrate was lapped and polished down to a final thickness of 100 μm and the SPR device was cleaved with a total length of 1.8 mm. The microscope photographs of figure 6.9-1 shows the surface of the gold sensing element of the SPR device.

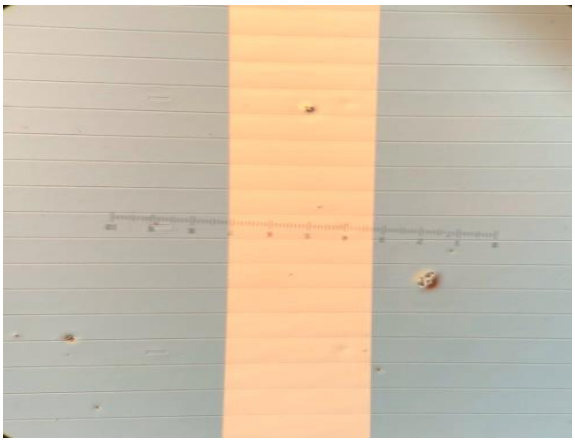

Figure 6.9-1, Top view of SPR sensor head after fabrication and metal.

6.10. Results for chromium -gold SPR sensor using erbium doped fiber amplifier and OSA

The amplified spontaneous emission of an erbium doped fiber amplifier provided the input light for the measurements. A polarizer was used to ensure that only the TM mode was launched into the SPR sensor waveguide by a 40X microscope objective lens. The transmitted light at the output of the device, was focused into an optical fiber that is connected to an Optical Spectrum Analyzer (OSA) to monitor the transmission spectrum as shown in figure 6.10-1. The emission spectrum from the SPR sensor head before placing the sample liquids shown in figure 6.10.2.

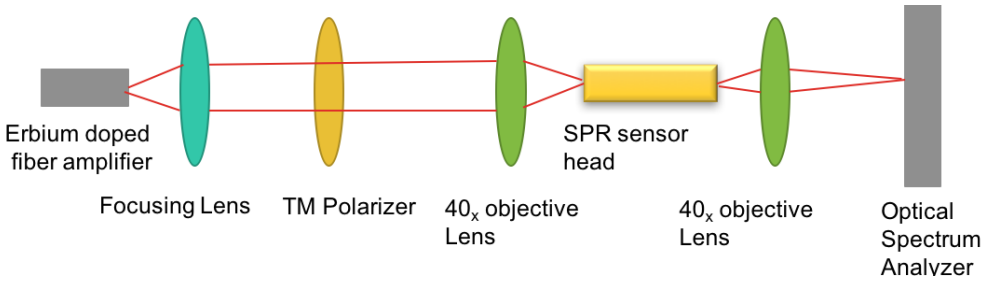

Figure 6.10-1, The experiment setup, the input light originates from an erbium doped fiber amplifier pass through a half-wave plate and a polarizer so that only TM mode could be launched into the waveguide.

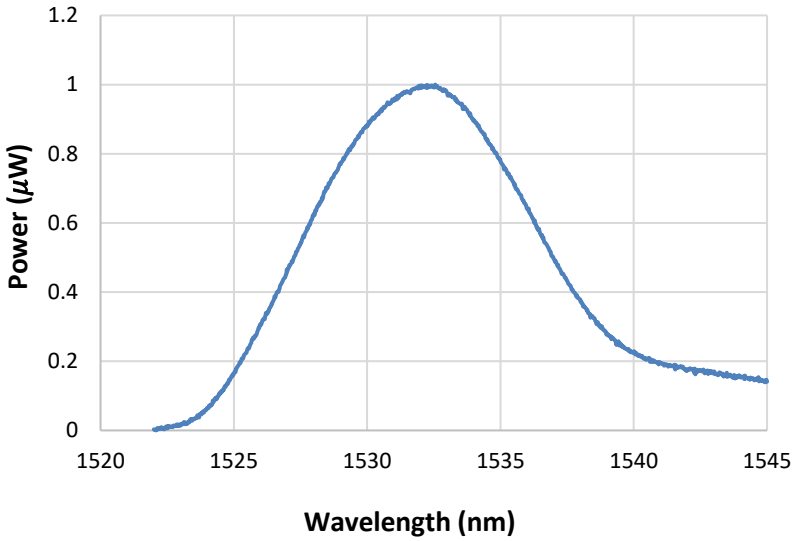

Figure 6.10-2, The emission spectrum from the SPR sensor head before placing the sample liquids.

By launching a broad spectrum of light into the device, it is expected that at the particular wavelength that corresponds to ideal matching condition between the waveguide mode and the surface plasmon mode, a resonant transfer of power from the waveguide should occur. Therefore, the spectrum of the transmitted light is more or less the spectrum of the input light a dip at the SPR wavelength. A set of analyte media with calibrated refractive indices (sample liquids) were applied on top of the SPR sensor head individually, and the transmission spectrum measured by the OSA was used to determine the SPR wavelength. Figure 6.10-3 shows the transmission spectra for analyte media of refractive indices 1.462, 1.496, and 1.502 respectively. As the sample liquid refractive index was lowered, the sharp dip in the transmission spectrum shifted to a shorter wavelength.

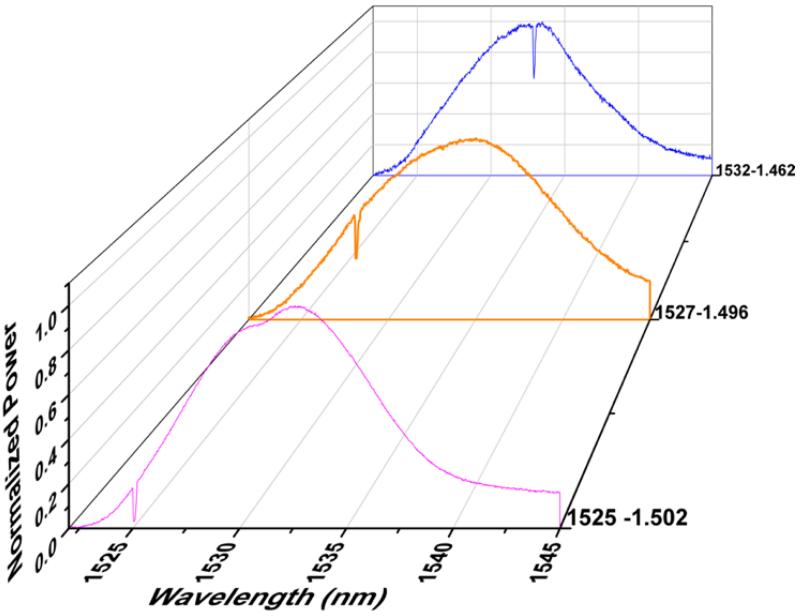

Figure 6.10-3, Emissions spectrum after placing the different sample liquids that results in shifting the transmission dip.

If we use the above device as an intensity modulation type SPR sensor, the refractive index dependence can be used as a measure of refractive index variation. In Figure 6.10-4 we use the refractive index range 1.44 to 1.502 for calculating the sensitivity of the sensor that calculated equation 6.10.1. Therefore, The SPR sensor head sensitivity was calculated to be 232 nm.RIU^{-1}.

$$\mathbf{S}=\Delta\boldsymbol{\gamma}/\Delta\boldsymbol{n} \qquad (3.10.1)$$

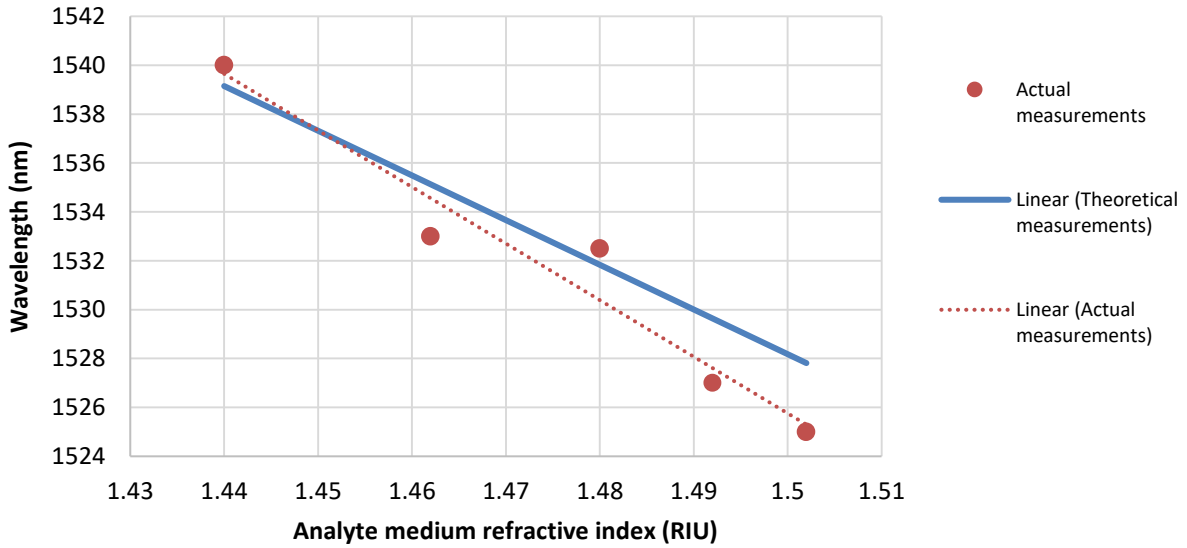

Figure 6.10-4, Different analyte medium refractive indices that change wavelength. Transmission spectrum.

6.10.1 Summary

We have demonstrated a novel optical surface Plasmon resonance (SPR) sensor unit that is based on the launching a surface plasmon wave that is resonant with a dielectric waveguide mode. The sensitivity of the device was measured to be S = 232 nm.RIU^{-1}. We show that the SPR sensor head can be used for monitoring analyte media with a refractive index ranging from 1.44 to 1.502 and the SPR wavelength shifted from 1525 nm to 1539 nm.

6.11. Results for titanium -Gold SPR sensor using semiconductor optical amplifier SOA and OSA

In this experiment, we used the second fabricated SPR sensor that is made of titanium and gold contact to compare the sensitivity and performance result with chromium-gold SPR. Thus, we replaced the erbium-doped fiber amplifier with semiconductor optical amplifier (SOA), which gives us more confinement output light and more broad spectrum. The input light was focused into the SPR sensor waveguide, then it was collected using OSA. Figure 6.11-1 shows the output spectra before placing the sample liquids.

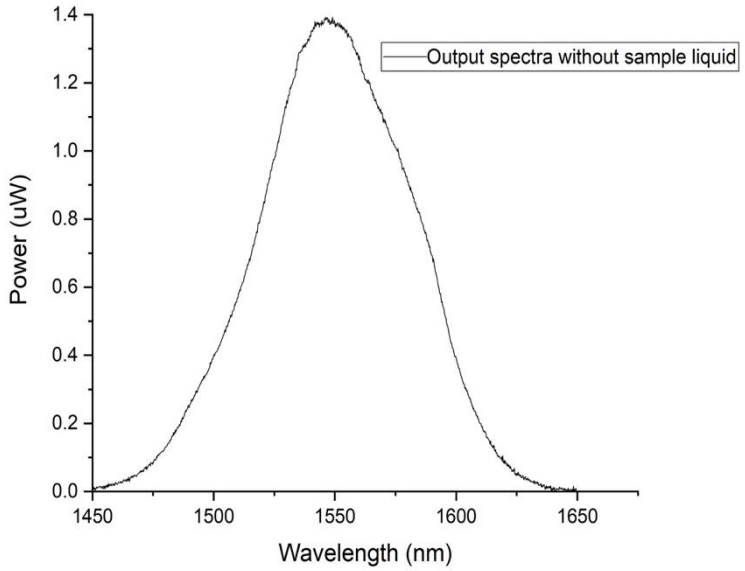

Figure 6.11-1, The emission spectrum from the SPR sensor head before placing the sample liquids originate from SOA.

Set of various sample liquids of the refractive index that will lead to a surface Plasmon resonance were placed on top of the SPR sensor. OSA captured transmission spectra for a range of reference samples liquids in contact with the SPR sensor head. Figure 6.11-2 and 6.11-3, shows the transmission spectra obtained with the sample liquids at the refractive indices of 1.442 and 1.454 respectively. All Sample liquids and results can be found in Appendix C. The shift of the SPR dip position in relation to the refractive index of the sample liquids verifies the functionality of our waveguide SPR sensor.

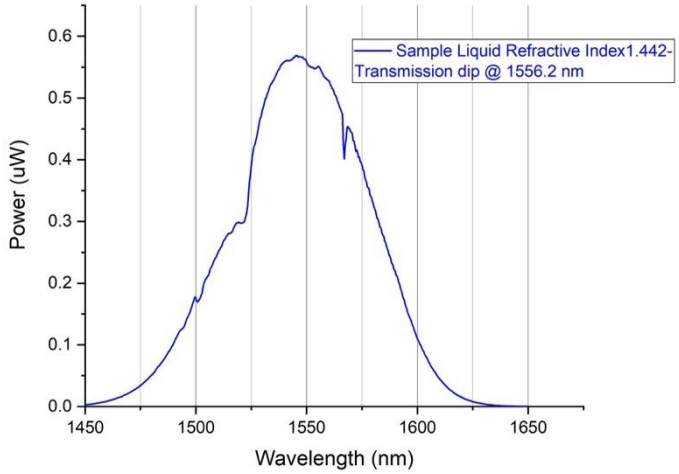

Figure 6.11-2, Emissions spectrum after placing 1.442 sample liquid.

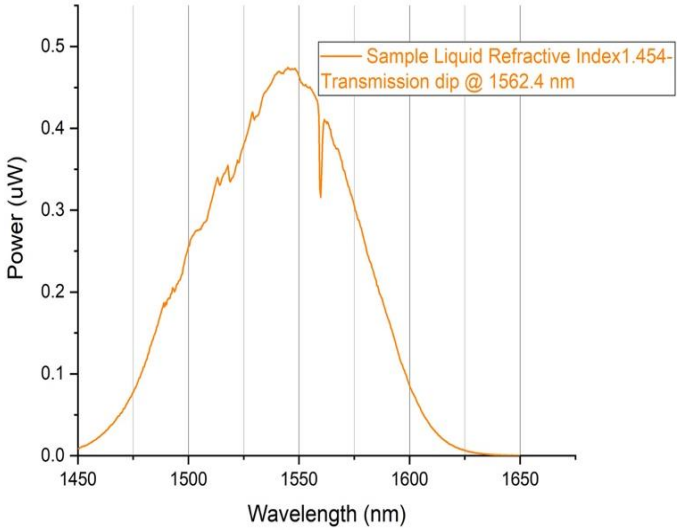

Figure 6.11-3, Emissions spectrum after placing 1.464 sample liquid.

The sensitivity of this SPR sensor was measured using equation 6.10.1 and figure 6.11-4. It was calculated to be S = 338.8nm.RIU^{-1}.

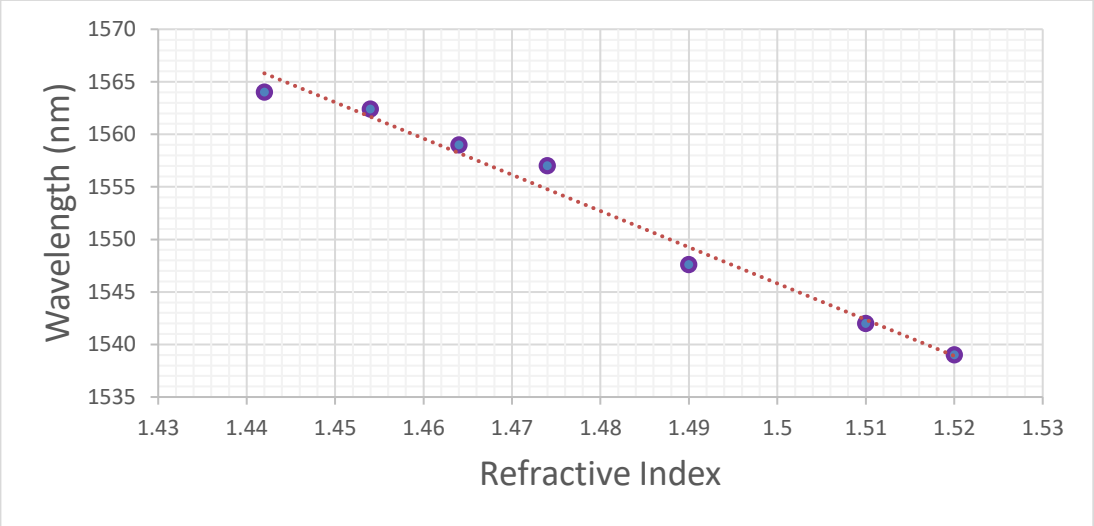

Figure 6.11-4, Different analyte medium refractive indices that change wavelength.

The sensitivity for titanium-gold SPR sensor was increased from 232nm.RIU^{-1}to 338.8 nm.RIU^{-1}. We theorize that this increase was due to the change in the metal contact for the SPR sensor head, from chrome to titanium. Hence, the conductivity of the surface Plasmon was also increased.

6.12. Results for titanium -Gold SPR using commercial Tunable laser

In this experiment. In order to prove that the fabricated tunable laser from chapter 5 will work with the SPR sensor, we replaced the input light source with a commercial tunable laser. The commercial tunable laser (CTL) can tune the laser wavelength up to 100 nm at two mW maximum output power. All the setup components from the previous experiments as shown in figure 6.10-1, were used. We have also replaced the OSA with photodiode to measure the output voltage. This tunable laser can be fully controlled using a software called LabVIEW. All the measurements were performed using 0.1 nm resolution and 1.8 mW output power. Before placing the sample liquids on-top of the SPR sensor, two measurements were performed. We started by measuring the input signal as shown in figure 6.12-1. After which the transmitted light that was focused into the SPR sensor waveguide, and the output signal, were collected and measured as shown in figure 6.12-2.

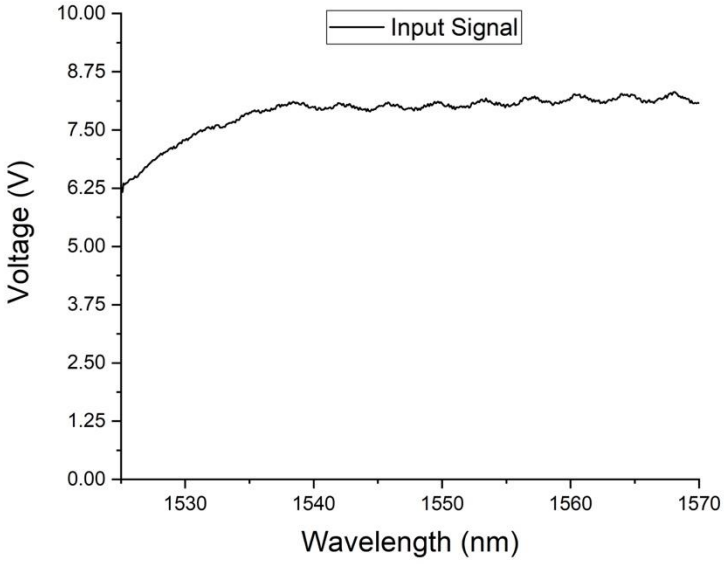

Figure 6.12-1, The emission spectrum from commercail tunable laser

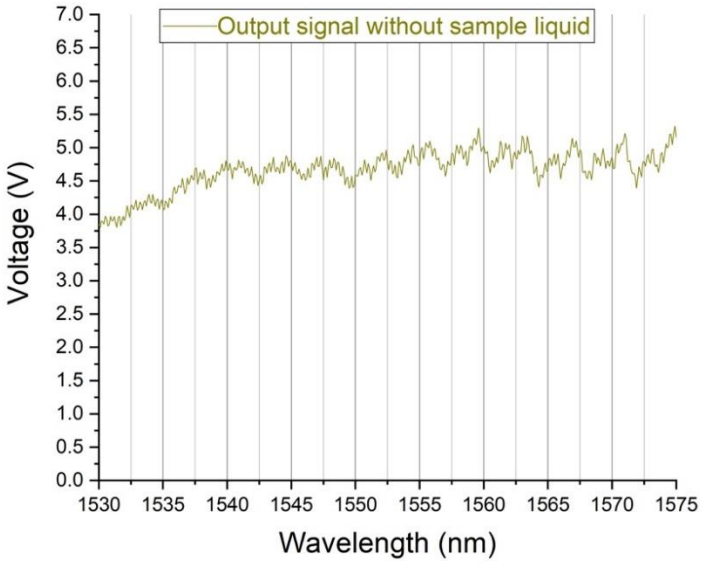

Figure 6.12-2, The emission spectrum from the SPR sensor originate from CT.

A set of reference liquids with refractive index, ranging from 1.442 to the 1.526 were used to find the dip in the transmutation output signal, as shown in figures 6.12-3 and 6.12-4. All the remaining figures could be found in the Appendix D. We observed that as the refractive index of the sample liquid increased, the dip in the transmutation signal shifted to the blue side. Using a set of reference liquids representing the analyte medium, the sharp resonance dip in the transmission spectrum

occurred at 1539 nm, and its position shifted to 1568 nm with an almost 30 nm range. The sensitivity of the sensor devices was determined to be S = 331.1 nm.RIU^{-1} compared to 338.8 nm.RIU^{-1} using the SOA source. The reason for that is the measurements recording error and different sample liquids range.

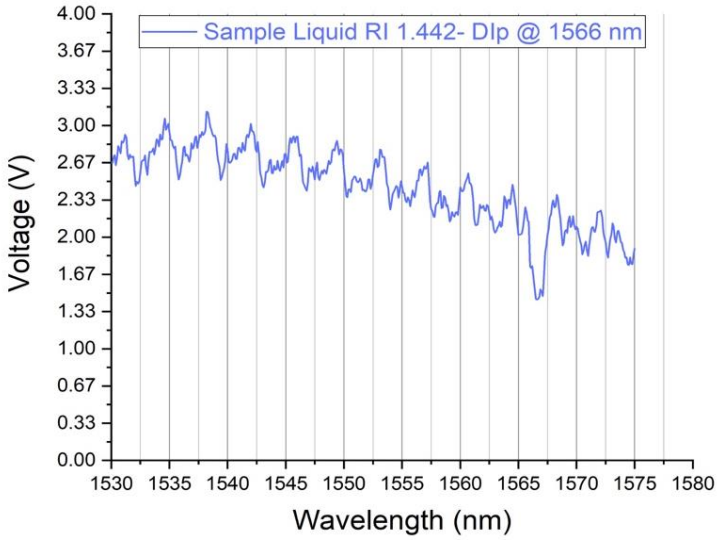

Figure 6.12-3, Output spectrum using 1,442 sample liquids and CTL

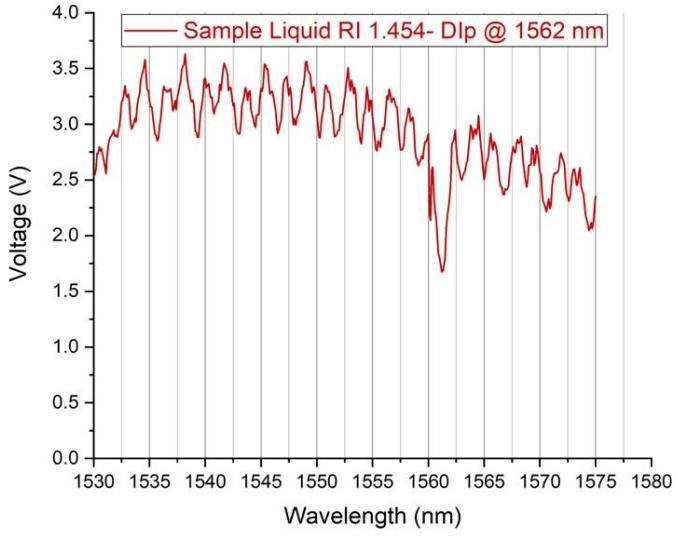

Figure 6.12-4, Output spectrum using 1,442 sample liquids and CTL.

6.13. Outline

Right now we can use the fabricated tunable laser from chapter 5 as input light source for the SPR sensor. The partially integrated device will be explained in more details in chapter 7.

CHAPTER 7: PARTIALLY INTEGRATED TUNABLE LASER DIODE WITH PLASMON RESONANCE OPTICAL SENSOR

7.1.Introduction

Recently, integrated photonics devices have made a tremendous jump in analytical spectroscopy and advanced optical networks applications. Also with the rapid growth and demand for biological sensing instruments, there has been an increased emphasis on more versatile and reliable integrated biomolecule detection systems. The motivation is continually growing especially with the rising health consciousness. A monolithically integrated multiple quantum wells tunable laser diode for launching an optical waveguide mode into asurface plasmonic sensor head is fabricated and investigated experimentally.

Tunable laser diodes allow for very compact integrated devices that are vital for environmental sensing applications requiring spectroscopic measurements such as chemical and biological agents' detection. In this work, we demonstrate an InGaAsP multiple quantum well tunable laser diode that amalgamates two gain sections with different bandgap energies (chapter 5). This is achieved using selective area intermixing of the multiple quantum wells, and impurity-free vacancy induced disordering. When different current combination is injected into each section, that leads to a laser wavelength peak whose position depends on the relative magnitudes of the two injected currents.The laser wavelength can be fine-tuned from 1538 nm to 1578 nm with relatively constant output power. Using the tunable laser diode, we have demonstrated an optical surface plasmon resonance sensor head that is based on an inverted rib dielectric waveguide (chapter 6), in which the resonance wavelength of the surface plasmon excited at the gold metal-dielectric interface depends on the refractive index of the liquid in contact with it. The inverted-rib waveguide of the SPR sensor head is made of a layer of SU-8 polymer with a refractive index of 1.568. While the lower cladding layer

consists of silicon oxynitride (SiOxNy) with a refractive index of 1.526. The top surface is coated with a 4 nm of titanium followed by 25 nm thick layer of gold. The SPR sensor head was designed, to allow monitoring of analyte media with a refractive index, ranging from 1.43 to the 1.52. Using a set of reference liquids representing the analyte medium, the sensitivity of the SPR sensor was measured using the fabricated tunable laser, an optical spectrum analyzer, and a photodiode. It was found that with various calibrated sample liquids in contact with the gold metal, a sharp resonance dip in the transmission spectrum occurred, and its position shifted to shorted wavelength when the refractive index of the sample liquids was increased. Therfore,In this chapter, we partially integrated our InGaAsP multiple quantum well tunable laser from chapter 5 with SPR sensor mentioned in chapter 6. We have been able to prove that the fabricated tunable laser diode does work for probing the SPR optical sensor.

7.2.Experiment Setup

Light from the fabricated tunable laser diode was launched into the SPR sensor head to provide the input light source for the measurements. A 40X microscope objective lens is used to couple the light from the tunable laser into the SPR sensor and another one is used to collect the transmitted light onto a photodetector. The output light from the back facet of the tunable laser diode is used to measure the laser output power and monitor the output spectrum. A half-wave plate was placed in the path of the main laser output beam to ensure that only the TM mode was launched into the SPR sensor. The output transmission from the SPR sensor was split into two by a beamsplitter with one beam being focused onto an IR camera for monitoring the waveguide mode and the other one being coupled into a fiber pigtailed photodiode, to monitor the intensity of the transmission light. The experimental setup is shown in the figure 7.2-1.

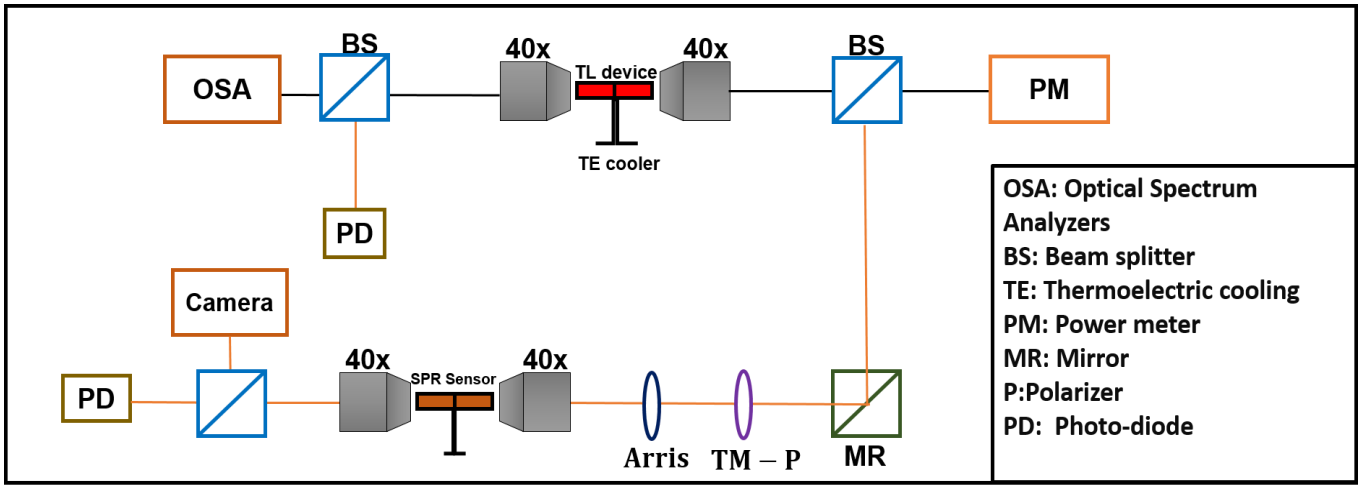

Figure 7.2-1, Experiment setup using the tunable laser as input source.

7.3.Results

The tunable laser was first calibrated and tuned manually before each sample liquid was placed on the surface of the SPR sensor. We started by tuning the operating wavelength of the laser diode from 1545 nm to 1554 nm while noting the electrical currents applied to each electrode and recording the laser spectra as shown in figure 7.3-1 and 7.3-2.

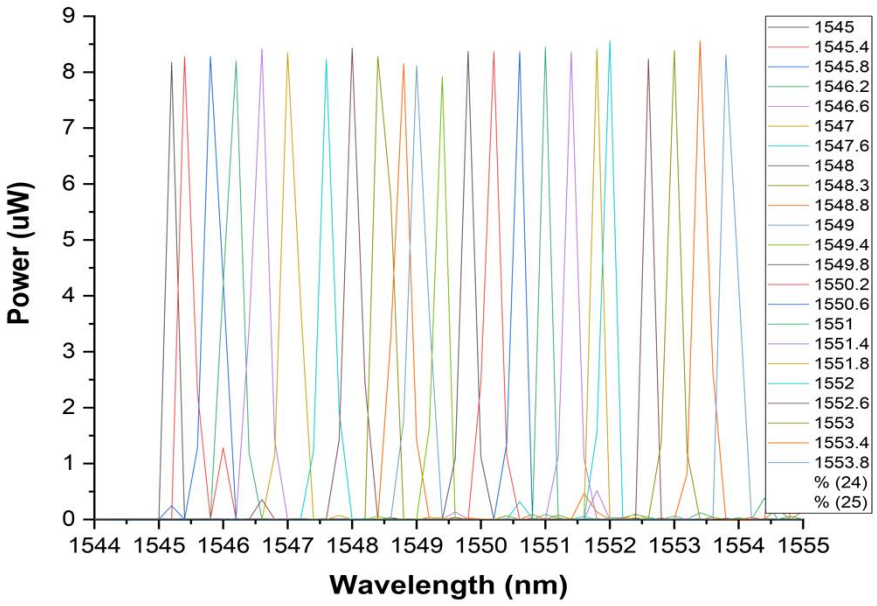

Figure 7.3-1, the laser spectra obtained from the tunable laser diode from 1545 to 1554 nm.

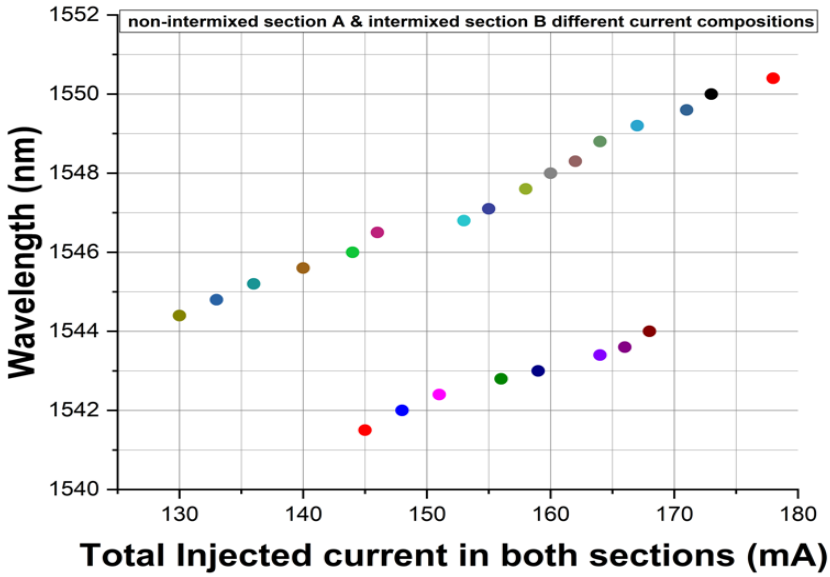

Figure 7.3-2 the tuning wavelengths as function of different current composition for non-intermixed section A and intermixed section B.

The free spectral range (FSR) for our tunable laser was found to be around 0.25 nm. Therefore, for 10 nm tuning range, we have measured 24 readings for each currents and the output power variations between 1.35 mW to 1.45 mW as shown in table 7.3-1.

Table 7.3-1, the tuning range as function of the injected currents I_A and I_B in the sections A & B , output power , and output voltage.

Intermixed (SiN_x) section	Non-intermixed (SiO_xN_y) section	Power before (mW)	Wavelength (nm)	Voltage before sample liquid (V)
Current (mA)				
83	50	1.32	1545	1.95
86	50	1.32	1545.4	1.96
88	52	1.35	1546	1.94
92	52	1.35	1546.5	1.97
94	52	1.37	1546.8	1.98
98	55	1.39	1547.1	1.99
100	55	1.42	1547.6	1.99
103	55	1.42	1548	1.98
105	55	1.42	1548.3	1.98
107	55	1.425	1548.8	1.97
109	55	1.43	1549.2	1.98
114	53	1.35	1549.6	1.96
118	53	1.35	1550	1.95
120	53	1.36	1550.4	1.94
125	53	1.365	1550.8	1.96
128	53	1.4	1551.2	1.97
130	53	1.41	1551.6	1.98
133	62	1.42	1552	1.95
135	62	1.45	1552.4	1.97
137	62	1.48	1552.8	1.99
139	62	1.49	1553.2	2
140	62	1.49	1553.6	2.02
165	45	1.44	1554	1.99

The transmitted output signal from the SPR sensor was measured using a photodiode (voltage unit) detector before placing any sample liquids as shown in figure 7.3-3. The output voltage values were almost constant at 2.2 V as expected. It was observed that the voltage value experienced a sharp drop, once the analyte medium was placed on top of the SPR sensor.

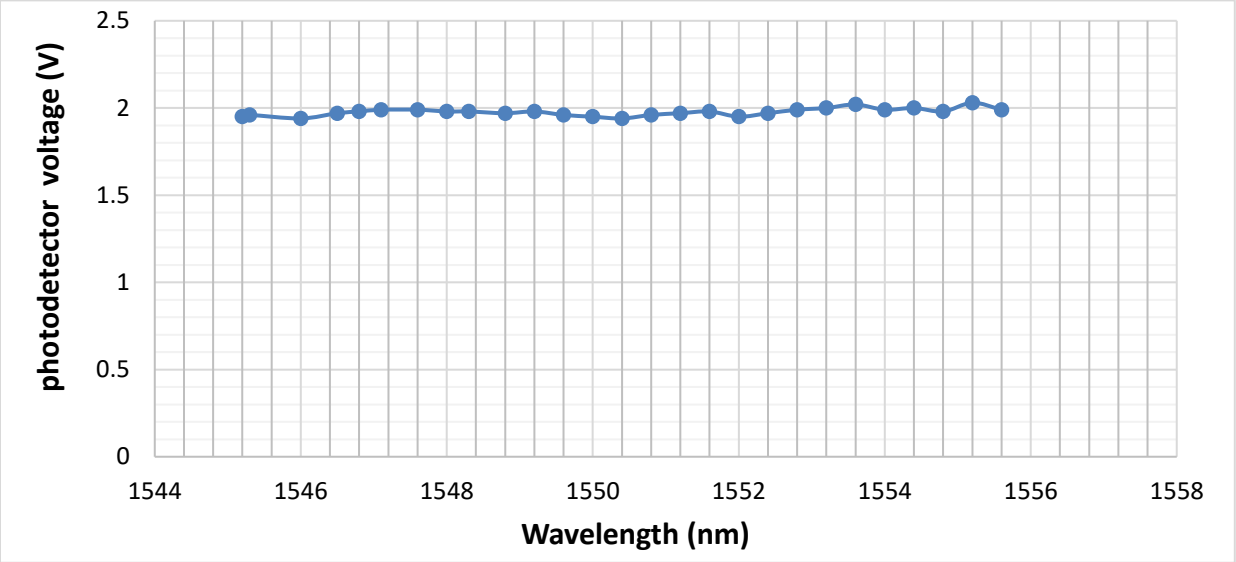

Figure 7.3-3 Photodiode spectrume in voltage as function of wavelength befor placing the sample liquid.

As soon as we placed a sample liquid with a refractive index of 1.494 on top of the SPR sensor, the surface plasmonic waves were launched and the transmitted intensity was reduced. The transmission spectrum was recorded by the scanning the laser while monitoring the photodiode signal and it clearly showed a dip that corresponded to the wavelength of the SPR resonance. The full width at half maximum (FWHM) of the dip was found to be around 1 nm and it occurred at 1548.8 nm as shown in figure 7.3-4.

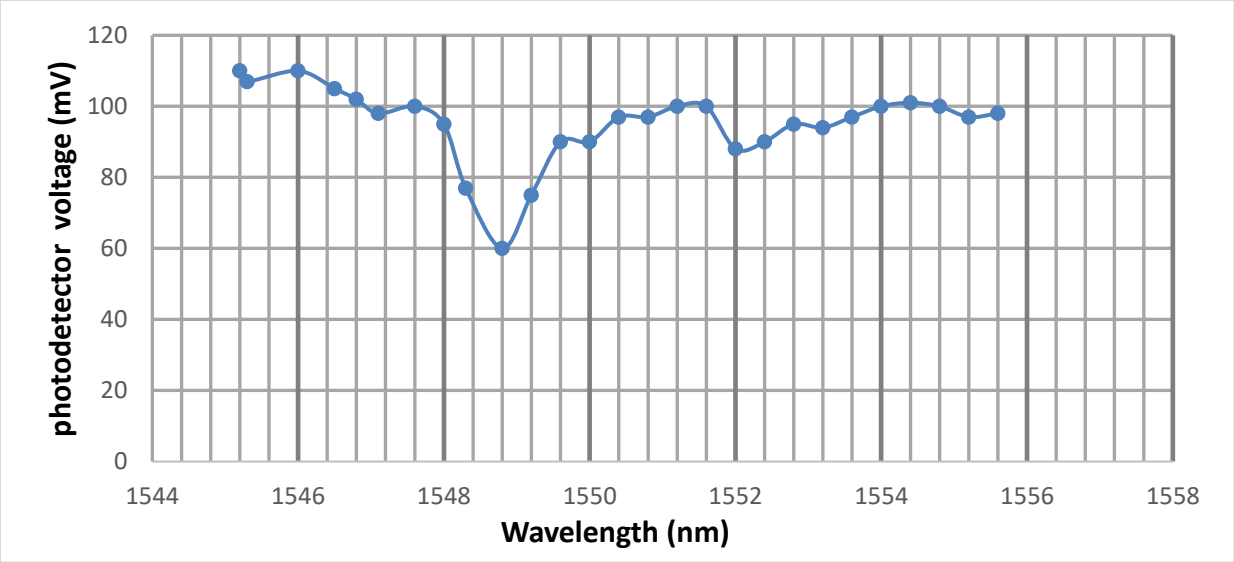

Figure 7.3-4 Photodiode spectrume in voltage as function of wavelength after placing 1.494 refractive index sample liquid.

We have tested the SPR sensor device using five different sample liquids with calibrated refractive indices that varied between 1.512 and 1.438. The sharp resonance dip in the transmission spectrum occurred at 1541 nm and its position shifted to 1568.8 nm with almost 18 nm range as shown in figure 7.3-5. Thus, the sensitivity of the SPR sensor was determined to be S = 334.03 nm.RIU^{-1}. As the sample liquid refractive index was increased, the sharp dip in the transmission spectrum shifted to a shorter wavelength.

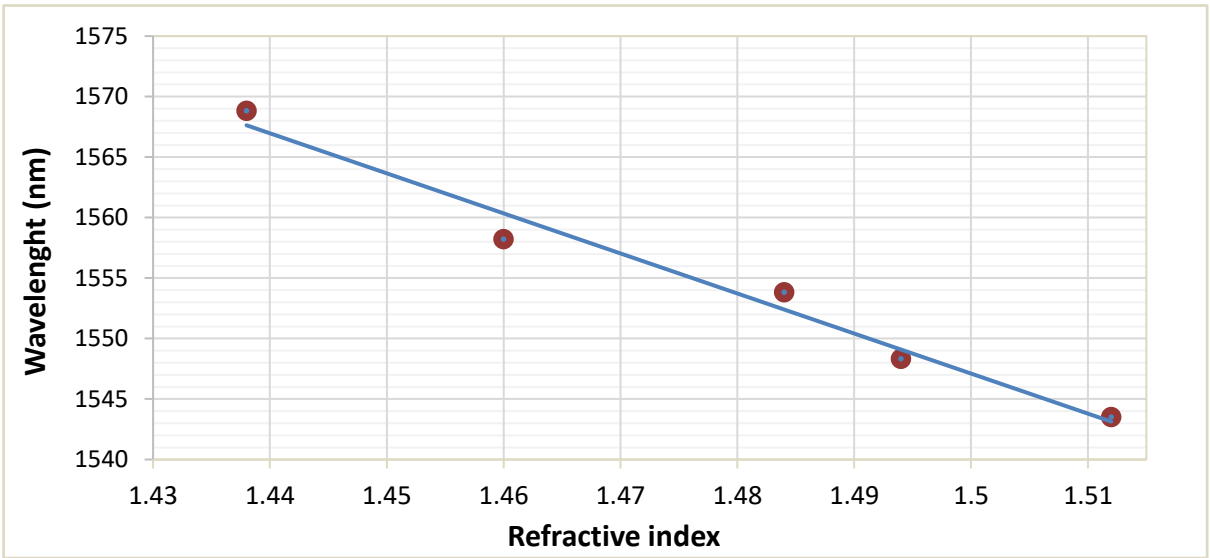

Figure 7.3-5 - Different analyte medium refractive indices that change wavelength.transmission spectrum.

7.4.Summary

We have demonstrated a novel tunable laser diode that has been used to probe an optical surface plasmon resonance (SPR) sensor head. The fabricated device was capable of producing laser emission that was tunable from 1538 nm to 1578 nm. The highest SPR sensitivity of the devices was measured to be S = 334 nm.RIU^{-1}. Both devices were fabricated and partially integrated. We show that the fabricated tunable laser can be potentially be used as probing source for a wide range of spectroscopic applications.

Note:

We have repeated the same measurements and calibration for each set of the sample liquid. The whole data could be found in APPENDIX E. In summary, we were able to tune the tunable laser wavelength from 1541 nm to 1572 nm by changing the injected current compositions for both section A and B as shown in the figures in APPENDIX E.

CHAPTER 8: CONCLUSION

In conclusion, we have demonstrated a novel tunable laser diode that can be used to Probe an optical surface plasmon resonance (SPR) sensor head. This tunable laser diode is amalgamate of two gain sections with different bandgap energies. Using a controlled technique for selective-area intermixing of InGaAsP MQWs, a two-section laser diode whose wavelength of operation can be tuned by varying the injected current applied to the two sections has been demonstrated. The bandgap energy of the MQW section capped by a SiN_x layer, which remains unchanged at a corresponding wavelength of 1560 nm. Meanwhile, the bandgap wavelength of the section capped by SiO_xN_y layer is blue shifted to 1530 nm. The fabricated device was capable of producing laser emission that was tunable from 1538 to 1578 nm depending on the currents injected into the two sections. The continuous wavelength tuning could be achieved with fixed output power. Furthermore, The L-I measurements for individual devices fabricated in either section show only a small degradation from the characteristics of a reference device fabricated in the as-grown MQW sample. The manipulation of bandgap energies on a single chip can enable different functionality of this tunable laser.

We launched the fabricated InGaAsP MQW tunable laser into an optical surface Plasmon resonance (SPR) sensor head, based on an inverted rib dielectric waveguide. Where the resonance wavelength of the surface plasmon excited at the gold metal-dielectric interface. The SPR sensor head was designed to allow monitoring of analyte media with a refractive index ranging from 1.43 to the 1.52. Using a set of reference liquids representing the analyte medium, the sensitivity of the SPR sensor was measured using our fabricated tunable laser as light source and an optical spectrum analyzer. It was found that with a liquid of 1.43 refractive index in contact with the gold metal, a sharp resonance dip in the transmission spectrum occurred at 1568 nm and its position shifted to 1542 nm when a

liquid of 1.514 was used. From these measurements, the sensitivity of the sensor devices was determined to be S = 334 nm.RIU^{-1}. We demonstrate that this device can potentially be integrated entirely with a wavelength tunable light source, a photodetection unit as well as a liquid delivery system via microfluidic channels making it an extremely compact unit.

APPENDIX A TUNABLE LASER –CURRENT INJECTED DATA

Section B (SiO_xN_y)	Section A (SiN_x)	Total injected Current (mA)	Power (μW)	Average Wavelength (nm)
Current (mA)				
12	55	67	75.6	1550
12	65	77	306	1553
12	75	87	660	1553.5
12	85	97	840	1557
12	95	107	870	1560
12	105	117	1008	1561.5
12	115	127	948	1563
12	125	137	660	1566
25	42	67	192	1546
25	50	75	774	1548
25	65	90	1020	1550.2
25	75	100	1052	1553.5
25	85	110	1085.2	1556.3
25	95	120	1092	1557.3
25	105	130	1093	1560
25	135	160	1093.8	1565.7
35	35	70	192	1545
35	45	80	900	1548
35	55	90	1032	1551
35	65	100	1062.6	1553
35	75	110	1074	1558
35	85	120	1080	1559
35	95	130	1086	1560
35	105	140	1086	1561
35	115	150	1098	1562
45	30	75	180	1544
45	45	90	1020	1545
45	55	100	1056	1547.7
45	65	110	1076.4	1549.3
45	75	120	1087.8	1555
45	85	130	1093.2	1556.5
45	95	140	1098	1557
45	105	150	1100.4	1558
55	25	80	312	1542
55	35	90	984	1543

55	45	100	1044	1544.7
55	55	110	1071.6	1546.7
55	65	120	1084.8	1549.4
55	75	130	1095.6	1552.5
55	85	140	1100.4	1553.4
55	95	150	1104.6	1555.3
55	105	160	1113	1558
65	30	95	720	1540
65	35	100	997.2	1542
65	45	110	1060.2	1545
65	55	120	1086.2	1547
65	65	130	1092	1549
65	75	140	1100.4	1550.6
65	85	150	1105.8	1552.8
65	95	160	1106	1555
65	105	170	1050	1558
75	25	100	312	1539
75	35	110	984	1542
75	45	120	1044	1544
75	55	130	1071.6	1546
75	65	140	1085.8	1548
75	75	150	1095.6	1549
75	85	160	1100.4	1557.4
75	95	170	1104.6	1562
75	105	180	1113	1566.8
85	20	105	198	1537
85	35	120	1050	1545
85	45	130	1098	1549
85	55	140	1104	1553
85	65	150	1116	1556
85	75	160	1156	1560
85	85	170	1180	1565.8
85	95	180	1240	1568.9
85	105	190	1300	1573

- **Second Tunable Laser –current injected data**

Section A (SiN_x)	Section B (SiO_xN_y)	Power (µW)	Average Wavelength (nm)
Current (mA)			
45	45	52.8	1543
45	55	376.2	1546.3
45	65	660	1548.9
45	75	825	1551.5
45	85	970.2	1551.9
45	95	990	1555.4
45	105	1062.6	1556.7
45	115	838.2	1559.3
45	125	1108.8	15560
45	135	541.2	15561
45	145	99	1563
45	155	52.8	1565
55	45	283.8	1545.2
55	55	561	1546.8
55	65	844.8	1549
55	75	1036.2	1551.2
55	85	1095.6	1552.9
55	95	1122	1554.9
55	105	1122	1556.2
55	115	1075.8	1559
55	125	1128.6	1559.4
55	135	805.2	15560
55	145	224.4	1561.8
55	155	52.8	1564
65	35	198	1541
65	45	402.6	1543.7
65	55	864.6	1546
65	65	1089	1549
65	75	1128.6	1550
65	85	1148.4	1552.5
65	95	1161.6	1554.3
65	105	1161.6	1555.6
65	125	1188	1558
65	135	#VALUE!	

75	30	59.4	1540
75	45	646.8	1545
75	55	1016.4	1546
75	65	1115.4	1549
75	75	1155	1550.8
75	85	1168.2	1553
75	95	1174.8	1554.4
75	105	1174.8	1555.6
85	30	59.4	1539.5
85	45	772.2	1543
85	55	1095.6	1546
85	65	1155	1548
85	75	1174.8	1550
85	85	1181.4	1552.5
85	95	1188	1555
85	105	1188	1556
95	30	52.8	1539
95	45	818.4	1546
95	55	1115.4	1548
95	65	1161.6	1550
95	75	1181.4	1551
95	85	1188	1553
95	95	1194.6	1554
95	105	1201.2	1555
105	30	56.1	1538
105	45	924	1544
105	55	1128.6	1546
105	65	1174.8	1548
105	75	1188	1550.9
105	85	1194.6	1553.6
105	95	1201.2	155.1
105	105	1201.2	1556.9

- **Third Tunable Laser –current injected data**

Section A (SiN_x)	Section B (SiO_xN_y)	Power (mW)	Average Wavelength (nm)
Current (mA)			
65	40	0.4	1545
75	40	0.55	1548
85	40	0.67	1550
95	40	0.71	1552.5
105	40	0.8	1555
115	40	0.93	1557.75
125	40	1	1560
135	40	1.12	1562
145	40	1.24	1564.5
155	40	1.33	1566
165	40	1.44	1567.75
175	40	1.53	1569
185	40	1.64	1571
65	60	0.63	1548.5
75	60	0.74	1550.25
85	60	0.81	1552
95	60	0.91	1556
105	60	1.03	1558
115	60	1.14	1561
125	60	1.26	1562.3
135	60	1.35	1564.5
145	60	1.44	1567
155	60	1.54	1569.25
165	60	1.63	1571
175	60	1.71	1573
185	60	1.79	1574.5
65	80	0.77	1549
75	80	0.86	1552.35
85	80	0.96	1555
95	80	1.05	1558
105	80	1.15	1560
115	80	1.23	1562
125	80	1.32	1563
135	80	1.43	1566
145	80	1.5	1568

155	80	1.61	1572
165	80	1.72	1573.5
175	80	1.8	1575
185	80	1.88	1576.57
65	100	0.79	1551
75	100	0.89	1556
85	100	0.98	1559
95	100	1.09	1561
105	100	1.18	1563.5
115	100	1.27	1566
125	100	1.37	1568.5
135	100	1.47	1570
145	100	1.56	1573
155	100	1.66	1574.3
165	100	1.76	1575.5
175	100	1.84	1577.25
185	100	1.88	1579
65	120	0.86	1554
75	120	0.97	1557
85	120	1.07	1559
95	120	1.17	1560
105	120	1.28	1564
115	120	1.37	1567
125	120	1.46	1571
135	120	1.55	1574
145	120	1.66	1576
155	120	1.78	1578
165	120	1.89	1580
65	140	1	1560
75	140	1.11	1562
85	140	1.23	1566.5
95	140	1.32	1569.25
105	140	1.42	1572
115	140	1.53	1573
125	140	1.61	1577
135	140	1.72	1578.25
145	140	1.8	1579
155	140	1.9	1581
175	140	0	0

- **Blue Shifted Wavelength examples**

Section A (SiN_x) Current (mA)	Section B ($SiOxN_y$) Current (mA)	Blue Shifted Wavelength (nm)
70	35	1559
70	45	1556
70	55	1553
70	65	1550
70	75	1548
70	85	1545
70	95	1542
70	105	1540
35	65	1560
45	65	1562
55	65	1564
65	65	1566
75	65	1568
85	65	1573
95	65	1576
105	65	1578
115	65	1580

APPENDIX B SIO_XN_Y FILMS REFRACTIVE INDEX MEASUREMENTS USING FILMETRIC

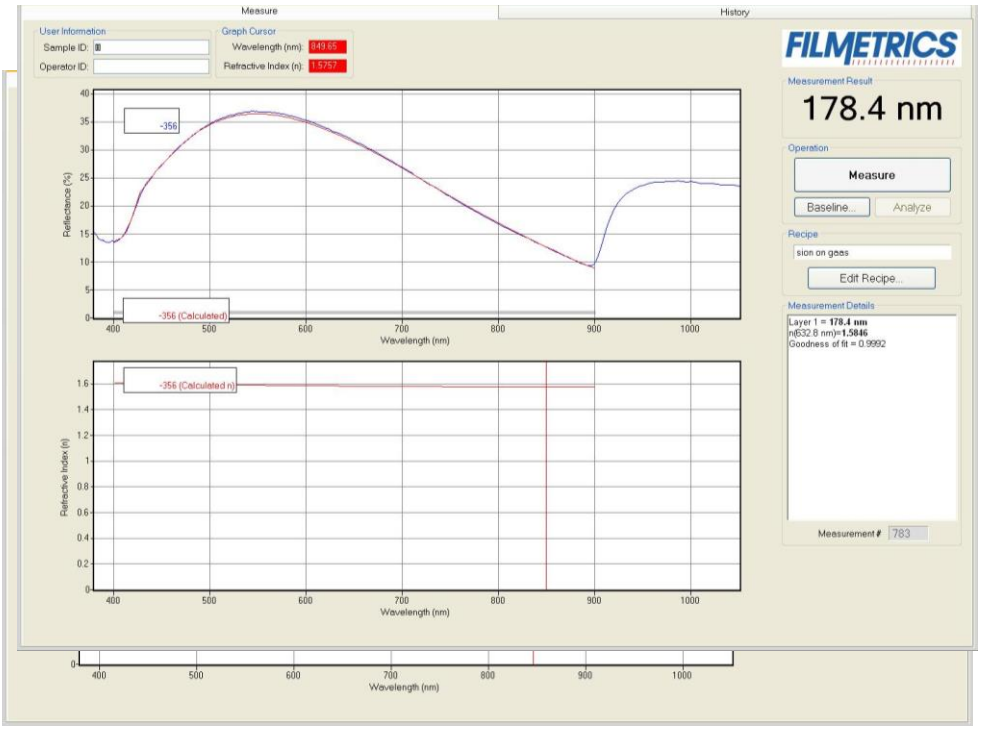
Measure
History
User Information
Sample ID:
Operator ID:
Graph Cursor
Wavelength (nm): 849.65
Refractive Index (n): 1.5767
FILMETRICS
Measurement Result
178.4 nm
Operation
Measure
Baseline...
Analyze
Recipe
sion on gaas
Edit Recipe...
Measurement Details
Layer 1 = 178.4 nm
n(632.8 nm)=1.5846
Goodness of fit = 0.9992
Measurement # 783
-356
-356 (Calculated)
-356 (Calculated n)
Reflectance (%)
Refractive Index (n)
Wavelength (nm)

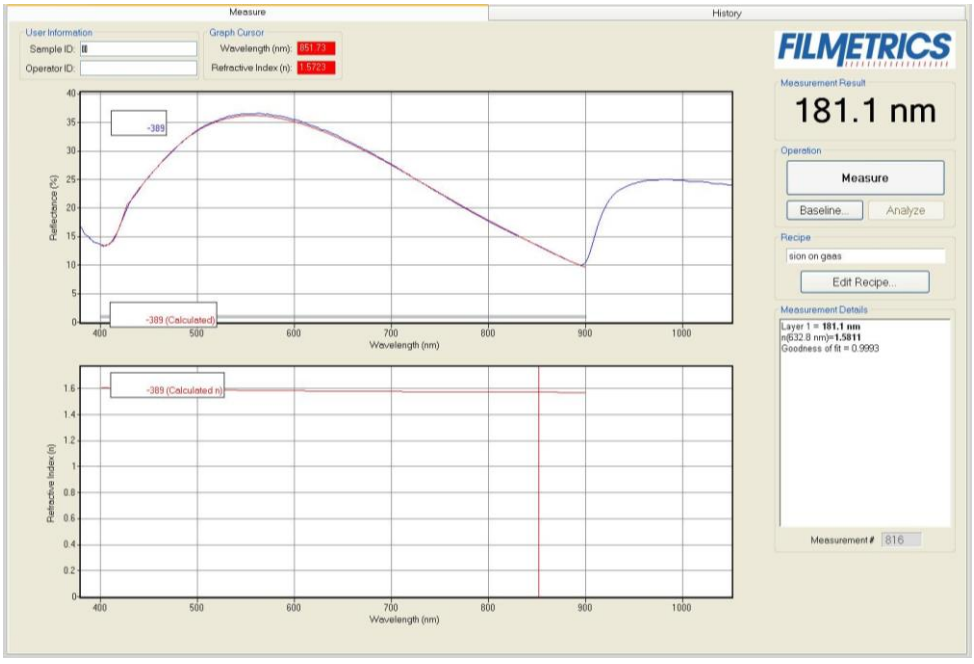
Measure
History
User Information
Sample ID:
Operator ID:
Graph Cursor
Wavelength (nm): 851.73
Refractive Index (n): 1.5723
FILMETRICS
Measurement Result
181.1 nm
Operation
Measure
Baseline...
Analyze
Recipe
sion on gaas
Edit Recipe...
Measurement Details
Layer 1 = 181.1 nm
n(632.8 nm)=1.5811
Goodness of fit = 0.9993
Measurement # 816
-389
-389 (Calculated)
-389 (Calculated n)
Reflectance (%)
Refractive Index (n)
Wavelength (nm)

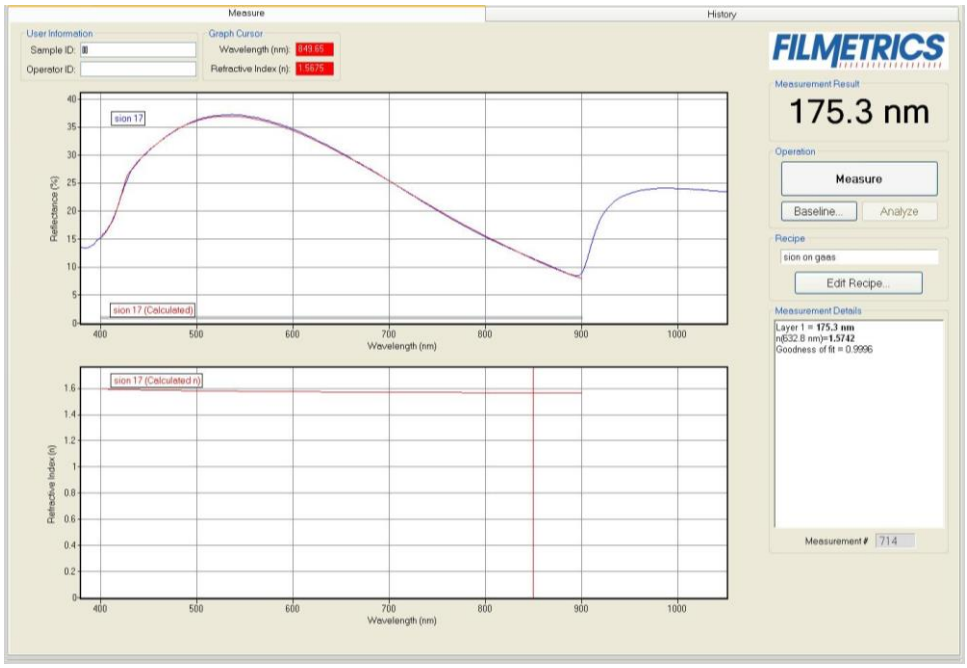
Measure
History
User Information
Sample ID:
Operator ID:
Graph Cursor
Wavelength (nm): 849.65
Retractive Index (n): 1.5675
FILMETRICS
Measurement Result
175.3 nm
Operation
Measure
Baseline...
Analyze
Recipe
sion on gaas
Edit Recipe...
Measurement Details
Layer 1 = 175.3 nm
n(632.8 nm)=1.5742
Goodness of fit = 0.9996
Measurement # 714
sion 17
sion 17 (Calculated)
Reflectance (%)
Wavelength (nm)
sion 17 (Calculated n)
Refractive Index (n)
Wavelength (nm)

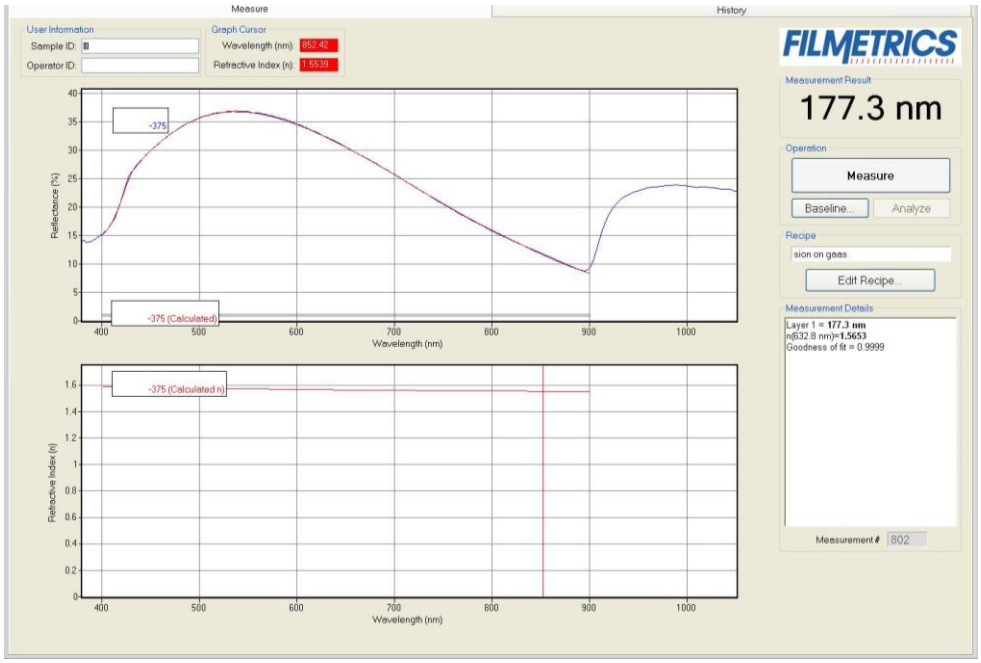
Measure
History
User Information
Sample ID:
Operator ID:
Graph Cursor
Wavelength (nm): 852.42
Refractive Index (n): 1.5539
FILMETRICS
Measurement Result
177.3 nm
Operation
Measure
Baseline...
Analyze
Recipe
sion on gaas
Edit Recipe...
Measurement Details
Layer 1 = 177.3 nm
n@632.8 nm)=1.5653
Goodness of fit = 0.9999
Measurement # 802
-375
-375 (Calculated)
Reflectance (%)
Wavelength (nm)
-375 (Calculated n)
Refractive Index (n)
Wavelength (nm)

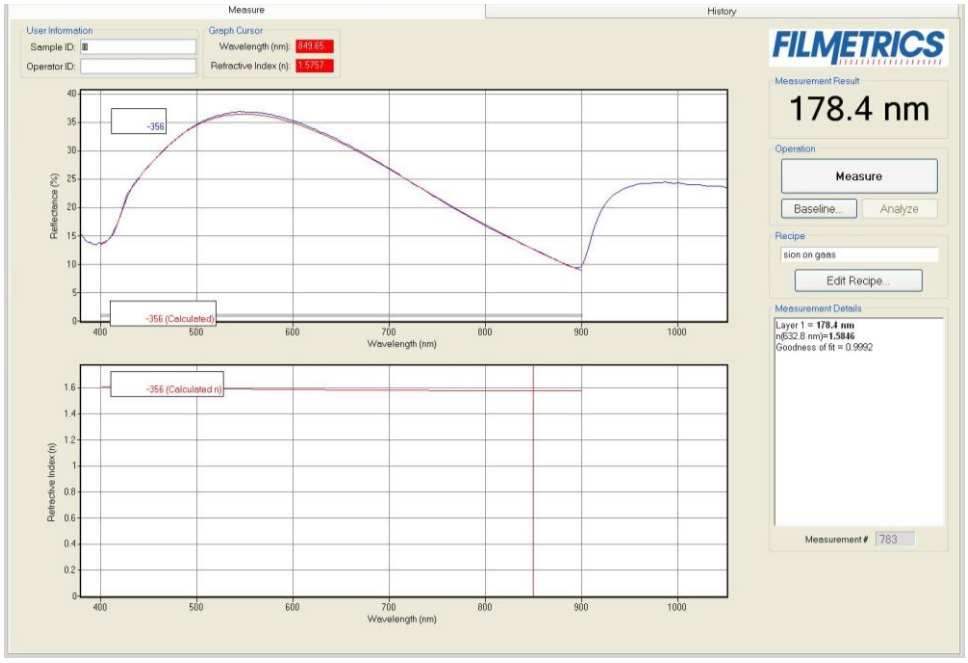
Measure
History
User Information
Sample ID:
Operator ID:
Graph Cursor
Wavelength (nm): 849.65
Refractive Index (n): 1.5767
FILMETRICS
Measurement Result
178.4 nm
Operation
Measure
Baseline...
Analyze
Recipe
sion on gaas
Edit Recipe...
Measurement Details
Layer 1 = 178.4 nm
n@632.8 nm)=1.5846
Goodness of fit = 0.9992
Measurement # 783
-356
-356 (Calculated)
Reflectance (%)
Wavelength (nm)
-356 (Calculated n)
Refractive Index (n)
Wavelength (nm)

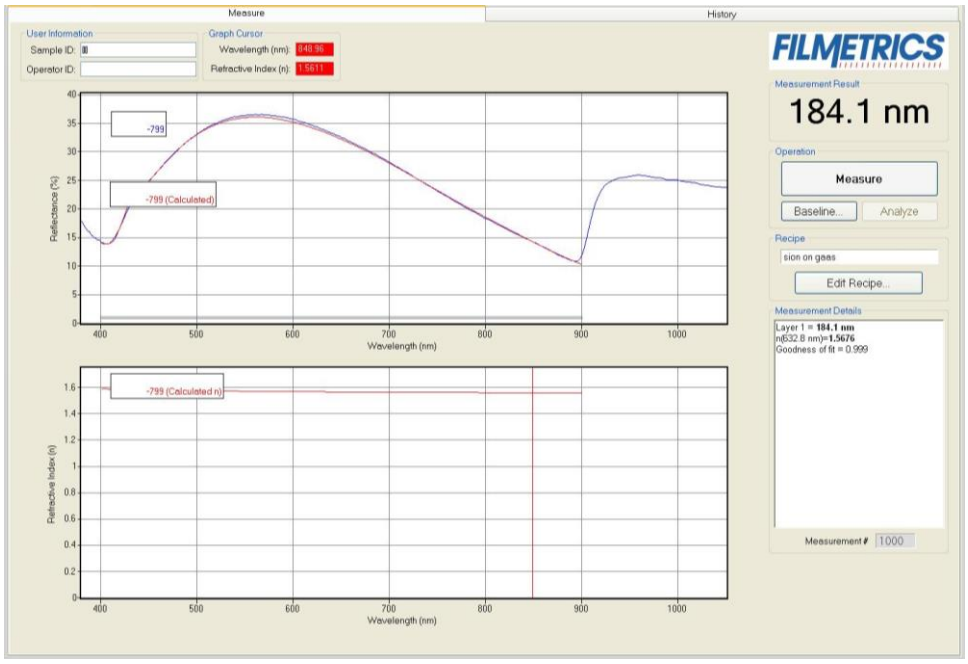
Measure
History
User Information
Sample ID:
Operator ID:
Graph Cursor
Wavelength (nm): 848.96
Refractive Index (n): 1.5611
FILMETRICS
Measurement Result
184.1 nm
Operation
Measure
Baseline...
Analyze
Recipe
sion on gaas
Edit Recipe...
Measurement Details
Layer 1 = 184.1 nm
n@632.8 nm)=1.5676
Goodness of fit = 0.999
Measurement # 1000
-799
-799 (Calculated)
Reflectance (%)
Wavelength (nm)
-799 (Calculated n)
Refractive Index (n)

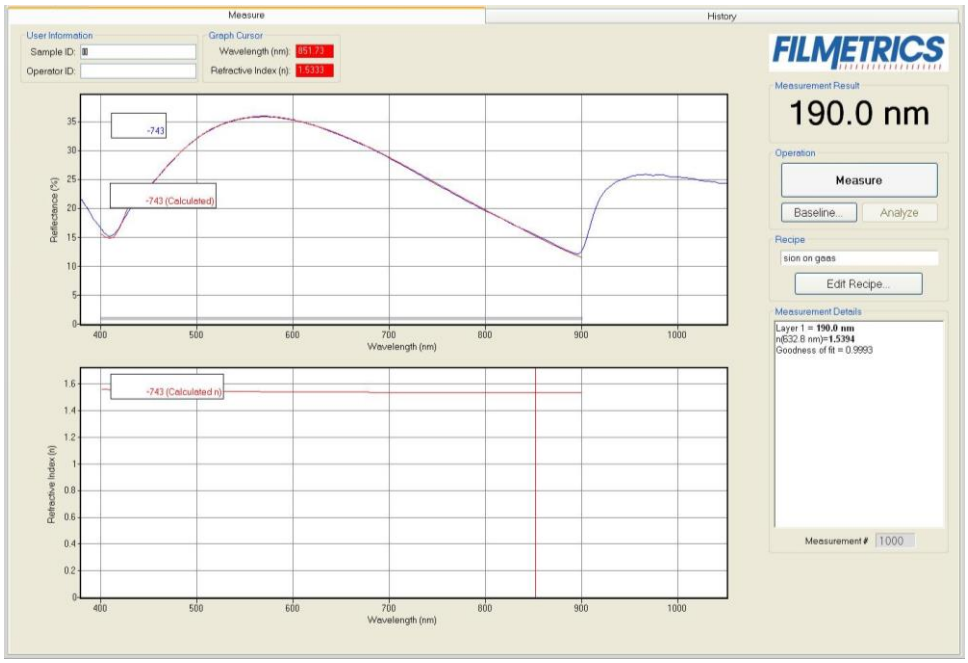
Measure
History
User Information
Sample ID:
Operator ID:
Graph Cursor
Wavelength (nm): 851.73
Refractive Index (n): 1.5333
FILMETRICS
Measurement Result
190.0 nm
Operation
Measure
Baseline...
Analyze
Recipe
sion on gaas
Edit Recipe...
Measurement Details
Layer 1 = 190.0 nm
n@632.8 nm)=1.5394
Goodness of fit = 0.9993
Measurement # 1000
-743
-743 (Calculated)
Reflectance (%)
Wavelength (nm)
-743 (Calculated n)
Refractive Index (n)

APPENDIX C ALL THE SAMPLE LIQUIDS FIGURES FOR SECTION 6.11

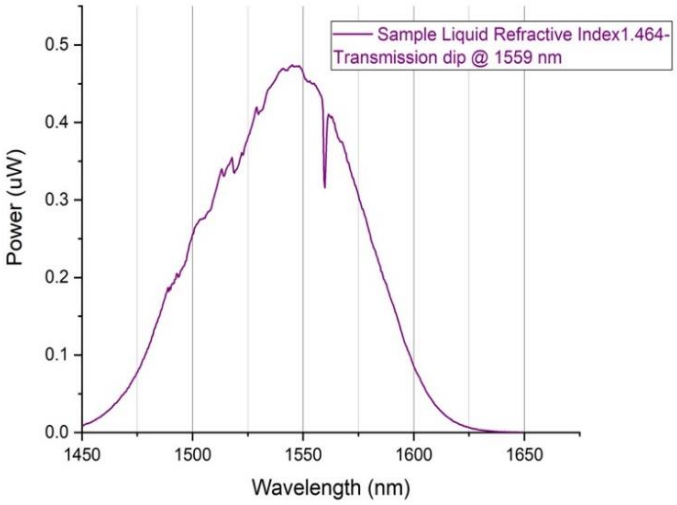
Sample Liquid Refractive Index1.464-
Transmission dip @ 1559 nm
Power (uW)
0.0
0.1
0.2
0.3
0.4
0.5
1450
1500
1550
1600
1650
Wavelength (nm)

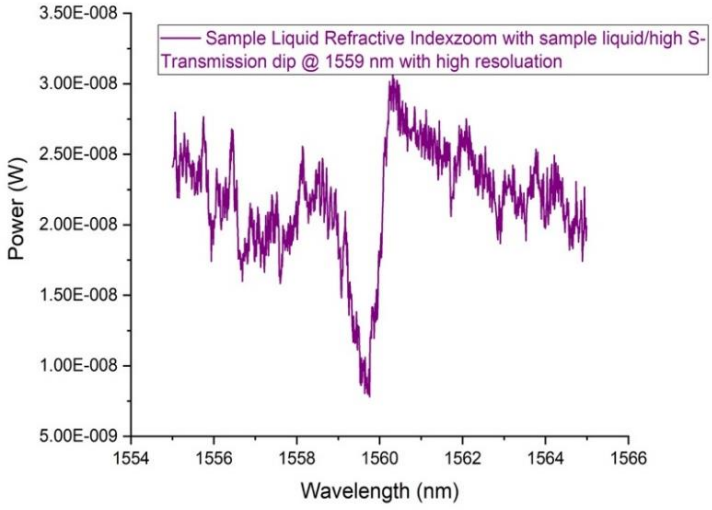
Sample Liquid Refractive Indexzoom with sample liquid/high S-
Transmission dip @ 1559 nm with high resoluation
Power (W)
3.50E-008
3.00E-008
2.50E-008
2.00E-008
1.50E-008
1.00E-008
5.00E-009
1554
1556
1558
1560
1562
1564
1566
Wavelength (nm)

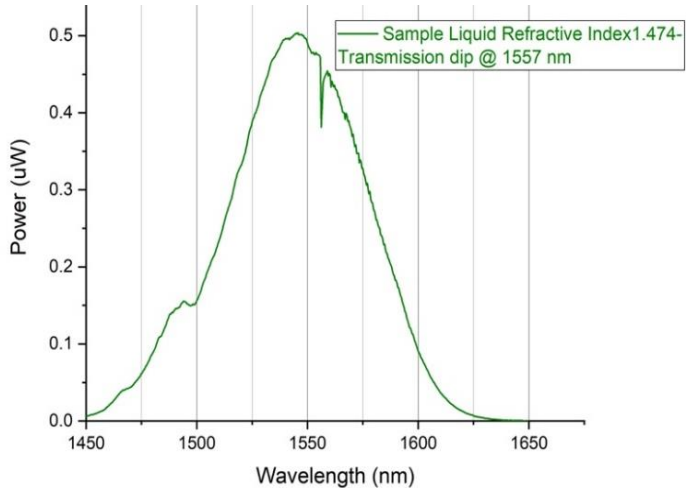
Sample Liquid Refractive Index1.474-
Transmission dip @ 1557 nm
Power (uW)
Wavelength (nm)
0.0
0.1
0.2
0.3
0.4
0.5
1450
1500
1550
1600
1650

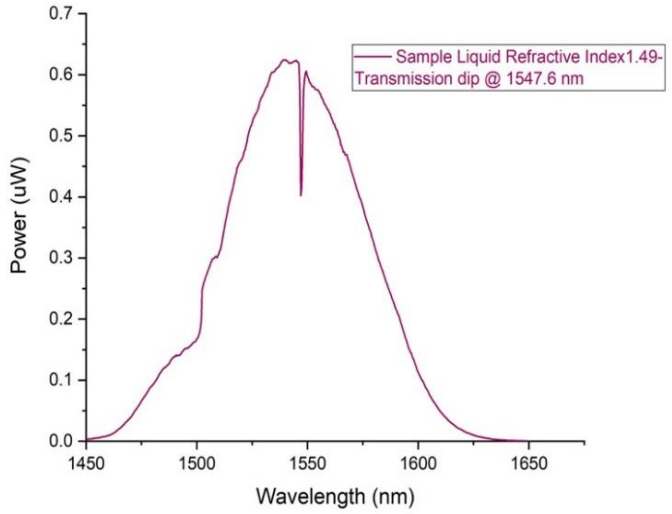
Sample Liquid Refractive Index1.49-
Transmission dip @ 1547.6 nm
Power (uW)
Wavelength (nm)
0.0
0.1
0.2
0.3
0.4
0.5
0.6
0.7
1450
1500
1550
1600
1650

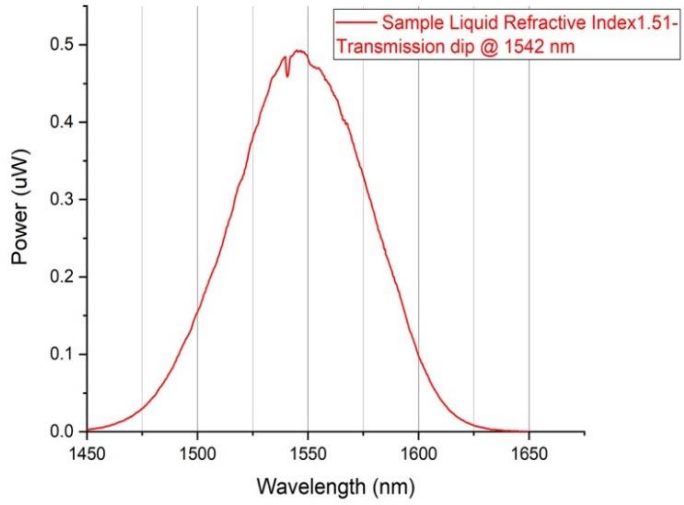
Sample Liquid Refractive Index1.51-
Transmission dip @ 1542 nm
Power (uW)
Wavelength (nm)
0.0
0.1
0.2
0.3
0.4
0.5
1450
1500
1550
1600
1650

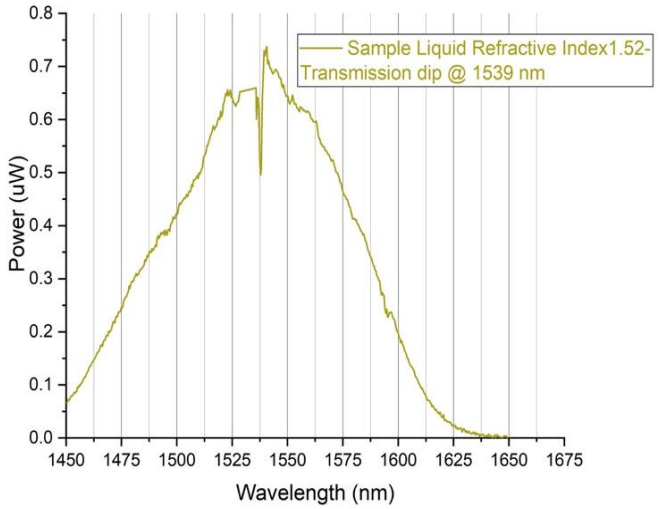
Sample Liquid Refractive Index1.52-
Transmission dip @ 1539 nm
Power (uW)
Wavelength (nm)
0.0
0.1
0.2
0.3
0.4
0.5
0.6
0.7
0.8
1450
1475
1500
1525
1550
1575
1600
1625
1650
1675

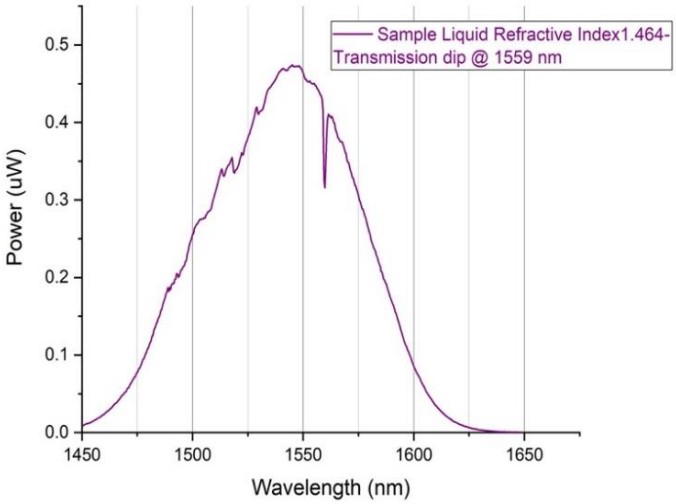
Sample Liquid Refractive Index1.464-
Transmission dip @ 1559 nm
Power (uW)
Wavelength (nm)
0.0
0.1
0.2
0.3
0.4
0.5
1450
1500
1550
1600
1650

APPENDIX D ALL THE SAMPLE LIQUIDS FIGURES FOR SECTION 6.12

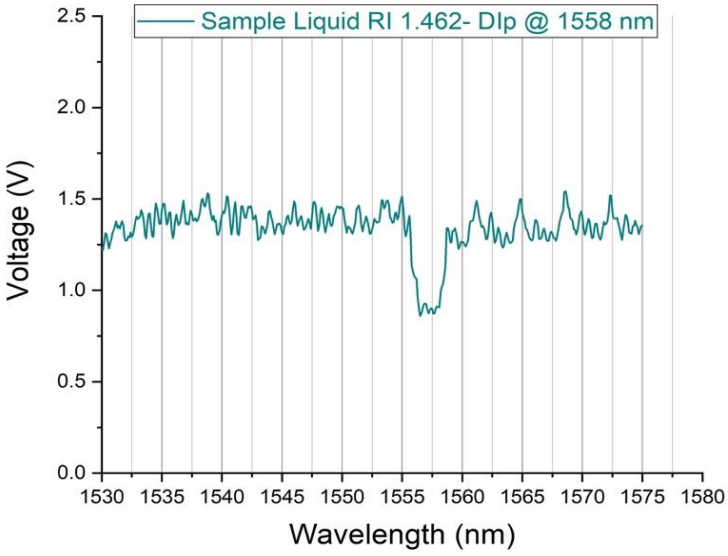
Sample Liquid RI 1.462- Dlp @ 1558 nm
Voltage (V)
Wavelength (nm)
2.5
2.0
1.5
1.0
0.5
0.0
1530 1535 1540 1545 1550 1555 1560 1565 1570 1575 1580

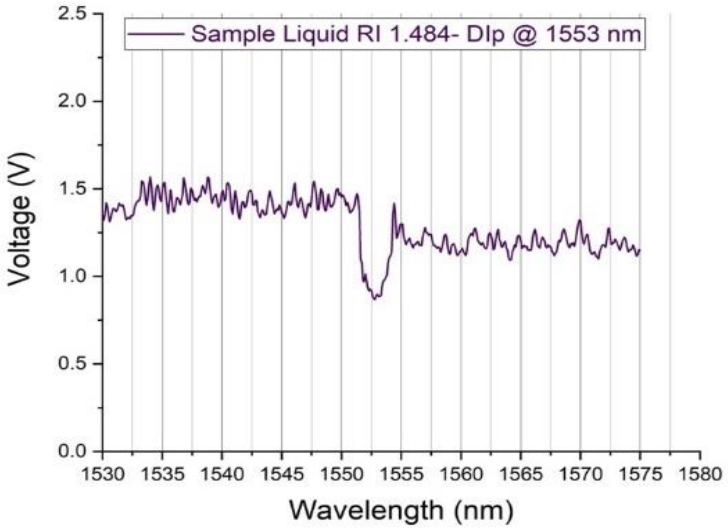
Sample Liquid RI 1.484- Dlp @ 1553 nm
Voltage (V)
Wavelength (nm)
2.5
2.0
1.5
1.0
0.5
0.0
1530 1535 1540 1545 1550 1555 1560 1565 1570 1575 1580

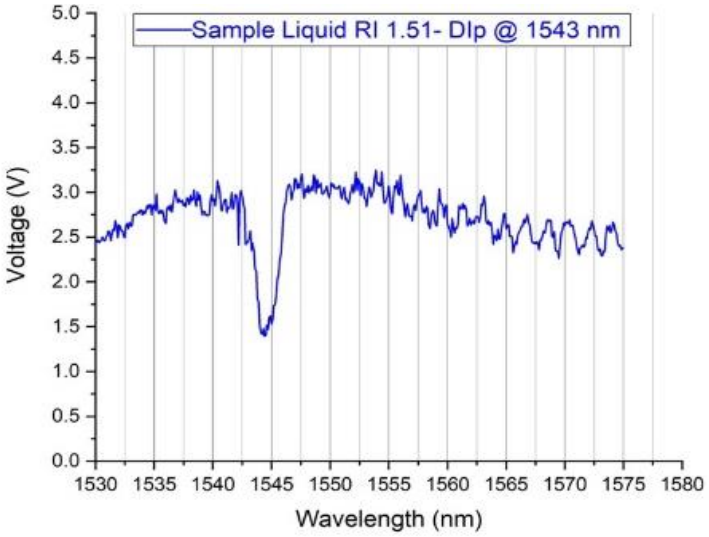
Sample Liquid RI 1.51- DIp @ 1543 nm
Voltage (V)
Wavelength (nm)
5.0
4.5
4.0
3.5
3.0
2.5
2.0
1.5
1.0
0.5
0.0
1530 1535 1540 1545 1550 1555 1560 1565 1570 1575 1580

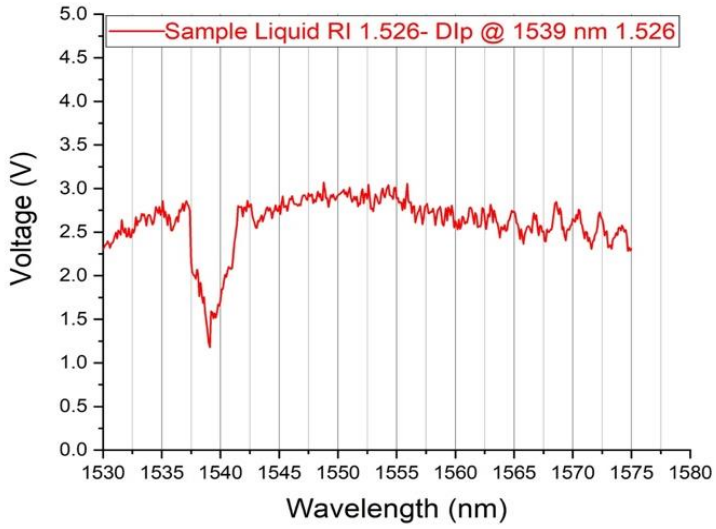
Sample Liquid RI 1.526- DIp @ 1539 nm 1.526
Voltage (V)
Wavelength (nm)
5.0
4.5
4.0
3.5
3.0
2.5
2.0
1.5
1.0
0.5
0.0
1530 1535 1540 1545 1550 1555 1560 1565 1570 1575 1580

APPENDIX E TUNABLE LASER CURRENTS COMPOSITIONS AND WAVELENGTH CHANGING WITH OUTPUT POWER AND VOLTAGE FOR SECTION 7.3

Sample liquid with 1.512 refractive index

Injected current in Section A (SiN_x) (mA)	Injected current in Section B (SiO_xN_y) (mA)	Output Power (mW)	Wavelength (nm)	Voltage after placing the sample liquid (mV)
40	100	1.35	1541.5	120
40	105	1.38	1542	121
40	108	1.42	1542.4	122
40	111	1.44	1542.8	115
42	114	1.45	1543	88
42	117	1.45	1543.4	65
44	120	1.46	1543.6	74
44	122	1.48	1544	89
44	124	1.47	1544.4	100
80	50	1.3	1544.8	105
83	50	1.32	1545.2	113
86	50	1.32	1545.6	125
88	52	1.35	1546	114
92	52	1.35	1546.5	118
94	52	1.37	1546.8	117
98	55	1.39	1547.1	119
100	55	1.42	1547.6	120
103	55	1.42	1548	122
105	55	1.42	1548.3	124
107	55	1.425	1548.8	135
109	55	1.43	1549.2	135
114	53	1.35	1549.6	136
118	53	1.35	1550	132
120	53	1.36	1550.4	130
125	53	1.365	1550.8	135

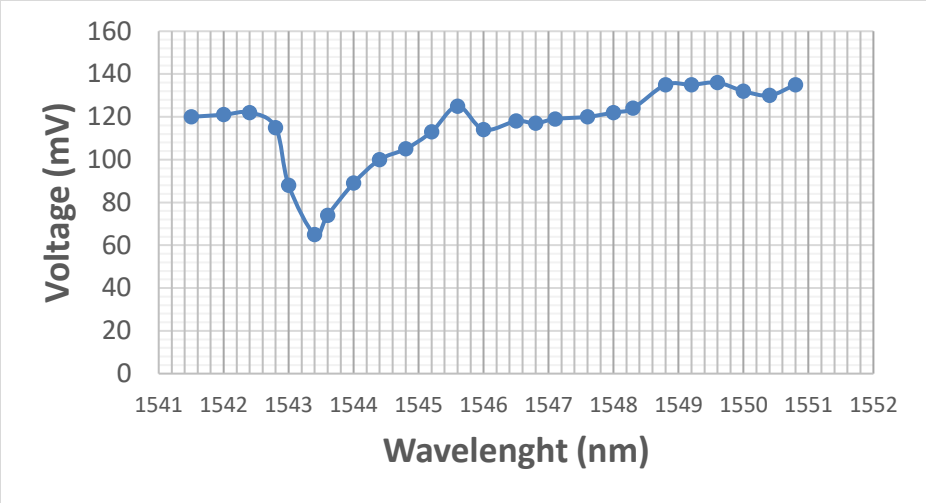

Sample liquid with 1.494 refractive index

Injected current in Section A (SiN_x) (mA)	Injected current in Section B (SiO_xN_y) (mA)	Output Power (mW)	Wavelength (nm)	Voltage after placing the sample liquid (mV)
83	50	1.32	1545.2	110
86	50	1.32	1545.3	107
88	52	1.35	1546	110
92	52	1.35	1546.5	105
94	52	1.37	1546.8	102
98	55	1.39	1547.1	98
100	55	1.42	1547.6	100
103	55	1.42	1548	95
105	55	1.42	1548.3	77
107	55	1.425	1548.8	60
109	55	1.43	1549.2	75
114	53	1.35	1549.6	90
118	53	1.35	1550	90
120	53	1.36	1550.4	97
125	53	1.365	1550.8	97
128	53	1.4	1551.2	100
130	53	1.41	1551.6	100
133	62	1.42	1552	88
135	62	1.45	1552.4	90
137	62	1.48	1552.8	95
139	62	1.49	1553.2	94
140	62	1.49	1553.6	97
165	45	1.44	1554	100
168	45	1.43	1554.4	101
172	45	1.43	1554.8	100
175	45	1.425	1555.2	97
178	45	1.4	1555.6	98

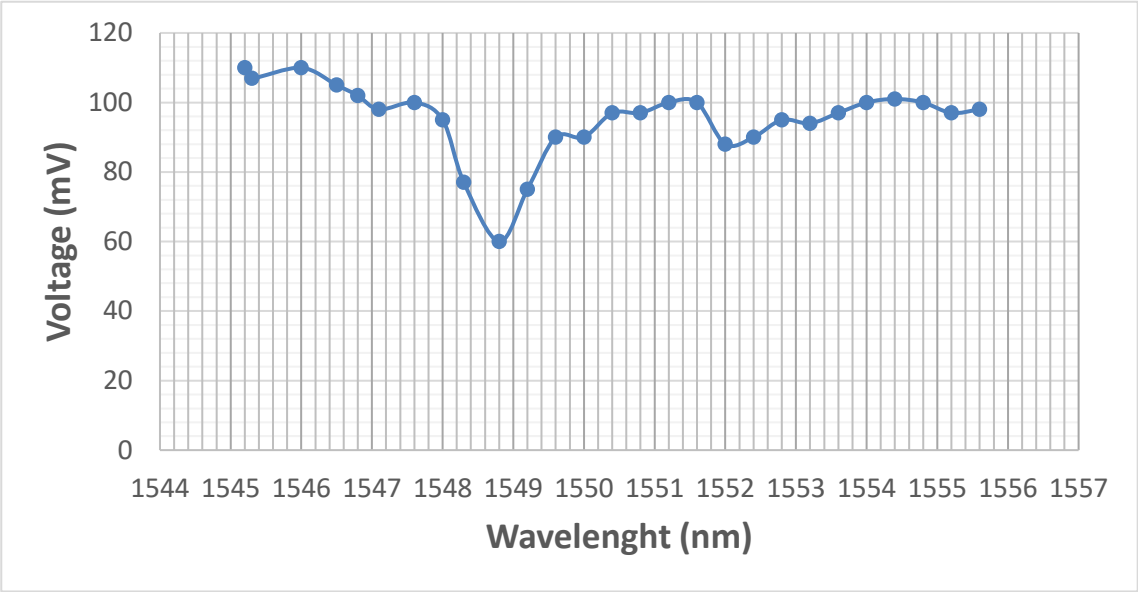

Sample liquid with 1.484 refractive index

Injected current in Section A (SiN_x) (mA)	Injected current in Section B (SiO_xN_y) (mA)	Output Power (mW)	Wavelength (nm)	Voltage after placing the sample liquid (mV)
103	55	1.42	1548	160
105	55	1.42	1548.3	164
107	55	1.425	1548.8	163
109	55	1.43	1549.2	162
114	53	1.35	1549.6	168
118	53	1.35	1550	165
120	53	1.36	1550.4	160
125	53	1.365	1550.8	161
128	53	1.4	1551.2	161
130	53	1.41	1551.6	163
133	62	1.42	1552	169
135	62	1.45	1552.4	170
137	62	1.48	1552.8	168
139	62	1.49	1553.2	150
140	62	1.49	1553.6	142
165	45	1.44	1554	144
168	45	1.43	1554.4	148
172	45	1.43	1554.8	159
175	45	1.425	1555.2	165
178	45	1.4	1555.6	165
100	70	1.48	1555.5	164
103	70	1.49	1555.8	163
106	72	1.5	1556	168
108	74	1.51	1556.3	169
112	78	1.5	1556.6	165

115	80	1.48	1557	165

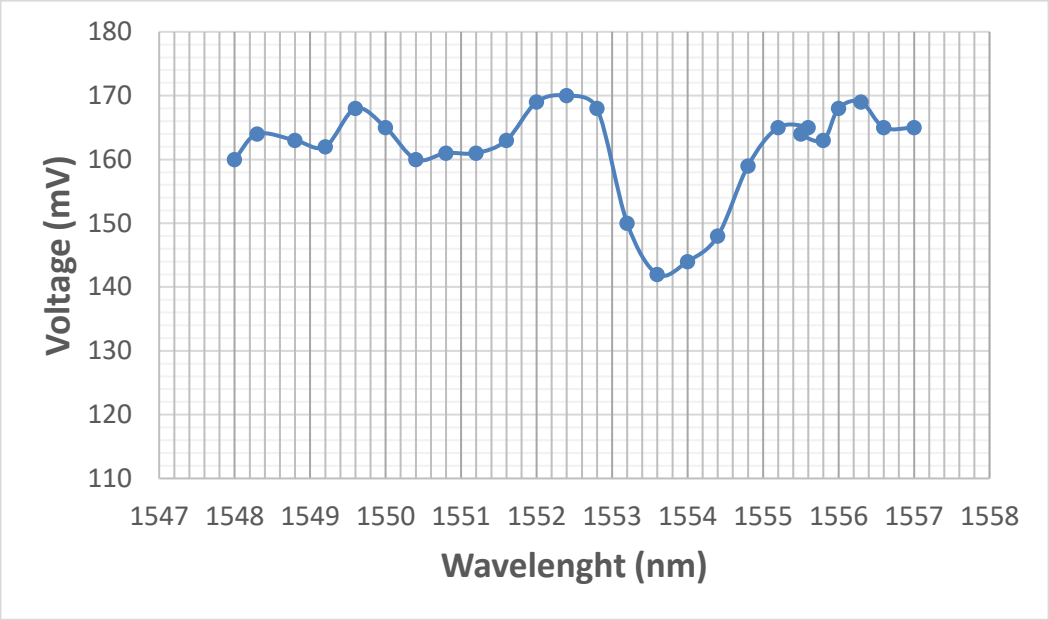

Sample liquid with 1.46 refractive index

Injected current in Section A (SiN_x) (mA)	Injected current in Section B (SiO_xN_y) (mA)	Output Power (mW)	Wavelength (nm)	Voltage after placing the sample liquid (mV)
95	60	1	1554	58.4
97	60	1.02	1554.6	60
99	61	1.04	1555	62
100	63	1.05	1555.5	59
103	63	1.1	1555.8	60
106	63	1.12	1556	59.2
108	64	1.15	1556.3	62.2
112	55	1.12	1556.6	56
115	55	1.24	1557	58
117	56	1.26	1557.3	50
120	56	1.3	1557.7	46
124	56	1.3	1558	28
126	58	1.3	1558.3	24
110	70	1.18	1558.6	38
113	70	1.2	1558.9	40
116	70	1.25	1559.3	60
130	75	1.28	1559.6	58
135	73	1.34	1559.6	62
140	80	1.33	1560	60
143	80	1.36	1560.5	64
146	82	1.36	1561	68

150	82	1.37	1561.6	69
148	87	1.35	1562	68.8

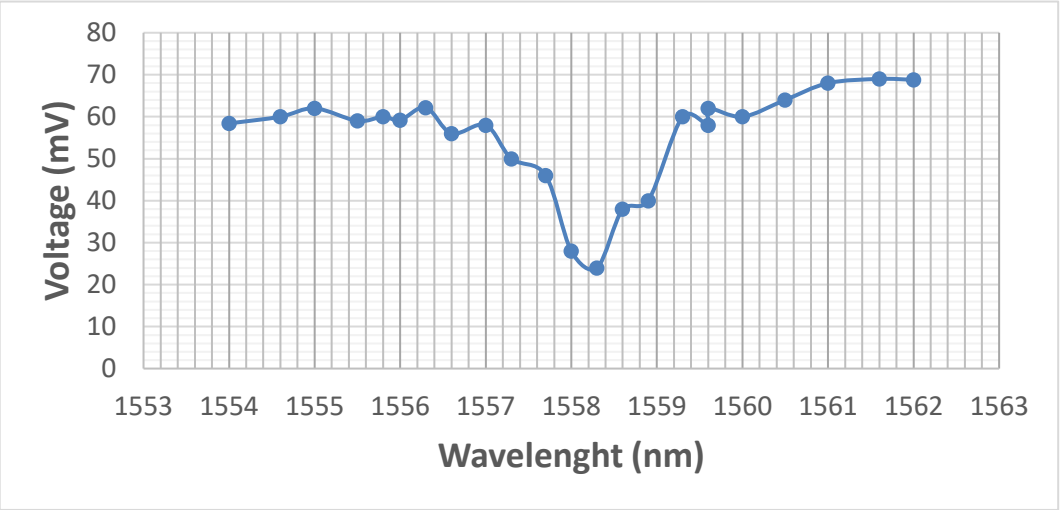

Sample liquid with 1.438 refractive index

Injected current in Section A (SiN_x) (mA)	Injected current in Section B (SiO_xN_y) (mA)	Output Power (mW)	Wavelength (nm)	Voltage after placing the sample liquid (mV)
145	90	1.45	1565	140
148	90	1.48	1565.5	142
150	90	1.49	1566	146
165	99	1.5	1566.5	148
168	100	1.5	1567	150
170	100	1.51	1567.5	135
170	104	1.51	1568	130
172	104	1.52	1568.4	123
175	104	1.53	1568.8	120
176	105	1.52	1569.2	139
177	109	1.51	1569.6	142
180	109	1.51	1570.2	150
184	109	1.51	1570.6	146
188	110	1.48	1571	149

194	110	1.48	1572	155
199	110	1.46	1573	150

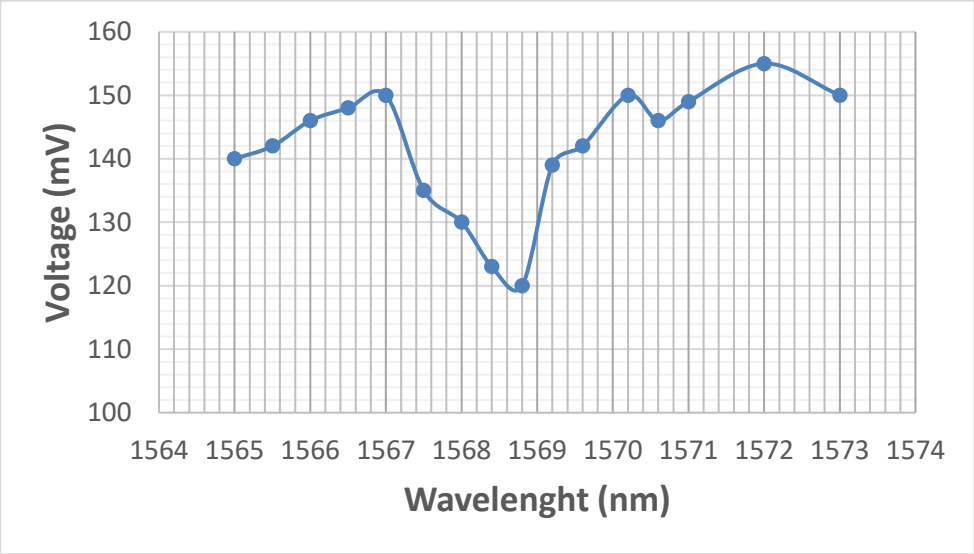

we were able to tune the tunable laser wavelength from 1541 nm to 1572 nm by changing the injected current compositions for both section A and B as shown in figure 7.3-1. For every 1 nm wavelength, there are at least 3 -4 reading as shown in

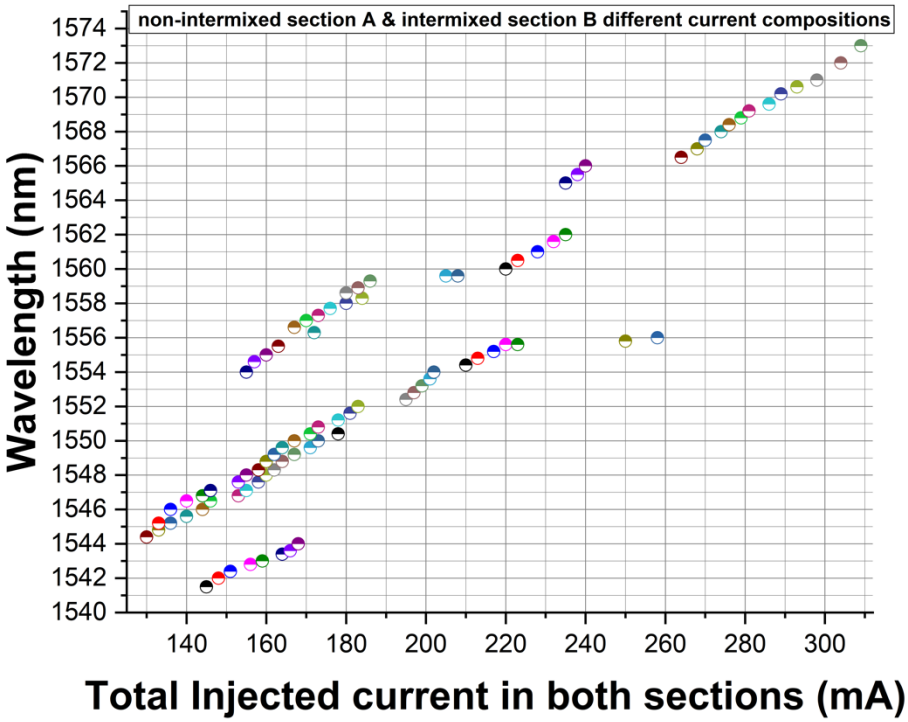

Figure Different current composition for the tunable laser from 1541-1573 nm.

The below figures, show the whole range of tunability from 1541 to 1572 nm that include 78 spectra for that rang.

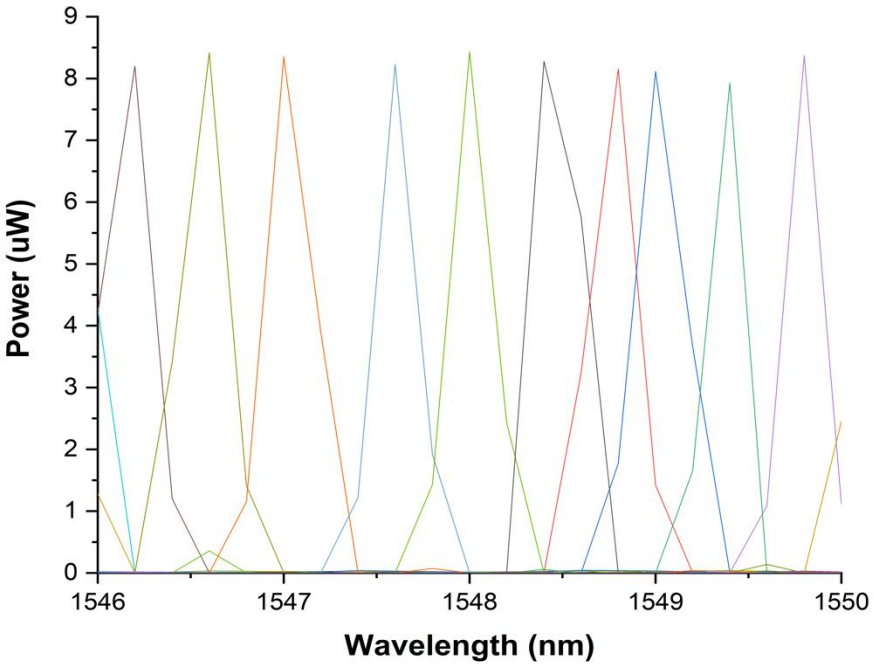

Figure, example of short range laser spectra.

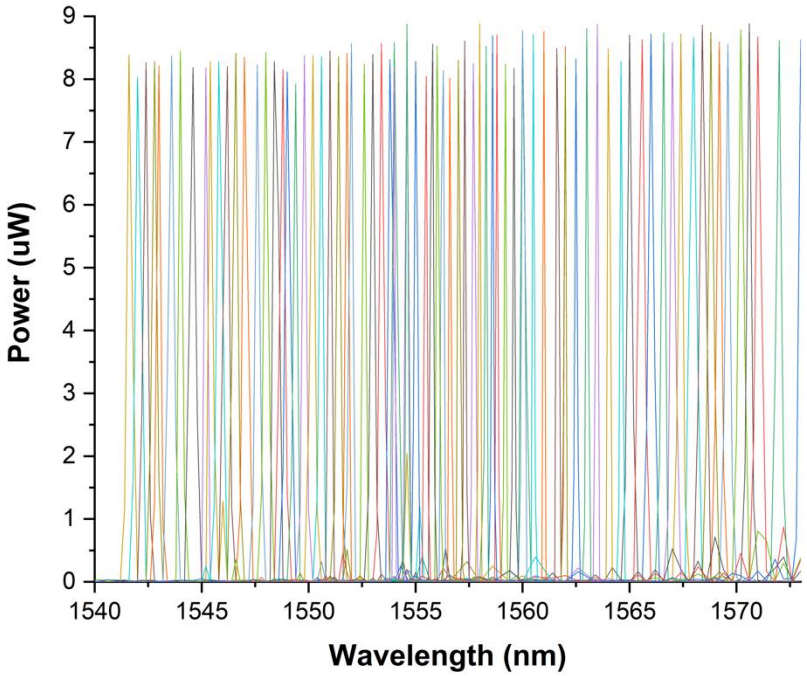

Figure the laser spectra obtained from the two-section laser diode from 1541 to 1573 nm

LIST OF REFERENCES

1. Richards, R.D., et al., *Photovoltaic characterisation of GaAsBi/GaAs multiple quantum well devices.* Solar Energy Materials and Solar Cells, 2017. 172: p. 238-243.
2. Schulz, S., et al., *Atomistic analysis of the impact of alloy and well-width fluctuations on the electronic and optical properties of InGaN/GaN quantum wells.* Physical Review B, 2015. 91(3).
3. Wall, D.L., et al., *Development of IR tunable diode lasers and source assemblies for atmospheric monitoring and related applications*, in *Tunable Diode Laser Spectroscopy, Lidar, and DIAL Techniques for Environmental and Industrial Measurements*. 1994, SPIE.
4. Wu, X., M.T. Trinh, and X.Y. Zhu, *Excitonic Many-Body Interactions in Two-Dimensional Lead Iodide Perovskite Quantum Wells.* The Journal of Physical Chemistry C, 2015. 119(26): p. 14714-14721.
5. Signoret, P., et al., *Bragg section effects on linewidth and lineshape in 1.55-/spl mu/m DBR tunable laser diodes.* IEEE Photonics Technology Letters, 2004. 16(6): p. 1429-1431.
6. Sakano, S., et al., *Tunable DFB laser with a striped thin-film heater.* IEEE Photonics Technology Letters, 1992. 4(4): p. 321-323.
7. Buus, J. and E.J. Murphy, *Tunable lasers in optical networks.* Journal of Lightwave Technology, 2006. 24(1): p. 5-11.
8. Coldren, L.A., et al., *Tunable semiconductor lasers: A tutorial.* Journal of Lightwave Technology, 2004. 22(1): p. 193.
9. Agrawal, G.P., *Lightwave Technology*. 2005, John Wiley & Sons, Inc.

10. Mason, B., et al., *Widely tunable sampled grating DBR laser with integrated electroabsorption modulator.* IEEE Photonics Technology Letters, 1999. 11(6): p. 638-640.
11. Reid, J., D.T. Cassidy, and R.T. Menzies, *Linewidth measurements of tunable diode lasers using heterodyne and etalon techniques.* Applied Optics, 1982. 21(21): p. 3961.
12. Kotaki, Y., et al., *Tunable DBR laser with wide tuning range*. Electronics Letters, 1988. 24(8): p. 503-505.
13. Partin, J.K., *Investigation of Tunable Diode Spectroscopy for Monitoring Gases in Geothermal Plants*. 2006, Office of Scientific and Technical Information (OSTI).
14. Schubert, E.F., *Doping in III–V Semiconductors*. 1993: Cambridge University Press.
15. Hermann, J., R.A. DiStasio, and A. Tkatchenko, *First-Principles Models for van der Waals Interactions in Molecules and Materials: Concepts, Theory, and Applications.* Chemical Reviews, 2017. 117(6): p. 4714-4758.
16. Wan, Q. and G. Galli, *First-Principles Framework to Compute Sum-Frequency Generation Vibrational Spectra of Semiconductors and Insulators.* Physical Review Letters, 2015. 115(24).
17. Peng, X., Q. Wei, and A. Copple, *Strain-engineered direct-indirect band gap transition and its mechanism in two-dimensional phosphorene.* Physical Review B, 2014. 90(8).
18. Lyons, J.L., et al., *First-principles theory of acceptors in nitride semiconductors.* physica status solidi (b), 2015. 252(5): p. 900-908.
19. Hinuma, Y., et al., *Band alignment of semiconductors from density-functional theory and many-body perturbation theory.* Physical Review B, 2014. 90(15).
20. Zhang, S., et al., *Atomically Thin Arsenene and Antimonene: Semimetal-Semiconductor and Indirect-Direct Band-Gap Transitions.* Angewandte Chemie, 2015. 127(10): p. 3155-3158.

21. Zhang, S., et al., *Semiconducting Group 15 Monolayers: A Broad Range of Band Gaps and High Carrier Mobilities.* Angewandte Chemie International Edition, 2015. 55(5): p. 1666-1669.

22. Alkauskas, A., M.D. McCluskey, and C.G. Van de Walle, *Tutorial: Defects in semiconductors—Combining experiment and theory.* Journal of Applied Physics, 2016. 119(18): p. 181101.

23. Liu, Y., et al., *Fundamental theories of piezotronics and piezo-phototronics.* Nano Energy, 2015. 14: p. 257-275.

24. Kuo, Y.-K., J.-Y. Chang, and M.-C. Tsai, *Enhancement in hole-injection efficiency of blue InGaN light-emitting diodes from reduced polarization by some specific designs for the electron blocking layer.* Optics Letters, 2010. 35(19): p. 3285.

25. Kuo, Y.-K., et al., *Advantages of blue InGaN multiple-quantum well light-emitting diodes with InGaN barriers.* Applied Physics Letters, 2009. 95(1): p. 011116.

26. Cho, Y.-H., et al., *"S-shaped" temperature-dependent emission shift and carrier dynamics in InGaN/GaN multiple quantum wells.* Applied Physics Letters, 1998. 73(10): p. 1370-1372.

27. Eastwood, M.A., *Heisenberg's uncertainty principle.* QJM, 2016: p. hcw193.

28. Miller, R.C. and D.A. Kleinman, *EXCITONS IN GaAs QUANTUM WELLS*, in *High Excitation and Short Pulse Phenomena*. 1985, Elsevier. p. 520-540.

29. Lu, T.-P., et al., *The advantage of blue InGaN multiple quantum wells light-emitting diodes with p-AlInN electron blocking layer.* Chinese Physics B, 2011. 20(9): p. 098503.

30. Wang, N., et al., *Perovskite light-emitting diodes based on solution-processed self-organized multiple quantum wells.* Nature Photonics, 2016. 10(11): p. 699-704.

31. Susilo, N., et al., *AlGaN-based deep UV LEDs grown on sputtered and high temperature annealed AlN/sapphire.* Applied Physics Letters, 2018. 112(4): p. 041110.

32. Skogen, E.J., et al., *Multiple-band-edge quantum-well intermixing in the InGaAs/InGaAsP/InGaP material system.* Applied Physics Letters, 2005. 86(24): p. 241117.

33. McKerracher, I., et al., *Intermixing of InGaAs/GaAs quantum wells and quantum dots using sputter-deposited silicon oxynitride capping layers.* Journal of Applied Physics, 2012. 112(11): p. 113511.

34. May-Arrioja, D.A., et al., *Intermixing of InP-based multiple quantum wells for integrated optoelectronic devices.* Microelectronics Journal, 2009. 40(3): p. 574-576.

35. Byun, Y.T., Y.M. Jhon, and S.H. Kim, *Quantum-well Intermixing Process for Large Blueshifting in an Ion-implanted InGaAs/InGaAsP Multiple-quantum-well Structure Using Two-step Annealing.* Journal of the Korean Physical Society, 2010. 57(5): p. 1189-1192.

36. Yu, S.F. and E.H. Li, *Semiconductor lasers using diffused quantum-well structures.* IEEE Journal of Selected Topics in Quantum Electronics, 1998. 4(4): p. 723-735.

37. Zhao, J., et al., *Spatial control based quantum well intermixing in InP/InGaAsP structures using ICP.* Journal of Semiconductors, 2012. 33(10): p. 106001.

38. McLeod, R.R., et al., *3D waveguides with fiber couplers and 90 degree bends in holographic photopolymer*, in *Organic 3D Photonics Materials and Devices*. 2007, SPIE.

39. Sang Kee, S., et al., *Area selectivity of InGaAsP-InP multiquantum-well intermixing by impurity-free vacancy diffusion.* IEEE Journal of Selected Topics in Quantum Electronics, 1998. 4(4): p. 619-623.

40. Helmy, A.S., et al., *Control of silica cap properties by oxygen plasma treatment for single-cap selective impurity free vacancy disordering.* Applied Physics Letters, 1999. 74(5): p. 732-734.

41. Teng, J.H., et al., *Controlled group V intermixing in InGaAsP quantum well structures and its application to the fabrication of two section tunable lasers.* Journal of Applied Physics, 2002. 92(8): p. 4330-4335.

42. Choi, J., et al., *Dependence of dielectric-cap quantum-well disordering of GaAs-AlGaAs quantum-well structure on the hydrogen content in SiN/sub x/ capping layer.* IEEE Journal of Selected Topics in Quantum Electronics, 1998. 4(4): p. 624-628.

43. Pépin, A., *Evidence of stress dependence in SiO2/Si3N4 encapsulation-based layer disordering of GaAs/AlGaAs quantum well heterostructures.* Journal of Vacuum Science & Technology B: Microelectronics and Nanometer Structures, 1997. 15(1): p. 142.

44. Zhang, R., Z. Ren, and S. Yu, *Fabrication of InGaAsP Double Shallow Ridge Rectangular Ring Laser With Total Internal Reflection Mirror by Cascade Etching Technique.* IEEE Photonics Technology Letters, 2007. 19(21): p. 1714-1716.

45. Rao, S.S., W.P. Gillin, and K.P. Homewood, *Interdiffusion of the group-III sublattice in In-Ga-As-P/In-Ga-As-P and In-Ga-As/In-Ga-As heterostructures.* Physical Review B, 1994. 50(11): p. 8071-8073.

46. Rao, E.V.K., et al., *New encapsulant source for III–V quantum well disordering.* Applied Physics Letters, 1995. 66(4): p. 472-474.

47. Fuchida, A., A. Matsutani, and F. Koyama, *Slow-light total-internal-reflection switch with bending angle of 30 deg.* Optics Letters, 2011. 36(14): p. 2644.

48. Rohner, D. and H. Kobeissi, *Secondary measurement of rapid thermal annealer temperature*. 1998, Google Patents.

49. Aleahmad, P., et al. *Controllable red and blue bandgap energy shifted LEDs and modulators on InGaAsP quantum well platform*. in *SPIE OPTO*. 2016. International Society for Optics and Photonics.

50. Marsh, J.H., *Quantum well intermixing.* Semiconductor science and technology, 1993. 8(6): p. 1136.

51. Ooi, B.-S., et al., *Fabrication of multiple wavelength lasers in GaAs-AlGaAs structures using a one-step spatially controlled quantum-well intermixing technique.* IEEE Photonics Technology Letters, 1995. 7(9): p. 944-946.

52. Li, E.H. *Quantum well intermixing: materials modeling and device physics*. in *Optoelectronics and High-Power Lasers & Applications*. 1998. International Society for Optics and Photonics.

53. Pepin, A., et al., *Evidence of stress dependence in SiO2/Si3N4 encapsulation-based layer disordering of GaAs/AlGaAs quantum well heterostructures.* Journal of Vacuum Science & Technology B, 1997. 15(1): p. 142-153.

54. Greiner, M.E. and J.F. Gibbons, *Diffusion of silicon in gallium arsenide using rapid thermal processing: Experiment and model.* Applied Physics Letters, 1984. 44(8): p. 750-752.

55. Moon, E.-A., J.-L. Lee, and H.M. Yoo, *Selective wet etching of GaAs on AlxGa1-xAs for AlGaAs/InGaAs/AlGaAs pseudomorphic high electron mobility transistor.* 1998.

56. Kim, J.-H., D.H. Lim, and G.M. Yang, *Selective etching of AlGaAs/GaAs structures using the solutions of citric acid H2O2 and de-ionized H2O buffered oxide etch.* Journal of Vacuum Science & Technology B, 1998. 16(2): p. 558-560.

57. Dill, F.H., et al., *Characterization of positive photoresist.* IEEE Transactions on electron devices, 1975. 22(7): p. 445-452.

58. Ueno, K., V.M. Donnelly, and Y. Tsuchiya, *Cleaning of CHF3 plasma-etched SiO2/SiN/Cu via structures using a hydrogen plasma, an oxygen plasma, and hexafluoroacetylacetone vapors.* Journal of Vacuum Science & Technology B, 1998. 16(6): p. 2986-2995.

59. Jourdain, A., et al., *Mechanical and electrical characterization of BCB as a bond and seal material for cavities housing (RF-) MEMS devices.* Journal of micromechanics and microengineering, 2005. 15(7): p. S89.

60. Woehrmann, M. and M. Toepper, *Polymerization of Thin Film Polymers*. 2012: INTECH Open Access Publisher.

61. Camlibel, I., et al., *Metallurgical Behavior of Gold-Based Ohmic Contacts to the InP/InGaAsP Material System.* Journal of The Electrochemical Society, 1982. 129(11): p. 2585-2590.

62. Cho, E.C., et al., *Understanding the role of surface charges in cellular adsorption versus internalization by selectively removing gold nanoparticles on the cell surface with a I2/KI etchant.* Nano letters, 2009. 9(3): p. 1080-1084.

63. Lin, C. and C. Lee, *Comparison of Au/Ni/Ge, Au/Pd/Ge, and Au/Pt/Ge Ohmic contacts to n-type GaAs.* Journal of Applied Physics, 1990. 67(1): p. 260-263.

64. Bechelany, M., et al., *Synthesis mechanisms of organized gold nanoparticles: influence of annealing temperature and atmosphere.* Crystal Growth & Design, 2010. 10(2): p. 587-596.

65. Aleahmad, P., et al. *Controllable red and blue bandgap energy shifted LEDs and modulators on InGaAsP quantum well platform*. in *Proc. of SPIE Vol*. 2016.

66. Liu, K. and M.G. Littman, *Novel geometry for single-mode scanning of tunable lasers.* Optics letters, 1981. 6(3): p. 117-118.

67. Buus, J., M.-C. Amann, and D.J. Blumenthal, *Tunable laser diodes and related optical sources*. 2005: John Wiley & Sons.

68. Matsushita, S., et al., *Diffusion and doping of Si into GaAS from undoped SiO x/SiN film.* Applied physics letters, 1993. 63(2): p. 225-227.

69. Tabbakh, T. and P. LiKamWa, *Dual Wavelength Single Waveguide Laser Diode Fabricated using Selective Area Quantum Well Intermixing.* Optik-International Journal for Light and Electron Optics, 2017.

70. Zakariya, A.J. and P. LiKamWa. *Monolithic tunable laser based on selectively intermixed GaAs/AlGaAs QW structure*. in *Photonics Conference (IPC), 2012 IEEE*. 2012. IEEE.

71. Stano, A., *Chemical etching characteristics of InGaAs/InP and InAlAs/InP heterostructures.* Journal of the Electrochemical Society, 1987. 134(2): p. 448-452.

72. Garrou, P.E., et al., *Rapid thermal curing of BCB dielectric.* IEEE transactions on components, hybrids, and manufacturing technology, 1993. 16(1): p. 46-52.

73. Tabbakh, T. and P. LiKamWa. *Tunable laser diode using partially intermixed InGaAsP multiple quantum well*. in *Laser Applications in Microelectronic and Optoelectronic Manufacturing (LAMOM) XXIII*. 2018. International Society for Optics and Photonics.

74. Alvarez, M., et al., *Development of nanomechanical biosensors for detection of the pesticide DDT.* Biosensors and Bioelectronics, 2003. 18(5-6): p. 649-653.

75. Carrascosa, L.G., et al., *Nanomechanical biosensors: a new sensing tool.* TrAC Trends in Analytical Chemistry, 2006. 25(3): p. 196-206.

76. Tamayo, J., et al., *Biosensors based on nanomechanical systems.* Chemical Society Reviews, 2013. 42(3): p. 1287-1311.

77. Kribich, K.R., et al., *Novel chemical sensor/biosensor platform based on optical multimode interference (MMI) couplers.* Sensors and Actuators B: Chemical, 2005. 107(1): p. 188-192.

78. Luff, B.J., et al., *Integrated-optical directional coupler biosensor.* Optics Letters, 1996. 21(8): p. 618.

79. Misiakos, K., et al., *A Monolithic Silicon Optoelectronic Transducer as a Real-Time Affinity Biosensor.* Analytical Chemistry, 2004. 76(5): p. 1366-1373.

80. Pfeifer, P., et al., *Real time sensing of specific molecular binding using surface plasmon resonance spectroscopy.* Sensors and Actuators B: Chemical, 1999. 54(1-2): p. 166-175.

81. Prieto, F., et al., *Design and analysis of silicon antiresonant reflecting optical waveguides for evanescent field sensor.* Journal of Lightwave Technology, 2000. 18(7): p. 966-972.

82. Quan, H. and Z. Guo, *Simulation of whispering-gallery-mode resonance shifts for optical miniature biosensors.* Journal of Quantitative Spectroscopy and Radiative Transfer, 2005. 93(1-3): p. 231-243.

83. Suzuki, A., et al., *Development of novel optical waveguide surface plasmon resonance (SPR) sensor with dual light emitting diodes.* Sensors and Actuators B: Chemical, 2005. 106(1): p. 383-387.

84. Burkhardt, H., *Dispersion relation dynamics.* 1969.

85. Tobiška, P., et al., *An integrated optic hydrogen sensor based on SPR on palladium.* Sensors and Actuators B: Chemical, 2001. 74(1-3): p. 168-172.

86. Wang, T.-J., W.-S. Lin, and F.-K. Liu, *Integrated-optic biosensor by electro-optically modulated surface plasmon resonance.* Biosensors and Bioelectronics, 2007. 22(7): p. 1441-1446.

87. Wheeler, A., *Poly(dimethylsiloxane) microfluidic flow cells for surface plasmon resonance spectroscopy.* Sensors and Actuators B: Chemical, 2004. 98(2-3): p. 208-214.

88. Homola, J., et al., *A novel multichannel surface plasmon resonance biosensor.* Sensors and Actuators B: Chemical, 2001. 76(1-3): p. 403-410.

89. Huang, J.-G., et al., *A miniaturized germanium-doped silicon dioxide-based surface plasmon resonance waveguide sensor for immunoassay detection.* Biosensors and Bioelectronics, 2006. 22(4): p. 519-525.

90. Dostálek, J., et al., *Surface plasmon resonance biosensor based on integrated optical waveguide.* Sensors and Actuators B: Chemical, 2001. 76(1-3): p. 8-12.

91. Dostálek, J., H. Vaisocherová, and J. Homola, *Multichannel surface plasmon resonance biosensor with wavelength division multiplexing.* Sensors and Actuators B: Chemical, 2005. 108(1-2): p. 758-764.

92. Harris, R.D., et al., *Integrated optical surface plasmon resonance immunoprobe for simazine detection.* Biosensors and Bioelectronics, 1999. 14(4): p. 377-386.

93. Homola, J., *Present and future of surface plasmon resonance biosensors*. Analytical and Bioanalytical Chemistry, 2003. 377(3): p. 528-539.

94. Carrascosa, L.G., et al., *Nanomechanical biosensors: a new sensing tool.* TrAC Trends in Analytical Chemistry, 2006. 25(3): p. 196-206.

95. Cohen, D.A., et al., *Monolithic chemical sensor using heterodyned sampled grating DBR lasers.* Electronics Letters, 2001. 37(22): p. 1358.

96. Čtyroký, J., et al., *Theory and modelling of optical waveguide sensors utilising surface plasmon resonance.* Sensors and Actuators B: Chemical, 1999. 54(1-2): p. 66-73.

97. Okamoto, K., *Fundamentals of optical waveguides*. 2010: Academic press.

98. Homola, J., S.S. Yee, and G. Gauglitz, *Surface plasmon resonance sensors.* Sensors and Actuators B: Chemical, 1999. 54(1-2): p. 3-15.

99. Aleahmad, P., et al. *Controllable red and blue bandgap energy shifted LEDs and modulators on InGaAsP quantum well platform*. in *Integrated Optics: Devices, Materials, and Technologies XX*. 2016. International Society for Optics and Photonics.

100. Tabbakh, T. and P. LiKam. *Blue and red shifted, partially intermixed InGaAsP quantum well semiconductor laser diodes*. in *Photonics Conference (IPC), 2017 IEEE*. 2017. IEEE